uOttawa

L'Université canadienne
Canada's university

FACULTÉ DES ÉTUDES SUPÉRIEURES ET POSTOCTORALES

uOttawa

L'Université canadienne
Canada's university

FACULTY OF GRADUATE AND POSDOCTORAL STUDIES

Brian Maxwell

AUTEUR DE LA THÈSE / AUTHOR OF THESIS

M.A.Sc. (Mechanical Engineering)

GRADE / DEGREE

School of Information Technology and Engineering

FACULTÉ, ÉCOLE, DÉPARTEMENT / FACULTY, SCHOOL, DEPARTMENT

One-Dimensional Model for Predicting Ignition During an Accidental Release of Pressurized Hydrogen into Air

TITRE DE LA THÈSE / TITLE OF THESIS

M. Radulescu

DIRECTEUR (DIRECTRICE) DE LA THÈSE / THESIS SUPERVISOR

CO-DIRECTEUR (CO-DIRECTRICE) DE LA THÈSE / THESIS CO-SUPERVISOR

M. Johnson

B. Jodoin

Gary W. Slater

Le Doyen de la Faculté des études supérieures et postdoctorales / Dean of the Faculty of Graduate and Postdoctoral Studies

One-Dimensional Model for Predicting Ignition During an Accidental Release of Pressurized Hydrogen into Air

Brian McN. Maxwell

A thesis submitted to the Faculty of Graduate and Postdoctoral Studies
in partial fulfillment of the requirements for the degree of

MASTER OF APPLIED SCIENCE

In Mechanical Engineering

Ottawa-Carleton Institute for Mechanical and Aerospace Engineering
University of Ottawa
Ottawa, Canada

January, 2010

Your file Votre référence
ISBN: 978-0-494-66237-3
Our file Notre référence
ISBN: 978-0-494-66237-3

Abstract

Previous experiments demonstrated that the accidental release of high pressure hydrogen into air can lead to the possibility of spontaneous ignition. It is believed that this ignition is due to the heating of the mixing layer, between hydrogen and air, caused by a shock wave that is driven by the pressurized hydrogen during the release. Currently, this problem is poorly understood and not amenable to direct numerical simulation. This is due to the presence of a wide range of scales between the sizes of the blast wave and the very thin mixing layer. The present study addresses this fundamental ignition problem and develops a solution framework in order to predict the ignition event, for given hydrogen storage pressures and dimension of the release hole, using a two stage model. The key physical processes in the problem are identified to be the mixing of the two gases at the mixing layer, the initial heating by the shock wave, and a cooling effect due to expansion of the mixing layer. First, a multi-dimensional non-reactive compressible flow solver is used to determine the expansion rate of the gas. Next, the mixing layer between the hydrogen and air is considered in a high resolution, one-dimensional model. The mixing layer, at the jet head, is advected as a Lagrangian fluid particle. Results indicate that for every storage pressure, there exists a critical hole size below which ignition is prevented during the release process. This limit was found to depend on the competition between the heating provided by the shock wave and the cooling due to expansion. Furthermore, the limiting ignition criteria were found to be well approximated, to leading order, by the Homogeneous Ignition Model of Cuenot and Poinsot, supplemented by a heat loss term due to expansion. Therefore, turbulent mixing occurring in reality is not likely to affect the ignition limits derived in the present study.

Acknowledgements

I would like to give special thanks to Matei Radulescu for his guidance and help during the development of this thesis. He has been an excellent teacher and supervisor. Furthermore, his knowledge in the fields of combustion and gas dynamics has been integral for the completion of this project. I would also like to give thanks to the NSERC Hydrogen Canada (H2CAN) Strategic Research Network for providing funding to make this research possible. I would also like to thank my wife Megan for her love, patience, and understanding during the busy times. Finally, I would like to thank my friends and family, especially my parents, for their continuing support.

Contents

List of Tables

List of Figures

Nomenclature

Variable	*Description*	*S.I. Units*
a	Speed of sound	m/s
c_p	Specific heat capacity at constant pressure for the mixture	J/kg·K
$c_{p,i}$	Specific heat capacity at constant pressure for the *i*th species	J/kg·K
D_{im}	Mixture-averaged diffusion coefficient of the *i*th species	m^2/s
$D_{T,i}$	Thermal diffusion coefficient of the *i*th species	m^2/s
$D_{i,j}$	Binary diffusion coefficient for species *i* and *j*	m^2/s
e	Total specific energy of the mixture	J/kg
h	Specific enthalpy of the mixture	J/kg
h_i	Specific enthalpy of the ith species	J/kg
h_i^o	Specific enthalpy of formation at 300K for the ith species	J/kg
k	Thermal conductivity for the mixture	W/m·K
m	Mass coordinate (Lagrangian coordinate)	kg/m^2
p	Pressure	Pa
q_{rad}	Heat flux due to radiation	W/m^2
R^o	Universal gas constant	J/K·mol
R	Size of blast wave	m
r	Hole radius	m
s	Specific entropy	J/kg·K
T	Temperature	K
t	Time (Eulerian coordinates)	s
u	Average velocity of the mixture	m/s
u_i	Velocity of the ith species	m/s
$u_{d,i}$	Diffusion velocity of the ith species	m/s
$u_{od,i}$	Ordinary diffusion velocity of the ith species	m/s
u_c	Correction for mixture-averaged diffusion velocity	m/s

$\overline{W}$	Mean molecular weight of the mixture	g/mol
$w_{d,i}$	Thermal diffusion velocity of the ith species	m/s
X_i	Mole fraction of the ith species	--
x	Spatial coordinate (Eulerian coordinate)	m
Y_i	Mass fraction of the ith species	--
z	Time (Lagrangian coordinate)	s
f_i	External forces acting on the ith species	N
α	Diffusivity	m^2/s
γ	Ratio of specific heats	--
δ	Size of mixing layer	m
ρ	Density	kg/m^3
ρ_i	Density of the ith species	kg/m^3
$\bar{\bar{\tau}}$	Shear stress tensor	Pa
ω_i	net rate of production of the ith species	$kg/m^3 \cdot s$
R_e	Reynolds number	--

Chapter 1

Introduction

1.1 Spontaneous Ignition of Pressurized H_2 Releases

Hydrogen gas is currently a clean energy carrier compared to using gasoline or other fuels in automobiles. It can be used in internal combustion engines or in fuel cells to generate power. However, a primary concern with using hydrogen is the safety of storing and handling the fuel. In order for hydrogen to be used as a fuel, it must be compressed to high pressures. This ensures that the fuel has a large amount of energy available in a small volume. Typical storage pressures for hydrogen gas to be used for transportation purposes are between 350 and 700 atmospheres (Vieira, et al. 2007). Unfortunately, many published experiments indicate that the accidental release of high pressure hydrogen into air can lead to spontaneous ignition, without a spark or flame present (Dryer, et al. 2007; Golub, et al. 2008; Mogi, et al. 2008; Wolanski and Wojcicki 1973).

In Canada, there are standards that have recently been published for the installation of hydrogen storage containers, hydrogen piping systems, hydrogen utilizing equipment, and hydrogen generating equipment (Bureau de normalisation du Québec 2007). However, these standards are relatively new and very little is known about the mechanisms that contribute to

the spontaneous ignition phenomena that is observed during accidental releases. In a recent study (Astbury and Hawksworth 2007), about 86% out of 81 investigated incidents involving hydrogen do not have an identified source of ignition. In their study, Astbury and Hawksworth postulated several mechanisms which may contribute to this spontaneous ignition. It is believed, in the study, that these unknown ignition incidents are due to five specific mechanisms. They are; 1) Reverse Joule-Thompson effect, 2) Electrostatic ignition, 3) Diffusion ignition, 4) Sudden adiabatic compression, and 5) Hot surface ignition. The first mechanism, the Reverse Joule-Thompson effect, was shown not to contribute sufficient amount of heat for ignition of the expanding gas to occur. Therefore, in the absence of a hot surface or sudden adiabatic compression of the gas, diffusion ignition and electrostatic ignition are the most likely mechanisms responsible for spontaneous ignition. In particular, diffusion ignition was first postulated to be a source of spontaneous ignition by Wolanski and Wojcicki (1973). In their study, Wolanski and Wojcicki demonstrated that ignition is possible when a diffusive mixing layer between hydrogen and air is subject to a shock wave. Furthermore, the codes and standards, mentioned above, do not have any design guidelines regarding diffusion ignition as a possible source of ignition. Therefore, in the present thesis, the shock induced diffusion ignition mechanism contributing to spontaneous ignition is of particular interest and is studied for the special case of hydrogen expansion directly into the atmosphere.

1.2 The Diffusion Ignition Mechanism

Consider a high pressure hydrogen storage tank with a sudden puncture. The subsequent release of hydrogen is essentially the gas dynamic problem of a highly under-expanded jet, as explained by Radulescu and Law (2007). The hydrogen jet, shown in Figure 1.1, acts as a piston which drives a strong shock wave into the air, in front of the jet head itself. The high temperature induced by the shock wave can trigger ignition in regions behind the shock where the gases have mixed. The turbulent mixing layer, shown in Figure 1.1, is a very thin region at the head of the jet which separates the shocked air from the cool expanding hydrogen.

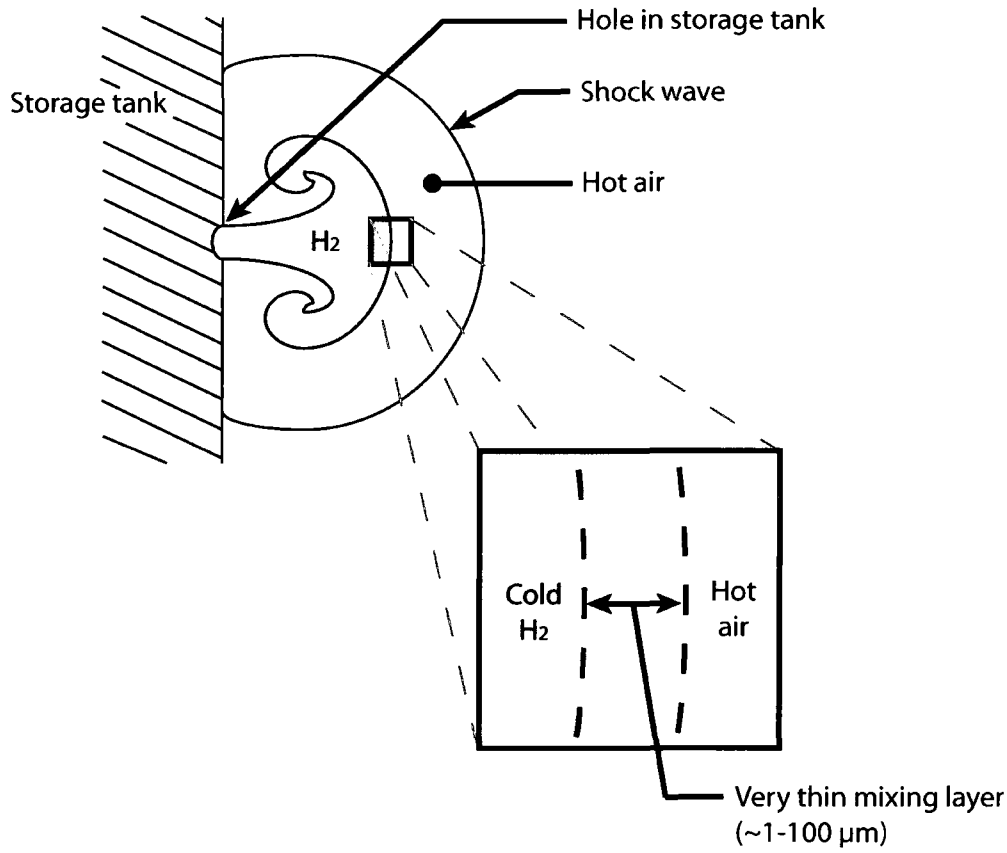

Figure 1.1 Accidental release of hydrogen from a high pressure storage tank (pictorial). Also shown in the Figure is the thin mixing layer at the head of the jet where the hydrogen mixes with shocked air ultimately leading to diffusion ignition.

In Wolanski and Wojcicki's paper (1973), the hydrogen release experiment was carried out in a *shock tube* (Liepmann and Rhoshko 2001), as illustrated in Figure 1.2. This particular shock tube setup has 3 sections; i) a driver section filled with a mixture of hydrogen, oxygen, and helium, ii) a driven section filled with pure hydrogen, and iii) a cylindrical section filled with pure oxygen. Each section is separated initially by membranes that are designed to burst when there is a sufficient pressure difference between the sections. Their findings show that the action of the pressurized hydrogen bursting into the cylindrical oxygen section causes a spherical shock wave, much like the one illustrated above in Figure 1.1, to propagate into the oxygen, thus raising the temperature of the oxygen. Furthermore, combustion is observed in the mixing layer, located at the head of the hydrogen jet. The cause of ignition in this region is found to be the diffusion of heat into the mixing layer from the shocked oxygen, hence the term diffusion ignition. In addition to the experiments conducted by Wolanski and Wojcicki, the diffusion ignition phenomenon has also been observed experimentally by other various groups. In a recent study by Dryer, et al. (2007), diffusion ignition was observed for hydrogen releases into atmosphere. The experimental setup, much like the one shown below in Figure 1.3, consisted of a high pressure storage tank, a reservoir with a burst disk at the end, and some downstream geometry (tubes of various lengths for example). In their experiment, they were able to show that ignition occurred during a release providing that the pressure, at which the burst disk ruptured, was sufficiently high and that there was sufficient mixing downstream from the burst disk. Although the geometry downstream is important for influencing the mixing process, upstream geometry did not affect ignition. Release experiments were also conducted recently by Golub, et al. (2008) and Mogi, et al. (2008) using a setup similar to Dryer's experiment. In their experiments they were able to show that there exists a storage pressure

dependence on length of tube, downstream from the burst disk, in order for ignition to occur. Shorter tubes require higher storage pressures in order for ignition to occur. Experiments were also conducted by Golub, et al. (2008) for unconfined releases in the absence of downstream geometry, although ignition was not observed. It should be noted, however, that the releases directly into atmosphere were conducted at storage pressures up to 123 atmospheres, but that the typical storage pressures for hydrogen are well above this limit; 350 to 700 atmospheres (Vieira, et al. 2007). In all three experiments (Dryer, et al. 2007; Golub, et al. 2008; Mogi, et al. 2008), it has been confirmed that shock induced diffusion-ignition in the mixing layer is indeed a significant mechanism contributing to spontaneous ignition. However, what is not clear in the experiments is that, in addition to this shock induced heating during release, the gas is also expanded and cooled. This is especially evident in the absence of a tube. Therefore, there are actually two competing mechanisms that control ignition; one of heat addition due to chemical reactions in the shocked gas, and one of cooling due to expansion. The present study addresses this fundamental diffusion-ignition problem with expansion and develops a solution framework in order to predict the ignition event for given hydrogen storage pressures and dimension of the release hole.

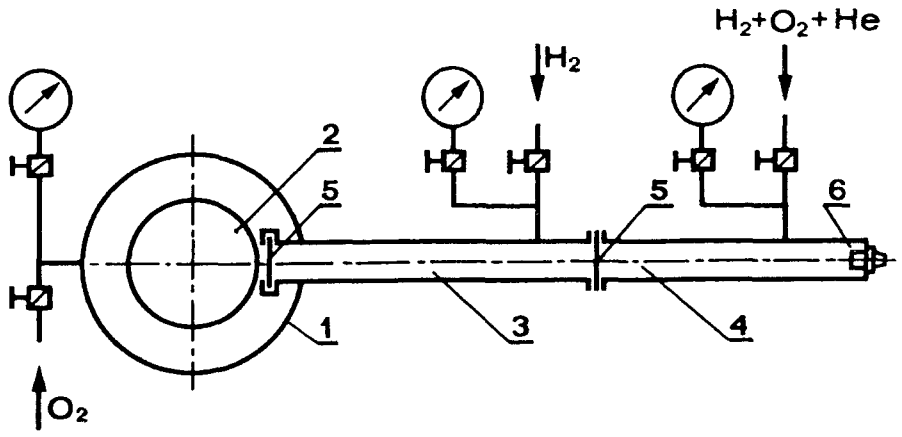

Figure 1.2 Shock tube setup for experiments conducted by Wolanski and Wojcicki (1973). Apparatus consists of 1) cylindrical chamber, 2) windows, 3) driven section, 4) driving section, 5) membrane, and 6) ignition plug.

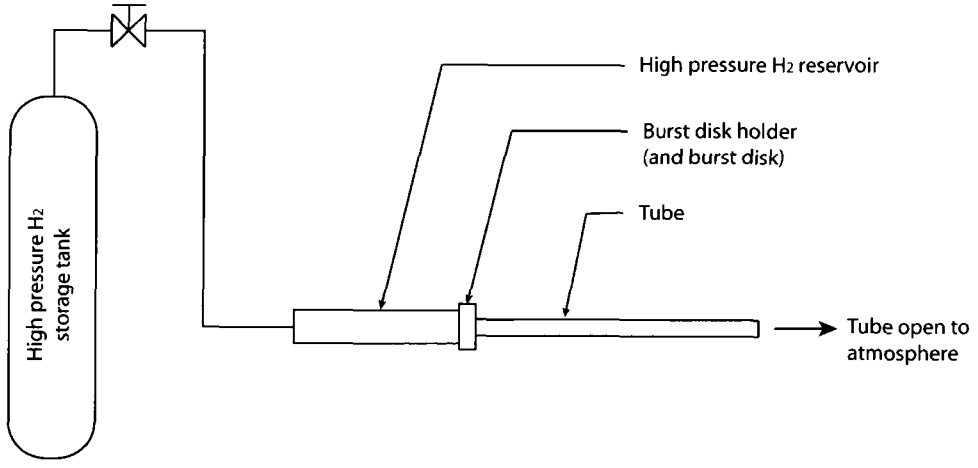

Figure 1.3 Typical experimental set-up (simplified). Here a high pressure storage tank is connected to a high pressure reservoir through a series of valves, gauges, and pipe fittings (not shown). At the end of the reservoir is a burst disk, designed to burst at certain pressures. In most cases, a tube is attached to end of the apparatus and is open to the atmosphere.

1.3 Current Solution Methodology

At present, this problem is poorly understood and not amenable to direct numerical simulation. Current CFD codes (Liu, et al. 2005; Liu, et al. 2009; Xu, et al. 2008; Xu, et al. 2009) for the hydrogen release problem, which take expansion into account, lack the resolution necessary to capture the ignition phenomena that occurs at small scales within the mixing layer. This is a problem since the size of the mixing layer, compared to the size of the blast wave itself, is very small. For example, while a blast wave can span several meters, the size of the mixing layer is only on the order of 1-100μm. Although Xu, et al. (2008; 2009) has attempted to solve the multi-dimensional release problem through *direct numerical simulation* (DNS) (Anderson 1995; Versteeg and Malalasekera 2007) of the *Navier-Stokes equations* using a detailed multi-component kinetic mechanism, they were only able to achieve a minimum grid resolution of 20μm. In a similar multi-dimensional numerical experiment, Liu, et al. (2005) solves the *Euler equations*, also using detailed mutli-component chemistry, and is able to achieve a minimum resolution is 10μm. In both of these cases, however, the minimum resolution does not capture the molecular diffusion that occurs within the mixing layer itself. Therefore, the validity of the models is questionable as the ignition phenomena, captured in the simulations, is subject to *false diffusion* (Versteeg and Malalasekera 2007) and *artificial dissipation* (Anderson 1995). Nevertheless the numerical experiments conducted by Liu, et al. (2005) and Xu, et al. (2008; 2009) show that larger storage pressures drive stronger shocks, thus contributing to the diffusion-ignition problem, even in the absence of an extension tube. The experiments also show that expansion of the gas has a cooling effect, and in some cases, the ignition process is quenched. Furthermore, numerical experiments conducted by Liu, et al. (2009) show that

smaller holes, through which hydrogen is released, make it more difficult for ignition to occur. What is not known yet, however, is how these factors (storage pressure, expansion of the gas, and hole size) contribute to ignition and what the limits are in order for self-ignition to occur during a release.

1.4 Proposed Methodology for this Study

In this study, the hydrogen release problem is modelled in two stages in order to accurately resolve the problem at the mixing layer. First, the multi-dimensional hydrogen release is modelled using a non-reactive compressible flow solver, explained in Section 2.1, in order to determine the expansion rate at the head of the jet. Once the expansion rate is known, the diffusive effects and chemical reactions are considered at the mixing layer itself in what is called the *1-D Lagrangian Diffusion-Reaction* (LDR) model. A derivation and explanation of the model is provided in Section 2.2. This technique permits us to use much higher resolution than previous studies. In this model, this mixing layer, at the jet head, is advected as a series of Lagrangian fluid particles of fixed mass. The evolution of its thermo-chemical structure can thus be readily obtained. The key physical processes in the problem are identified to be the mixing of the two gases at the mixing layer, the initial heating by the shock wave, and a cooling effect due to the expansion of the mixing layer. Specifically, the shock induced heating is evaluated by solving the well known shock tube problem (Liepmann and Rhoshko 2001) in terms of the initial storage pressure ratio. This provides the initial conditions at the mixing layer. The chemical reactions at the mixing layer are computed using the chemical kinetic mechanism developed by Li, et al. (2004) in order to capture high pressure reactions. Details of the mechanism are given in Section 2.4.6.

Thermodynamic properties are computed using the Cantera software package (Goodwin 2009) and the molecular mixing process is solved exactly using the mixture-averaged transport properties of each chemical species (Kee, et al. 2000). The expansion process of the hydrogen jet is prescribed as a source term from data obtained from the compressible flow solver for non-reacting releases. Finally, an approximate model that reacts a single Lagrangian particle with a pre-determined, highly reactive, mixture of fuel and air up to the point of ignition is also developed using the *Homogenous Mixing Ignition* (HMI) method (Echekki and Chen 2003; Knikker, et al. 2003) in order to study the significance of mixing in the hydrogen ignition problem. The HMI model is also explained in Section 2.2. The numerical methods applied to these localized one-dimensional models are explained in Chapter 3. The numerical experiments conducted, including results and discussion, are explained in Chapter 4. Finally conclusions and recommendations for further research are presented in Chapter 5.

Chapter 2

The Hydrogen Release Problem

2.1 Evolution of the Flow During an Accidental Release

When a high pressure gas is suddenly discharged into air, a highly unsteady under-expanded jet forms. In the initial stage of release, the expanding high pressure gas acts as a piston which drives a strong shock ahead of the jet into the lower pressure gas (Radulescu and Law 2007). The initial strength of the incident shock is governed by the *shock tube problem* (Liepmann and Rhoshko 2001). As the lead shock emerges from the orifice through which it is discharged, it diffracts around the corners (Ishii, et al. 1999), giving rise to a rounded spherical shape. This can be seen in experimental releases of helium into nitrogen conducted by Lacerda (1987), shown in Figure 2.1, and also for the experimental release of hydrogen into oxygen conducted by Wolanski and Wojcicki (1973), shown in Figure 2.2. Also shown in Figure 2.2 is the trajectory of the hydrogen jet interface, where the gases are mixing and reacting. Clearly, from the figure, the size of the mixing layer is very thin compared to the overall size of the jet itself, especially at early times. If the size of the mixing layer is much smaller than the size of the blast wave itself, then the diffusive fluxes and reacting chemistry within the mixing layer, prior to ignition, can be assumed not to affect the large-scale gas dynamics of the hydrogen jet release.

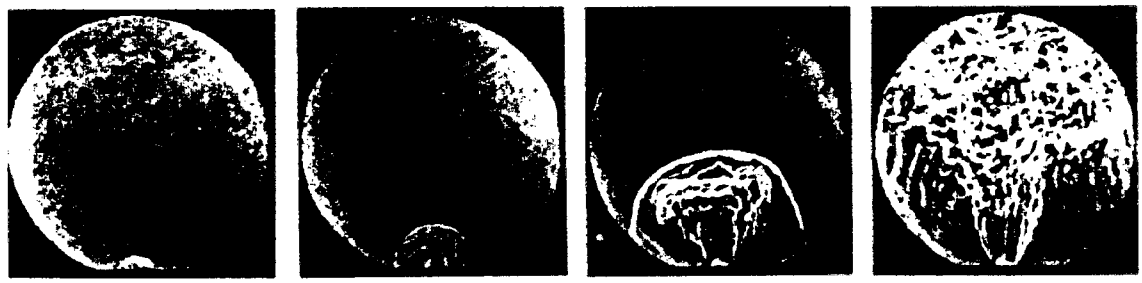

Figure 2.1: Release of high pressure helium into nitrogen. This Schlieren photograph is taken from Lacerda (1987) and is representative of a non-reactive hydrogen jet flowing into air. Clearly the expanding helium drives a strong shock which has a rounded spherical shape.

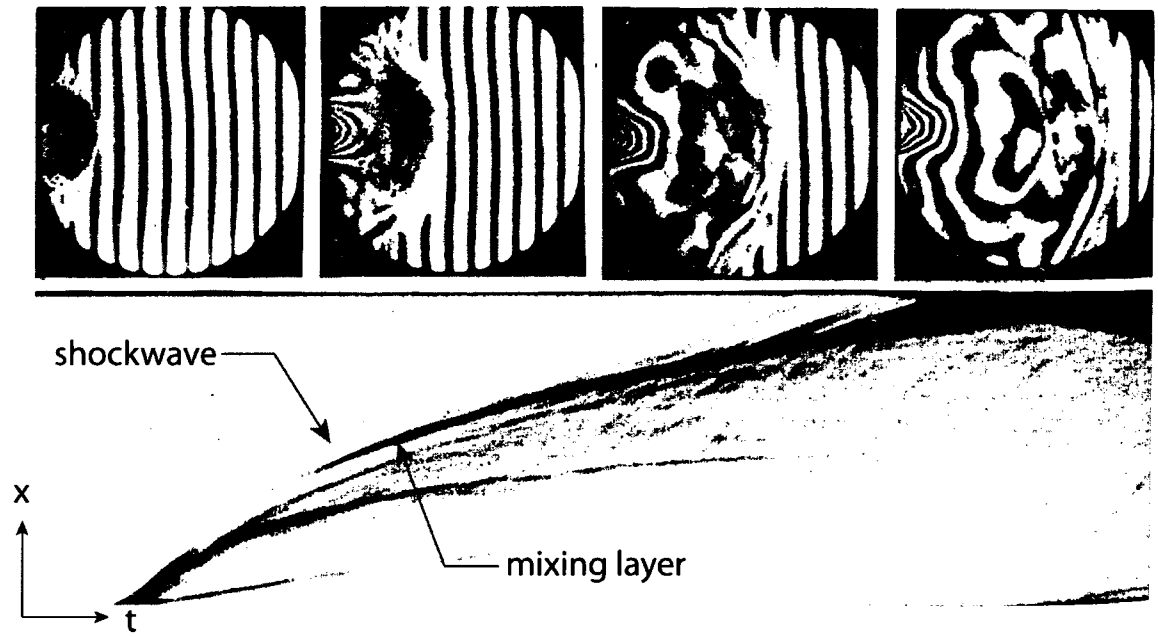

Figure 2.2: Release of high pressure hydrogen into oxygen. The intererometric photographs (top) and Schlieren streak photograph (bottom) is taken from Wolanksi and Wojciki (1973). The top frames show the rounded spherical shape of the lead shock wave. The Shlieren streak photograph on the bottom shows the trajectory of the lead shock, marked by the line that separates the white region by the grey undisturbed area, and also the trajectory of the mixing layer, represented by the upper most dark line.

By making use of the thin mixing layer assumption, the expansion rate at the head of the jet can be obtained numerically through a non-reactive compressible flow solver by treating the mixing layer as a discontinuity of negligible thickness in the simulation. Once

the expansion rate is known, the diffusive effects and chemical reactions can then be considered at the mixing layer itself in a highly localized one-dimensional model, described in Section 2.4. This is the approach recommended by Radulescu and Law (2007) and adapted in this study for solving the diffusion ignition problem of an expanding jet. To demonstrate that the thin mixing layer assumption holds up to the point of ignition, a simple order of magnitude justification is given in Section 2.3. Other important mixing layer assumptions, the *low Mach number approximation* (Paolucci 1982) for example, are also applied to the mixing layer in order to simplify the governing equations of the localized one-dimensional diffusion-reaction model. These other mixing layer assumptions are also described in section 2.3. First, however, the non-reactive gas dynamic model, for obtaining the expansion rate at the head of the jet, is briefly explained.

2.2 Non-Reactive Gas Dynamic Model

Currently, the evolution of the flow for the start up of an unreactive unsteady under-expanded jet can be modelled numerically using the *inviscid*, *perfect gas* (Thompson 1988) assumptions. The governing equations are the *Euler equations*, shown below in equations 2.1 through 2.3. This numerical approach has been shown to predict the gas dynamics in the early stages of the unsteady jet quite well when compared against experimental results (Ishii, et al. 1999). Furthermore, it has been demonstrated that the gas dynamics of the unsteady jet release problem are self-similar such that the problem can be scaled for any jet size and strength (Radulescu and Law 2007). An example of a simulation for an non-reactive hydrogen jet released into air is shown below in Figure 2.3. This particular figure shows the temperature profile of the flow field during release. Higher temperatures are shown in

lighter shades. In the figure, it is clearly visible that the air is shocked to a high temperature, followed by the cool, expanding hydrogen. The region where ignition is likely to occur is where the hot air mixes with hydrogen at the head of the jet, indicated in Figure 2.3. The simulation in Figure 2.3 is modelled using the Amrita computational facility (Quirk 1998a; Quirk 1998b). The conservation equations for mass, momentum, and energy are solved using a Lax-Friedrichs solver which is based on Godunov's method for solving compressible flow problems using a finite volume approach (Leveque 2002). The resolution of the simulation is 512 grid points across the diameter of hole. Initial and boundary conditions are shown in Figure 2.4.

Conservation of mass:

$$\frac{\partial \rho}{\partial t} + \nabla \cdot (\rho \vec{u}) = 0 \qquad \textbf{2.1}$$

Conservation of momentum:

$$\frac{\partial (\rho \vec{u})}{\partial t} + \nabla \cdot (\rho \vec{u}\vec{u}) + \nabla p = 0 \qquad \textbf{2.2}$$

Conservation of energy:

$$\frac{\partial (\rho e)}{\partial t} + \nabla \cdot \left((\rho e + p)\vec{u}\right) = 0 \qquad \textbf{2.3}$$

The total *specific energy*, e, which contains *internal* and *kinetic energy* components is given by:

$$e = \frac{p/\rho}{\gamma - 1} + \frac{1}{2}u^2 \qquad \textbf{2.4}$$

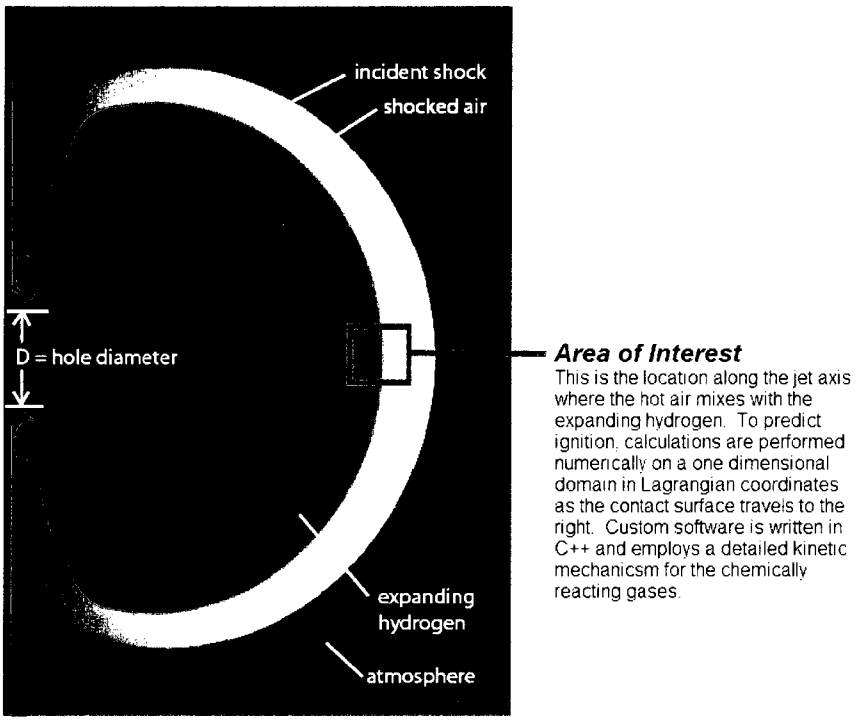

Figure 2.3: Temperature profile during a non-reactive release of hydrogen into the atmosphere. Lighter shades represent higher temperatures. The numerical simulation was run using the AMRITA language (Quirk 1998a; Quirk 1998b) to solve the Euler equations at a resolution of 512 grid points across the orifice. The initial pressure of the tank in this figure is 300 atmospheres.

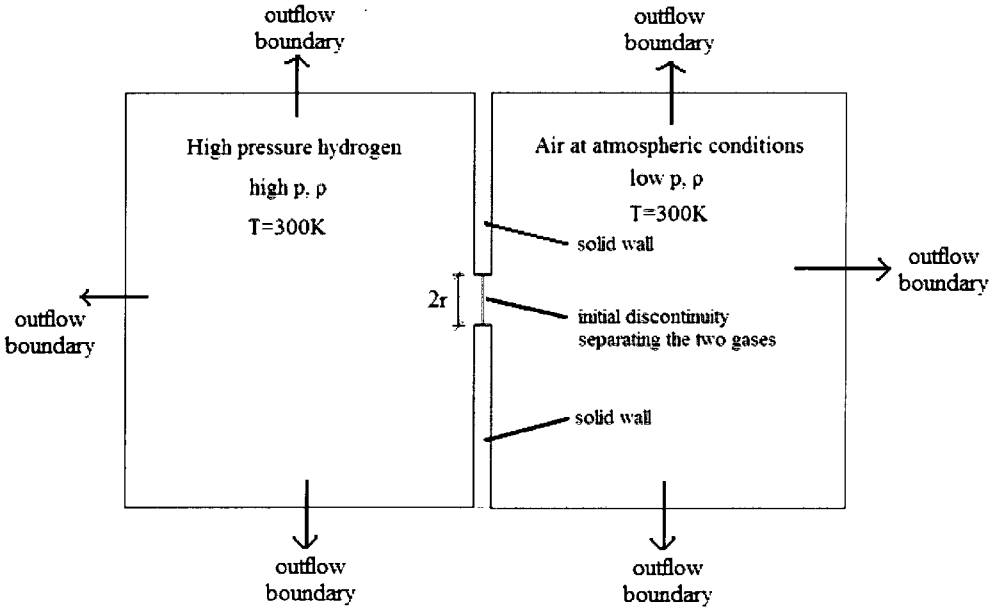

Figure 2.4: Initial conditions for non-reactive hydrogen release problem. The computational domain is zoomed in near the release hole. It should be noted that the storage tank in the simulation is assumed to be much larger than the release hole.

2.3 Mixing Layer Assumptions

2.3.1 Thin Mixing Layer

In order for inviscid, non-reactive, compressible flow solvers to be used to solve the gas dynamics of the release problem, specifically the expansion rate in the mixing layer, it must be shown that the size of the mixing layer is negligible compared to the overall size of the blast wave itself. To show this we let R be the size of the blast wave and δ be the size of the mixing layer, as shown in Figure 2.5. If $\frac{\delta}{R} \ll 1$, then the mixing layer can be treated as a discontinuity in the non-reactive multi-dimensional simulations and thus diffusion and chemical reactions in the mixing layer can be neglected.

The size of the mixing layer, δ, is controlled by the diffusivity of the gases, α. In this analysis, α is assumed to be equal and constant for both gases. An order of magnitude approximation for the size of the mixing layer, as a function of time, is given by

$$\delta \cong \sqrt{\alpha t} \tag{2.5}$$

From the analysis of unsteady jets (Radulescu and Law 2007) it can be shown that the position of the interface located at point i in Figure 2.5, normalized by the hole radius, r, for round jets as a function of time can be approximated by

$$\bar{x}_i = \frac{x_i}{r} \cong C\left(\frac{t a_{Ao}}{r}\right)^{1/2}\left(\frac{p_{Ao}}{p_{Bo}}\right)^{1/4} \tag{2.6}$$

where x_i is the distance of point i from the hole and C is a constant whose value is equal to

$$C = \left(\left(\frac{\bar{W}_A}{\bar{W}_B}\right) 6A^2 \left(\frac{\gamma_A + 1}{\gamma_A - 1}\right)^{1/2}\left(\frac{2}{\gamma_A + 1}\right)^{\gamma_A/(\gamma_A - 1)}\right)^{1/4} \approx 1 \tag{2.7}$$

Also, 'A' and 'B' refer to hydrogen and air, respectively, 'o' denotes the initial undisturbed state, and Λ is a constant whose value is $\Lambda = 1.2$ for round jets, and $\overline{W}$ refers to the molecular weight of gas A and B. To a first approximation, the position of the shock wave, or size of the blast wave, R, can be approximated by

$$R \approx x_i \qquad \textbf{2.8}$$

Therefore, the size of the mixing layer compared to the blast is given by

$$\frac{\delta}{R} \approx \left(\frac{\alpha}{r a_{Ao}}\right)^{1/2} \left(\frac{p_{Ao}}{p_{Bo}}\right)^{-1/4} \qquad \textbf{2.9}$$

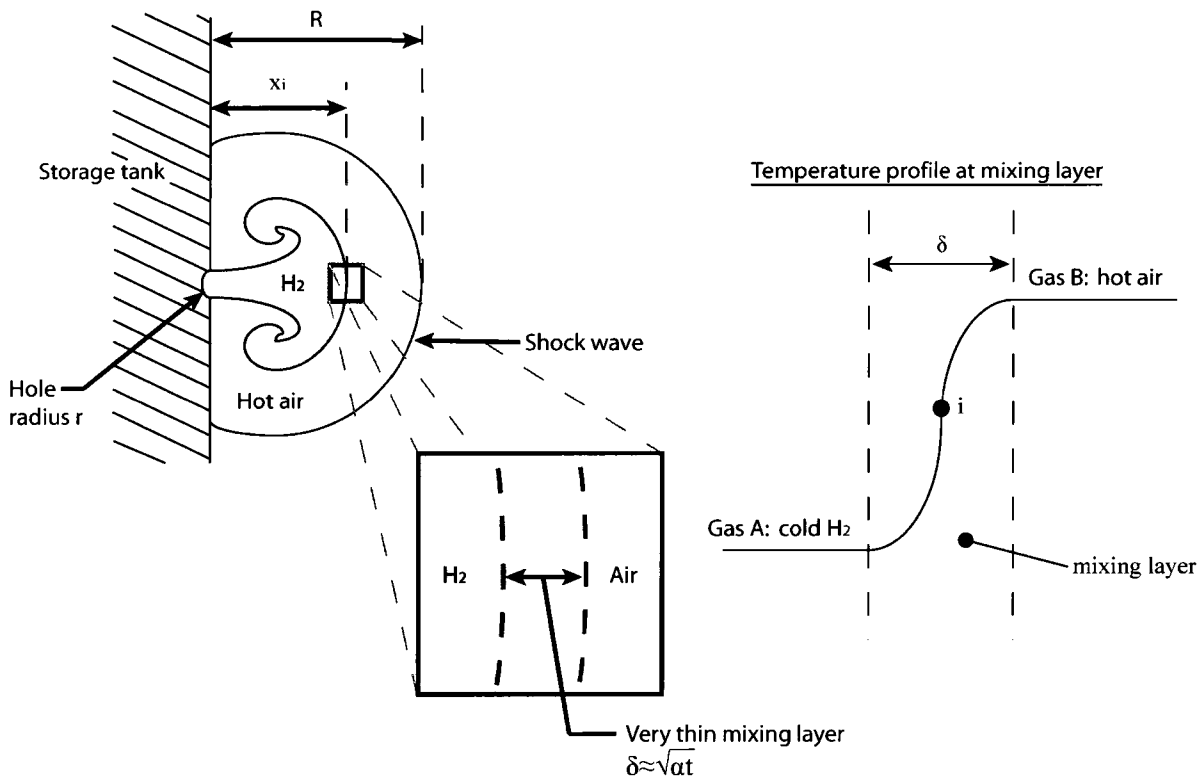

Figure 2.5: Pictorial sketch of hydrogen release showing the size of the blast wave (R) the size of the mixing layer (δ), and the position of the interface 'i' separating the two gases (x_i). Also shown is the expected temperature profile in the mixing layer prior to ignition.

Since the velocity of the blast wave for a supersonic jet is on the order of the sound speed, a_{Ao}, the size of the mixing layer compared to the size of the blast wave is related through the Reynolds number and initial storage pressure.

$$\frac{\delta}{R} \approx R_e^{-1/2} \left(\frac{p_{Ao}}{p_{Bo}}\right)^{-1/4} \qquad \textbf{2.10}$$

Clearly, the ratio δ/R has the strongest dependence on the Reynolds number. Therefore, for large Reynolds numbers associated with high speed flow ($R_e \gg 1$), then

$$\frac{\delta}{R} \ll 1$$

For example, in our case characteristic values are: $\alpha \sim 1 \times 10^{-4}\text{m}^2/\text{s}$, $r \sim 1 \times 10^{-4}\text{m}$, and $a_{Ao} \sim 1000\text{m/s}$. Therefore, $R_e \sim 1000$ and $\frac{\delta}{R} \sim 0.001$. Thus the size of the mixing layer is negligible compared to the blast wave itself.

2.3.2 Low Mach Number Approximation

If the *low Mach number approximation* is made within the mixing layer, then the problem can be simplified since local pressure gradients in the mixing layer are negligible. For example, see Paolucci (1982). Specifically, the low Mach number approximation assumes that acoustic pressure waves travel much faster than the flow itself. For example, consider an expanding piston/cylinder arrangement, shown in Figure 2.6. The motion of the piston sends pressure waves into the fluid which causes the gas to expand. Normally the pressure is a function of space and time, $p = p(x,t)$, however if these pressure waves are much faster than the motion of the cylinder itself $(u_{ac} \gg u_p)$, the pressure can be

approximated by a function of time only, $p = p(t)$. Thus the pressure gradients vanish and the flow becomes *isobaric* ($\nabla p = 0$). This can be attributed to the fact that the acoustic time scale for pressure waves to travel within the cylinder is much smaller than the time scale associated with the motion of the piston, giving rise to an instantaneous change in pressure uniformly throughout the cylinder due to the fast gas dynamic relaxation.

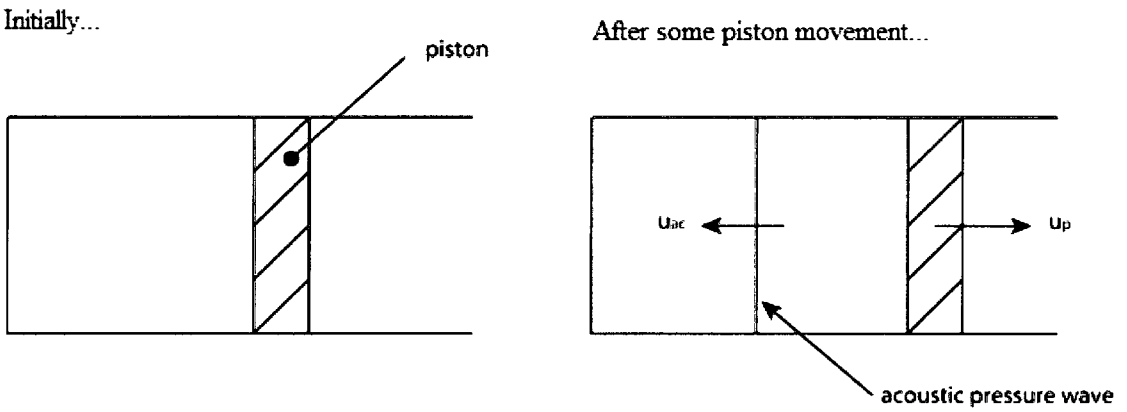

Figure 2.6: Expanding piston example. A piston that is impulse to velocity u_p sends an acoustic pressure wave into the gas at velocity u_{ac} telling the gas to expand and occupy more space.

Although the velocity of the jet itself is close to sonic speeds in the hydrogen release problem, it can be shown that the low Mach number approximation can be applied within the mixing layer. To demonstrate that this assumption holds for the hydrogen release problem it is necessary to show that the time scale associated with acoustic pressure waves passing through the mixing layer, t_{ac}, is much smaller than the time scale associated with expansion of the mixing layer itself, t_{flow}. Thus, it is necessary to show that $\frac{t_{ac}}{t_{\text{flow}}} \ll 1$.

First, consider the *acoustic time scale.* The time for an acoustic pressure wave to travel across the mixing layer can be approximated by

$$t_{ac} = \frac{\delta}{a_i} \qquad 2.11$$

where the characteristic length, δ, is the size of the mixing layer, and is given by equation 2.5.

Next consider the *flow time scale* due to expansion. Consider the points A and B, shown below in Figure 2.7. In the frame of reference of the jet head (point *i*), the points A and B will move in opposite directions with velocities u_A and u_B, respectively due to expansion. Therefore, the rate at which the fluid located at both boundaries pulls away from each other is characterized by $\Delta u = u_B - u_A$. This represents the maximum flow velocity difference in the mixing layer as a result of expansion. Thus the flow time scale is approximated by

$$t_{\text{flow}} = \frac{\delta}{\Delta u} \qquad 2.12$$

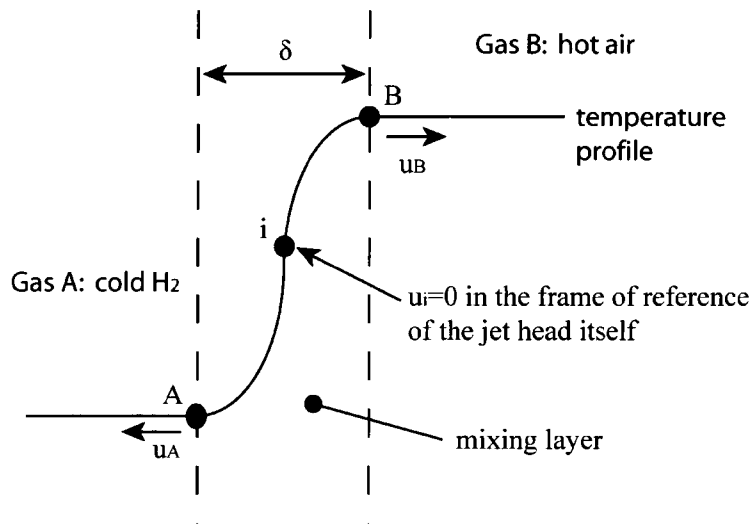

Figure 2.7: Mixing layer at head of the jet undergoing expansion. Points A and B move away from point i at velocities u_A and u_B, respectively, in the frame of reference of the jet head itself.

From the conservation of mass in one-dimension at the head of the jet

$$\left.\frac{D\rho_i}{Dt}\right|_{x=0} = -\rho_i \left.\frac{\partial u}{\partial x}\right|_{x=0} \qquad \textbf{2.13}$$

where the jet head is located at $x = 0$ in the frame of reference of the jet head itself. Here, $\left.\frac{\partial u}{\partial x}\right|_{x=0}$ can be approximated by

$$\left.\frac{\partial u}{\partial x}\right|_{x=0} \approx \frac{\Delta u}{\delta} \qquad \textbf{2.14}$$

Therefore the flow time scale, equation 2.12, can be written

$$t_{\text{flow}} = -\rho_i \left(\frac{D\rho_i}{Dt}\right)^{-1} = -\left(\frac{D(\ln \rho_i)}{Dt}\right)^{-1} \qquad \textbf{2.15}$$

Since the flow is isentropic

$$\frac{p_i}{\rho_i^{\gamma}} = \text{constant} \qquad \textbf{2.16}$$

therefore

$$t_{\text{flow}} = -\left(\frac{D(\ln p_i)}{Dt}\right)^{-1} \qquad \textbf{2.17}$$

According to numerical simulations conducted in this study, the pressure at the head of the jet can be approximated by a power law expression with the form shown below in equation 2.18. The actual correlation obtained in this study is given in Section 2.4.5.

$$p_i = Kt^{-n} \tag{2.18}$$

Here K is a constant and n is an exponent whose value can be worked out to be $n \approx 1$ analytically from Radulescu and Law (2007). Therefore from equations 2.17 and 2.18

$$t_{\text{flow}} \cong t \tag{2.19}$$

Therefore

$$\frac{t_{ac}}{t_{\text{flow}}} \cong \frac{\delta/a_i}{t} \cong \sqrt{\frac{\alpha}{a_i^2 t}} = \sqrt{\left(\frac{\alpha}{a_i r}\right)\left(\frac{r}{a_i t}\right)} \tag{2.20}$$

First we note that we have recovered the Reynolds number in equation 2.20 since

$$R_e \cong \frac{ar}{\alpha} \tag{2.21}$$

where it is assumed that the speed of sound at point i is approximated by $a_i = a_{Ao} = a$.

We also note that the second term, $\frac{r}{a_i t}$, also appears in equation 2.6 such that

$$\left(\frac{r}{a_i t}\right)^{1/2} \cong \frac{r}{x_i}\left(\frac{p_{Ao}}{p_{Bo}}\right)^{1/4} \tag{2.22}$$

Therefore

$$\frac{t_{ac}}{t_{\text{flow}}} \cong {R_e}^{-1/2}\left(\frac{r}{x_i}\right)\left(\frac{p_{Ao}}{p_{Bo}}\right)^{1/4} \tag{2.23}$$

Thus for large Reynolds number ($R_e \gg 1$) and for small hole sizes compared to the size of the blast wave $\left(\frac{r}{R} \cong \frac{r}{x_i} \ll 1\right)$ it is expected that

$$\frac{t_{ac}}{t_{\text{flow}}} \ll 1$$

since there is a weak dependence on storage pressure. Therefore, the low Mach number approximation holds within the mixing layer and the flow can be treated as isobaric such that $\nabla p = 0$.

2.3.3 Other Mixing Layer Assumptions

The following is a list of assumptions that are made in order to simplify the analysis of the diffusive and reactive mixing layer for the hydrogen release problem that is studied. Many of the assumptions are found in Warnatz, et al. (2006) for their derivation of the conservation equations for laminar premixed flames. According to Warnatz and co-authors, these assumptions lead to reasonable predictions of laminar flames and is therefore adopted accordingly in this study.

- The gases within the mixing layer are assumed to behave ideally such that pressure, temperature, and density are related through the *ideal gas law* (Çengel and Boles 2002).

$$\frac{p}{\rho} = \frac{R^o T}{\bar{W}} \qquad \textbf{2.24}$$

- External body forces (i.e. gravity) acting on the fluid are negligible. Thus if the external force acting on the ith chemical species is f_i, then $f_i = 0$ for all *i*.
- Heat flux due to radiation is negligible. Therefore $q_{rad} = 0$.

- *Dufour effects* are neglected as the contribution of energy is usually quite small (Law 2006). The Dufour effect $\left(R^o T \sum_{i=1}^{N} \sum_{j=1}^{N} \frac{X_j D_{T,i}}{\omega_i D_{i,j}} \left(\vec{u}_{d,i} - \vec{u}_{d,j}\right)\right)$ arises due to concentration gradients giving rise to thermal flux (Law 2006). Dufour effects are also neglected in many 1-D flame codes and numerical studies (Al-Khateeb, et al. 2007; Dixon-Lewis 1967; Goodwin 2009; Kee, et al. 2000; Rogg and Wang 1995).
- Finally, viscous dissipation effects are neglected since there are no significant shear stresses expected in the mixing layer.

2.4 Localized One-Dimensional Model

The reaction-diffusion-expansion phenomenon, following a bounded one-dimensional domain, which encompasses the turbulent mixing layer at the head of the jet, is governed by the conservation of momentum, energy, and the conservation of mass of each chemical species within the fluid particle. The equations are first presented in *Eulerian coordinates*, in the frame of reference of the jet head itself. Full derivations can be found in many combustion textbooks (Law 2006; Toong 1983; Warnatz, et al. 2006; Williams 1985). The equations are then transformed into *Lagrangian coordinates* using the transformation approach by Rogg and Wang (1995). In Eulerian coordinates the flow is described in terms of spatial coordinates (i.e. Cartesian coordinates). In Lagrangian coordinates, however, the flow is tracked for individual fluid particles of fixed mass. Lagrangian coordinates are particularly useful for keeping track of the gas as it gas expands and occupies more space. In the Eulerian approach, information is lost as mass flows out of the specified control

volumes to occupy more space during expansion. An illustration comparing the two different approaches is shown below in Figure 2.8.

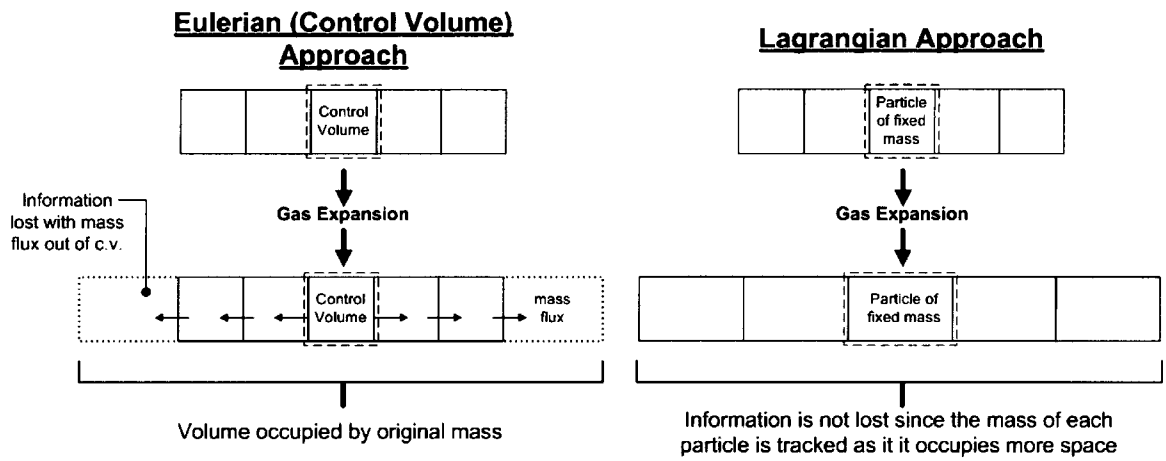

Figure 2.8: Eulerian (control volume) approach vs. Lagrangian approach for derivation of the governing equations.

2.4.1 Governing Equations in Eulerian Form

2.4.1.1 Conservation of Mass

The continuity equation, equation 2.25, is simply the rate at which mass changes with time per unit volume, plus the mass flux through the control volume is zero.

$$\frac{\partial \rho}{\partial t} + \nabla \cdot \rho \vec{u} = 0 \qquad 2.25$$

Alternatively, the continuity equation can be written in terms of the *material derivative*:

$$\frac{D\rho}{Dt} + \rho \nabla \cdot \vec{u} = 0 \qquad 2.26$$

where $\frac{D\rho}{Dt}$ is the change of density with respect to time for a fluid particle with a fixed mass.

2.4.1.2 Conservation of Mass of the ith Species

The change of mass of the *i*th species for a fluid particle is given by equation 2.27 where ω_i is the net rate of production of the *i*th species, and $\vec{u}_{d,i}$ is the diffusional velocity of the *i*th species.

$$\rho \frac{DY_i}{Dt} = \omega_i - \nabla \cdot \rho Y_i \vec{u}_{d,i} \qquad \textbf{2.27}$$

2.4.1.3 Conservation of Momentum

Newton's second law of motion states that the rate of change of momentum of a particle, or acceleration of the particle times the mass, is equal to the sum of the forces acting on the particle. The change in momentum for a fluid particle can be written

$$\rho \frac{D\vec{u}}{Dt} = -\nabla p - \nabla \cdot \bar{\bar{\tau}} + \sum_{i=1}^{N} \rho_i f_i \qquad \textbf{2.28}$$

where $\rho \frac{D\vec{u}}{Dt}$ is the change of momentum with respect to time for a fluid particle with a fixed mass, ∇p is the net force, due to hydrostatic pressure, acting on the fluid per unit volume, and $\nabla \cdot \bar{\bar{\tau}}$ is the contribution of viscous forces acting on the fluid per unit volume.

2.4.1.4 Conservation of Energy

The conservation of energy for a fluid particle of fixed mass has many forms. It can be written in terms of total energy (internal energy + kinetic energy), internal energy only, enthalpy, and entropy. Since the gas in the mixing layer is assumed to behave like an ideal gas, then a useful form of the energy equation can be written in terms of temperature. For an *ideal gas* (Çengel and Boles 2002; Warnatz, et al. 2006)

$$dh_i = c_{p,i} dT \qquad \textbf{2.29}$$

Thus temperature is related to enthalpy through equation 2.29. Furthermore, integrating equation 2.29 yields the *caloric equation of state* (Law 2006):

$$h_i = h_i^o + \int_{T_o}^{T} c_{p,i} dT \tag{2.30}$$

where h_i^o is the specific heat of formation for the *i*th species and is taken at $T_o = 298K$. The conservation of energy in terms of temperature, as derived by Toong (1983), is shown below in equation 2.31. It should be noted that the assumptions from section 2.3 have not yet been applied to the equation shown below.

$$\rho c_p \frac{DT}{Dt} = \frac{Dp}{Dt} - \sum_{i=1}^{N} h_i \omega_i + \nabla \cdot k\nabla T - \sum_{i=1}^{N} \rho Y_i c_{p,i} \vec{u}_{d,i} \nabla T$$
$$-\nabla \cdot R^o T \sum_{i=1}^{N} \sum_{j=1}^{N} \frac{X_j D_{T,i}}{\omega_i D_{i,j}} \left(\vec{u}_{d,i} - \vec{u}_{d,j}\right) - \nabla \cdot \vec{q}_{rad} + \phi + \sum_{i=1}^{N} \left(\vec{u}_{d,i}\right) \cdot \rho_i \vec{f}_i \tag{2.31}$$

Here the rate of change of enthalpy for a fluid particle of fixed mass $\left(\rho c_p \frac{DT}{Dt}\right)$, is governed by the rate of change of energy in a fluid particle due to expansion $\left(\frac{Dp}{Dt}\right)$, the rate of change of energy due to chemical reactions $(\sum_{i=1}^{N} h_i \omega_i)$, the diffusion of heat $(\nabla \cdot k\nabla T)$, rate of change of energy due to radiation $(\nabla \cdot \vec{q}_{rad})$, work done on the fluid particle due to external forces $\left(\sum_{i=1}^{N} \left(\vec{u}_{d,i}\right) \cdot \rho_i \vec{f}_i\right)$, and viscous dissipation (ϕ). Also contributing to the rate of change of energy of a fluid particle is the DuFour effect, and a secondary diffusion term that arises due to differences in diffusional velocities and temperature gradients amongst each species in the fluid particle $\left(\sum_{i=1}^{N} \rho Y_i c_{p,i} \vec{u}_{d,i} \nabla T\right)$.

2.4.1.5 Conservation Equations in 1-D Form with Mixing Layer Assumptions

The mixing layers assumptions from Section 2.3.2 and 2.3.3 are applied to equations 2.26, 2.27, 2.28, and 2.31 in order to simplify the problem. The resulting equations in 1-D Eulerian coordinates are presented below.

Conservation of Mass:

$$\frac{D\rho}{Dt} = -\rho\frac{\partial u}{\partial x} \tag{2.32}$$

Conservation of Mass of the ith Species:

$$\rho\frac{DY_i}{Dt} = \omega_i - \frac{\partial\left(\rho Y_i u_{d,i}\right)}{\partial x} \tag{2.33}$$

Conservation of Momentum:

$$\rho\frac{D\vec{u}}{Dt} = -\nabla p \approx 0 \tag{2.34}$$

Conservation of Energy:

$$\rho c_p\frac{DT}{Dt} = \frac{\partial p}{\partial t} - \sum_{i=1}^{N} h_i\omega_i + \frac{\partial}{\partial x}\left(k\frac{\partial T}{\partial x}\right) - \sum_{i=1}^{N}\rho Y_i c_{p,i} u_{d,i}\frac{\partial T}{\partial x} \tag{2.35}$$

It should be noted that applying the low Mach number approximation and neglecting external body forces leads to a de-coupling of the conservation of momentum from the other governing equations. Furthermore, the conservation of species, equation 2.33 already takes into account the conservation of mass, equation 2.32. Therefore, only the conservation of mass for each species, equation 2.33, and the conservation of energy, equation 2.35, need to be solved.

2.4.2 Governing Equations in Lagrangian coordinates (LDR Model)

As mentioned previously, it is useful to transform the governing equations into Lagrangian coordinates in order to keep track of the gas as it gas expands and occupies more space. The transformation is done using the same approach by Rogg and Wang (1995) where the Eulerian coordinates are transformed into mass-weighted Lagrangian coordinates

$$(x,t) \rightarrow (m,z) \tag{2.36}$$

First, the time variable is transformed simply by

$$z = t \tag{2.37}$$

where z is the Lagrangian time coordinate. The spatial coordinate, x, is transformed into a mass-based coordinate, m, by integrating the density from some reference coordinate, x_o, to x.

$$m(x,t) = \int_{x_o}^{x} \rho(x,t)dx \tag{2.38}$$

At this point, it is useful to take the time and spatial derivatives of 2.38 separately while holding the other variable constant:

$$\left.\frac{\partial m}{\partial x}\right|_t = \rho \tag{2.39}$$

$$\left.\frac{\partial m}{\partial t}\right|_x = \frac{\partial}{\partial t}\int_{x_o}^{x} \rho(x,t)dx \tag{2.40}$$

By applying the *Leibniz rule* (Lopez 2001) and noting that x is independent of t, equation 2.40 becomes:

$$\left.\frac{\partial m}{\partial t}\right|_x = \int_{x_o}^{x} \frac{\partial \rho}{\partial t} dx \qquad \textbf{2.41}$$

From applying the definition of the *material derivative* to the continuity equation,2.32

$$\frac{\partial \rho}{\partial t} = -\left(u\frac{\partial \rho}{\partial x} + \rho\frac{\partial u}{\partial x}\right) \qquad \textbf{2.42}$$

Therefore, plugging equation 2.42 into equation 2.41 yields

$$\left.\frac{\partial m}{\partial t}\right|_x = -\rho u + \dot{m}_o \qquad \textbf{2.43}$$

where, $\dot{m}_o$ is a constant and is interpreted as the initial mass flow rate of a fluid particle at its initial position.

$$\dot{m}_o = \rho u|_{x_o} \qquad \textbf{2.44}$$

By using equations 2.39 and 2.43, we can use the *chain rule* and the definition of the material derivative to find the corresponding transformations for the Eulerian differentials:

$$\left.\frac{\partial}{\partial x}\right|_t = \rho \left.\frac{\partial}{\partial m}\right|_z \qquad \textbf{2.45}$$

$$\frac{D}{Dt} = \dot{m}_o \left.\frac{\partial}{\partial m}\right|_z + \left.\frac{\partial}{\partial z}\right|_m \qquad \textbf{2.46}$$

Using the transformations from equations 2.45 and 2.46, and assuming that the initial velocity field is zero everywhere in the frame of reference of the jet head such that $\dot{m}_o = 0$, then the conservation equations, 2.33 and 2.35, are transformed into the following equations:

Conservation of Mass of the ith Species:

$$\rho \frac{\partial Y_i}{\partial z} = \omega_i - \rho \frac{\partial \left(\rho Y_i u_{d,i}\right)}{\partial m} \qquad \textbf{2.47}$$

Conservation of Energy:

$$\rho c_p \frac{\partial T}{\partial \mathrm{z}} = \frac{\partial p}{\partial \mathrm{z}} - \sum_{i=1}^{N} h_i \omega_i + \rho \frac{\partial}{\partial m}\left(k\rho \frac{\partial \mathrm{T}}{\partial \mathrm{m}}\right) - \sum_{i=1}^{N} \rho^2 Y_i c_{p,i} u_{d,i} \frac{\partial \mathrm{T}}{\partial \mathrm{m}} \qquad \textbf{2.48}$$

These two equations, 2.47 and 2.48, shall be referred to throughout the remainder of the thesis as the *1-D Lagrangian Diffusion-Reaction* (LDR) model. Mixture-averaged transport properties, explained in the next section, are used to calculate the diffusional velocities and thermal conductivity. The boundary and initial conditions are explained later in this chapter as well as how the expansion rate of the gas is prescribed. The numerical techniques used for solving these equations are described in detail in Chapter 3. Finally, another model is proposed in Section 2.4 which further simplifies the governing equations as an alternative method.

2.4.3 Mixture-Averaged Transport Properties

For calculating transport properties of the gasses (i.e. diffusion velocities of each species, thermal conductivities, and viscosities), two methods have been developed by Kee et al. (2000) for systems containing multiple reacting chemical species. The first method is the mutli-component set of formulas which is based on the approach used by Dixon-Lewis (1968) and Williams (1985) for calculating the transport properties of each chemical species at the molecular level (Hirschfelder, et al. 1954). The second method for approximating for the transport properties is the mixture-averaged formulas described by Coffee and Heimerl

(1981). In these mixture-averaged approximations, the overall average transport properties are determined for the entire mixture, rather than for each chemical species. While the multi-component method produces more realistic and accurate results, it is at a disadvantage since it requires more time to compute a solution (Kee, et al. 2000). For this study, only the mixture-averaged formulas were used since they provide a good estimate for the transport properties and were much less expensive to employ. Below is a summary of the formulas used for calculating the diffusion velocities of each chemical specie as well as the thermal conductivity of the mixture. Since viscous effects are neglected in the mixing layer, the formulas for calculating the viscosity of the mixture are not required.

Velocity of the ith species:

The total velocity of species i is simply the sum of average velocity of the flow, $\vec{u}$, and the diffusion velocity, $\vec{u}_{d,i}$.

$$\vec{u}_i = \vec{u} + \vec{u}_{d,i} \qquad \textbf{2.49}$$

Diffusion Velocity:

The diffusion velocity of each species, $u_{d,i}$, within a control volume is made up of 3 components. They are 1) ordinary diffusion velocity, $u_{od,i}$, 2) thermal diffusion velocity, $w_{d,i}$, and 3) a correction velocity, u_c, which is necessary for the mixture-averaged approximation.

$$u_{d,i} = u_{od,i} + w_{d,i} + u_c \qquad \textbf{2.50}$$

Ordinary Diffusion Velocity:

The ordinary component of the diffusion velocity is a component of the total diffusion velocity that arises due to gradients in species concentration and pressure gradients (Kee, et al. 2000).

$$u_{od,i} = -\frac{1}{X_i} D_{im} \vec{d}_i \qquad \textbf{2.51}$$

where D_{im}, is a mixture-averaged diffusion coefficient and

$$\vec{d}_i = \nabla X_i + (X_i - Y_i)\frac{\nabla p}{p} \qquad \textbf{2.52}$$

Since the low Mach number approximation is applied in the mixing layer, then $\nabla p = 0$. Therefore, in 1-D Eulerian coordinates:

$$\vec{d}_i = \frac{\partial X_i}{\partial x} \qquad \textbf{2.53}$$

Furthermore, equation 2.53 is transformed into Lagrangian coordinates using the transformation in equation 2.45. Therefore

$$\vec{d}_i = \rho \frac{\partial X_i}{\partial m} \qquad \textbf{2.54}$$

Thermal Diffusion Velocity:

The thermal diffusion velocity is a component of the diffusion velocity that arises due to gradients in temperature. In a multi-component model this term would normally be included. However in the mixture-averaged approximation, it is assumed that the contribution of thermal diffusion velocity is negligible (Coffee and Heimerl 1981).

Therefore

$$w_{d,i} \approx 0 \tag{2.55}$$

Correction for Mixture-Averaged Diffusion Velocity:

Since the mixture-averaged formulas for diffusion velocity are not exact, a correction is required. This correction ensures that the conservation of mass of each chemical species is not violated (Coffee and Heimerl 1981; Kee, et al. 2000).

$$u_c = -\sum_{i=1}^{N} Y_i\left(u_{od,i} + w_{d,i}\right) \tag{2.56}$$

This ensures that the net species diffusion flux of all chemical species is zero, such that

$$\sum_{i=1}^{N} Y_i u_{d,i} = 0 \tag{2.57}$$

Thermal Conductivity:

The overall thermal conductivity of the gas, k, is obtained through equation 2.58 (Kee, et al. 2000).

$$k = \frac{1}{2}\left(\sum_{i=1}^{N} X_i k_i + \frac{1}{\sum_{i=1}^{N} X_i/k_i}\right) \tag{2.58}$$

Here, k_i is the thermal conductivity of the ith species.

2.4.4 Initial and Boundary Conditions

To determine the initial boundary conditions of the problem, the properties of the hot air and cold fuel on each side of the contact surface are found by solving the *shock tube problem* (Liepmann and Rhoshko 2001). In this case, however, the shock tube problem is solved by taking realistic thermal properties into account. The solutions across the shock discontinuity and expansion fan are found using the numerical methods described by Browne, et al. (2008) and iterated until the pressure and velocity at the contact surface are matched. For a detailed explanation of the process and the algorithm used refer to Appendix A. Furthermore, boundaries are specified to have zero gradients. The initial temperatures of the air and hydrogen at the boundaries of the mixing layer as a function of storage pressure are shown below in Figure 2.9. Also, the initial pressure of the mixing layer is shown as a function of storage pressure in Figure 2.10.

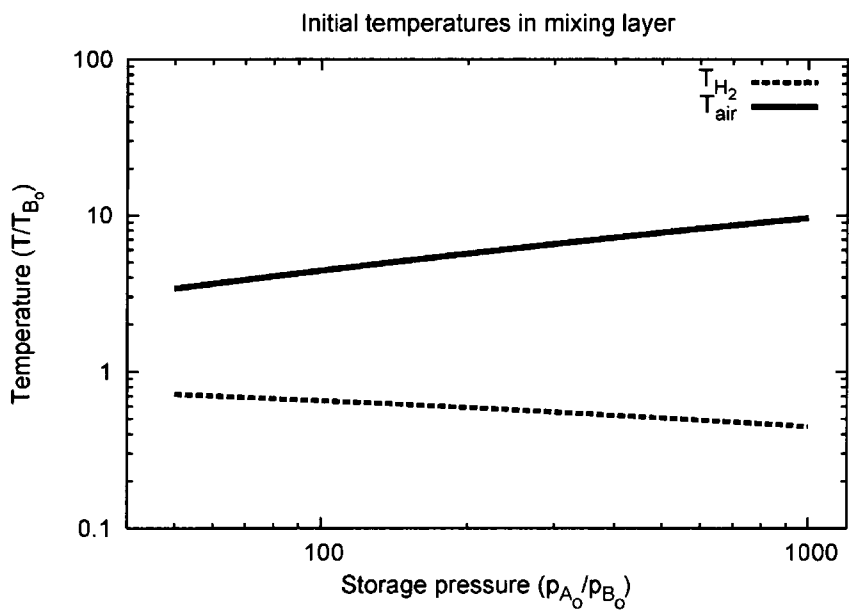

Figure 2.9: Initial temperatures of hydrogen and air at the boundaries, normalized by the temperature of the ambient air, T_{B_o}, as a function of storage pressure, $\frac{p_{Ao}}{p_{Bo}}$. The solutions are obtained by solving the shock tube problem for various storage pressures and taking realistic chemistry into account.

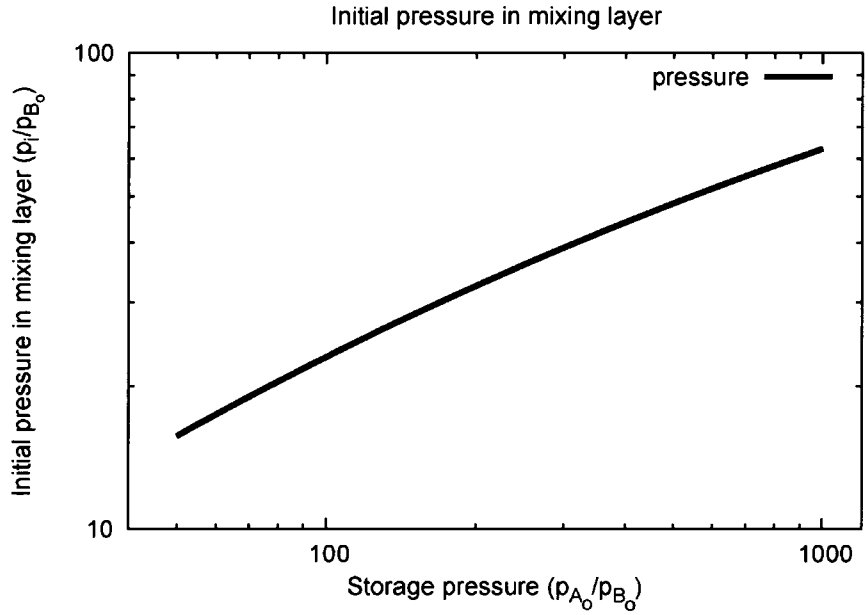

Figure 2.10: Initial pressure of the mixing layer, p_i, normalized by the pressure of the ambitent air, p_{B_o}, as a function of storage pressure, $\frac{p_{Ao}}{p_{Bo}}$. The solution is obtained by solving the shock tube problem for various storage pressures and taking realistic chemistry into account.

For the initial conditions of the *Lagrangian reaction-diffusion* (LDR) model, each half of the domain consists of the same gas located at the respective boundaries. However, rather than separate the two gases by a discontinuity, a smoothing function is applied at time zero across 6 grid points to avoid computational difficulties that may arise from computing the initial infinite gradients. The smoothing function applied is simply the solution to the diffusion equation given by the error function, shown in equation 2.59. This approach was also used by Knikker, et al. (2003) and the smoothing function is given below.

$$z = \frac{1}{2}\left[1 + \mathrm{erf}\left(\frac{m - m_o}{d}\right)\right] \qquad \textbf{2.59}$$

Here, z is the mixture fraction, or mass fraction, of the fuel (H_2) in the mixture (Knikker, et al. 2003). Thus $z = 0$ for pure air and $z = 1$ for pure fuel. Furthermore, m is the Largrangian coordinate, m_o is the midpoint in the domain. Finally, d is the number of grid points across which the smoothing function is applied (d=6 in this case). The species mass fractions and enthalpy are then determined at each grid point using equations 2.60 and 2.61. The temperature at each grid point can then be computed with Cantera (Goodwin 2009) since Y_i, h, and p are known everywhere.

$$Y_i = zY_{i,\text{fuel}} + (1 - z)Y_{i,\text{air}} \qquad \textbf{2.60}$$

$$h = zh_{\text{fuel}} + (1 - z)h_{\text{air}} \qquad \textbf{2.61}$$

A pictorial diagram showing the computational domain with the initial and boundary conditions is shown below in Figure 2.11. For the shock tube problem, the pressure of the ambient air is taken to be 1 atm and the initial temperatures of both gasses are assumed to be 300K.

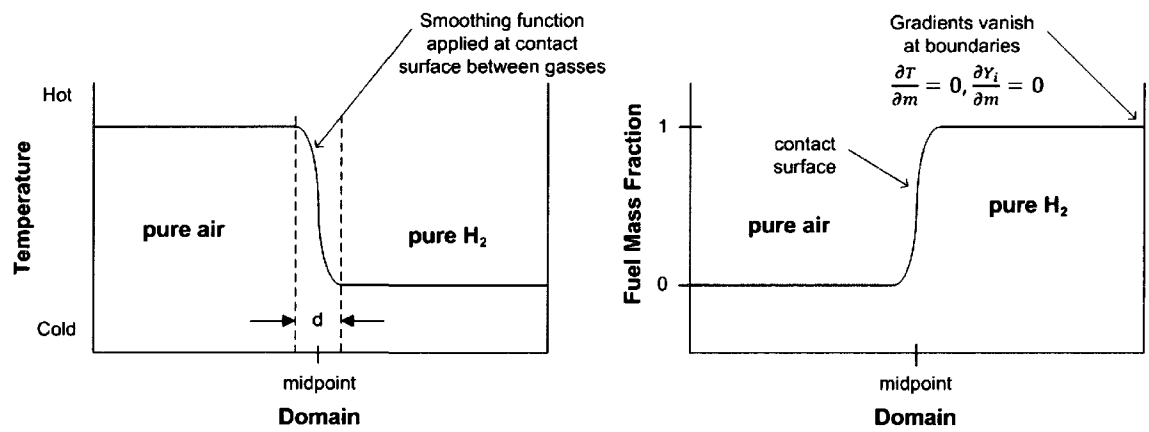

Figure 2.11: Initial and boundary conditions for the one-dimensional LDR Model. Also shown in the figure is the smoothing function that is applied at the contact surface between the two gasses in order to avoid computational errors associated with sharp, infinite, gradients discontinuities.

2.4.5 Expansion Rate

Radulescu and Law (2007) have previously determined the scaling parameters for under-expanded, non-reactive hydrogen jets both analytically and using a compressible flow solver for non-reacting releases. In their non-dimensional analysis, the pressure-time history at the interface between the gasses for different jet conditions was found to be well approximated by a unique relation. The rate at which the pressure at the interface decays in terms of the non-dimensional time scaling parameter, τ, is shown in Figure 2.12, both analytically and numerically. This scaling parameter, τ, was found to depend on the discharge flow rate, and hence the size of the hole through which the gas escapes as well as the chocked velocity at the hole. Their analytical model, however, did not correlate exactly with the solutions obtained from compressible flow solver simulations. Therefore, in this thesis, the unique relation describing the pressure at the interface, p_i, in terms of τ and regardless of the initial pressure ratio, $\frac{p_{Ao}}{p_{Bo}}$, is found by curve-fitting the numerical results and is shown in Figure 2.12. The unique relation was found to have a power-law form and is given by equation 2.62.

$$\frac{p_i}{p_{Bo}} = 12.2\tau^{-0.68} \qquad \textbf{2.62}$$

Here the scaling parameter, τ, is given by

$$\tau = \left(\left(\frac{\rho_{Bo}}{\rho_{Ao}}\right)\left(\frac{2}{\gamma_A + 1}\right)^{-1/(\gamma_A - 1)}\right)^{1/2} \frac{t a_{Ao}}{r\Lambda}\left(\frac{2}{\gamma_A + 1}\right)^{1/2} \qquad \textbf{2.63}$$

where 'A' and 'B' refer to hydrogen and air, respectively, 'o' denotes the initial undisturbed state, r is the radius of the hole through which hydrogen escapes from the tank, and Λ is a

constant whose value is $\Lambda = 1.2$ for round jets. Therefore, the rate of change of pressure at the jet head is then simply the time derivative of p_i.

$$\frac{\partial p}{\partial z} = \frac{\partial p_i}{\partial \tau}\frac{\partial \tau}{\partial z} = -8.3 p_{Bo}\tau^{-1.68}\frac{\partial \tau}{\partial z} \qquad \textbf{2.64}$$

Where $\frac{\partial \tau}{\partial z}$ is simply the time derivative of equation 2.63, noting that $t = z$.

$$\frac{\partial \tau}{\partial z} = \left(\frac{\rho_{Bo}}{\rho_{Ao}}\left(\frac{2}{\gamma_A + 1}\right)^{-1/(\gamma_A - 1)}\right)^{1/j}\frac{a_{Ao}}{r\Lambda}\left(\frac{2}{\gamma_A + 1}\right)^{1/2} \qquad \textbf{2.65}$$

Furthermore, at the onset of release there is initially a period where the pressure at the interface remains constant. This can clearly be seen for the case where $\frac{p_{Ao}}{p_{Bo}} = 88$ in Figure 2.12. The reason for this initial period of constant pressure is due to the time required for information regarding expansion at the corner of the hole to reach the location of the particle along the axis of the jet. To account for this delay, the value of τ is calculated for when $\frac{p_i}{p_{Bo}}$ is equal to the initial pressure of the jet head, obtained through the shock tube solution. The simulations are then started at time zero of the release process, incorporating this period of constant pressure.

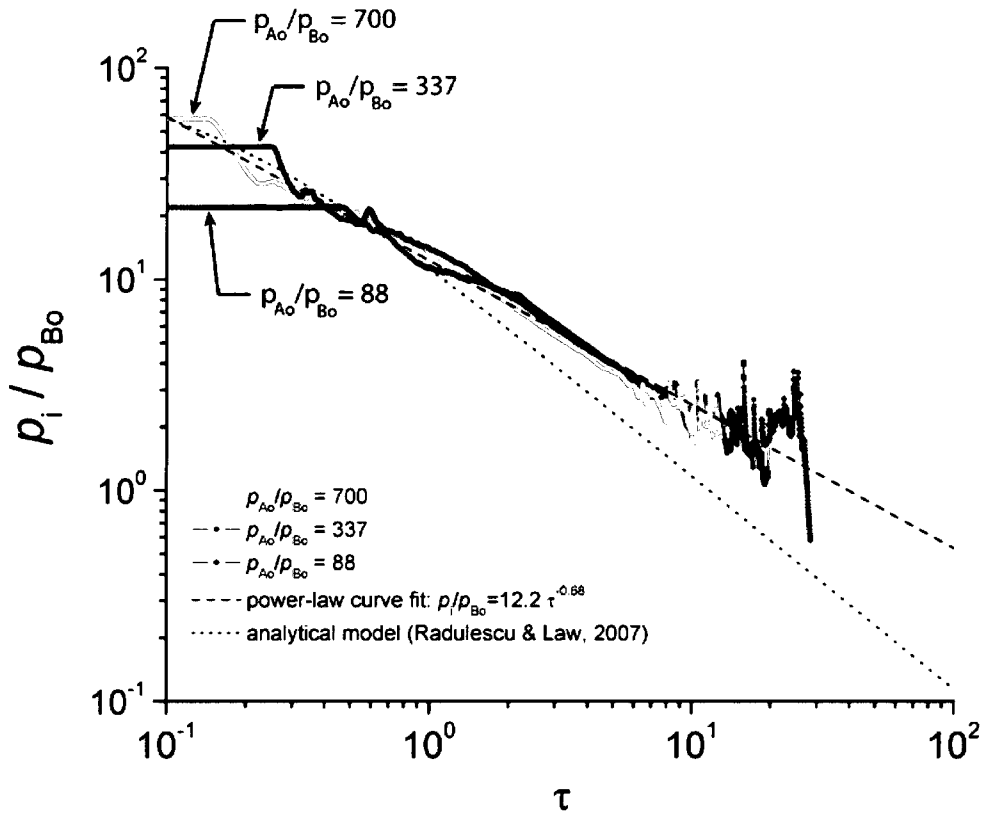

Figure 2.12: Evolution of the contact surface pressure along the jet axis for round jets. Results were obtained numerically for various storage pressure to ambient pressure ratios from Radulescu and Law (2007).

2.4.6 Reaction Mechanism for Hydrogen Combustion

In order to compute the thermodynamic properties ($c_{p,i}$, h_i, etc...) and production rates of each chemical species, ω_i, a reaction mechanism is required which provides the details of reactions involved including the required thermo chemical data. The reaction mechanism chosen for this study is the mechanism developed by Li, et al. (2004) that is specifically designed for hydrogen combustion. The reaction mechanism contains 19 reactions, shown in Table 2.1, and 11 chemical species.

To see how production rates of each chemical species, ω_i, are computed using the reaction mechanism in Table 2.1, consider the *elementary reaction* (Kee, Rupley and Meeks, et al. 1996) involving *I* species and *N* reactions

$$\sum_{i=1}^{I} v'_{ni}\chi_i \leftrightarrow \sum_{i=1}^{I} v''_{ni}\chi_i \qquad (n = 1, \ldots, N)$$

Here v'_{ni} is the stoichiomentric coefficient of the *i*th reactant species in the *n*th reaction, v''_{ni} is the stoichiometric coefficient of the *i*th product species in the *n*th reaction, and χ_i is the chemical symbol for the *i*th species (Kee, et al. 1996). The overall stoichiometric coefficient for the *i*th species in the *n*th reaction is simply

$$v_{ni} = v''_{ni} - v'_{ni} \qquad \textbf{2.66}$$

The net production rate of species *i*, involving *N* reactions, is calculated from

$$\omega_i = \sum_{n=1}^{N} v_{ni} q_n \qquad \textbf{2.67}$$

where $q_n$is the rate of progress variable for the *n*th reaction and is given by equation 2.68 for elementary reactions. For equations pertaining to the rate of progress variables for *three body* or *falloff* reactions see the Kee, et al. (1996).

$$q_n = k_{f_n} \prod_{i=1}^{I} [X_i]^{v'_{ni}} - k_{r_n} \prod_{i=1}^{I} [X_i]^{v''_{ni}} \qquad \textbf{2.68}$$

Here $[X_i]$ is the molar concentration of the *i*th species.

Table 2.1: Detailed H_2/O_2 Reaction Mechanism from Li, et al. (2004).

			A_n	β_n	E_n	Reaction Type
H2/O2 chain reactions						
1.	H + O2 = O + OH		3.55×10^{15}	−0.41	16.60	elementary
2.	O + H2 = H + OH		5.08×10^{4}	2.67	6.29	elementary
3.	H2 + OH = H2O +H		2.16×10^{8}	1.51	3.43	elementary
4.	O + H2O = OH + OH		2.97×10^{6}	2.02	13.40	elementary
H2/O2 dissociation/recombination reactions						
5.	H2 + M = H + H + M[a]		4.58×10^{19}	−1.40	104.38	three-body
	H2 + Ar = H + H + Ar		5.84×10^{18}	−1.10	104.38	elementary
	H2 + He = H + H + He		5.84×10^{18}	−1.10	104.38	elementary
6.	O + O + M = O2 + M[a]		6.16×10^{15}	−0.50	0.00	three-body
	O + O + Ar = O2 + Ar		1.89×10^{13}	0.00	−1.79	elementary
	O + O + He = O2 + He		1.89×10^{13}	0.00	−1.79	elementary
7.	O + H + M = OH + M[a]		4.71×10^{18}	−1.0	0.00	three-body
8.	H + OH + M = H2O + M[b]		3.8×10^{22}	-2.00	0.00	three-body
Formation and consumption of HO2						
9.	H + O2 + M = HO2 + M[c]	k0	6.37×10^{20}	−1.72	0.52	fall-off
	H + O2 + M = HO2 + M[d]	k0	9.04×10^{19}	−1.50	0.49	fall-off
		k∞	1.48×10^{12}	0.60	0.00	
10.	HO2 + H = H2 + O2		1.66×10^{13}	0.00	0.82	elementary
11.	HO2 + H = OH + OH		7.08×10^{13}	0.00	0.30	elementary
12.	HO2 + O = OH + O2		3.25×10^{13}	0.00	0.00	elementary
13.	HO2 + OH = H2O + O2		2.89×10^{13}	0.00	−0.50	elementary
Formation and consumption of H2O2						
14.	HO2 + HO2 = H2O2 + O2[e]		4.20×10^{14}	0.00	11.98	elementary
	HO2 + HO2 = H2O2 + O2		1.30×10^{11}	0.00	−1.63	elementary
15.	H2O2 + M = OH + OH + M[f]	k0	1.20×10^{17}	0.00	45.50	fall-off
		k∞	2.95×10^{14}	0.00	48.40	
16.	H2O2 + H = H2O + OH		2.41×10^{13}	0.00	3.97	elementary
17.	H2O2 + H = H2 + HO2		4.82×10^{13}	0.00	7.95	elementary
18.	H2O2 + O = OH + HO2		9.55×10^{6}	2.00	3.97	elementary
19.	H2O2 + OH = H2O + HO2[e]		1.00×10^{12}	0.00	0.00	elementary
	H2O2 + OH = H2O + HO2		5.8×10^{14}	0.00	9.56	elementary

Units are cm³-mol-s-kcal-K, and $k = A_n T^{\beta_n} exp(-E_n/R^o T)$

a Efficiency factors are: $\varepsilon_{H2O} = 12.0$, $\varepsilon_{H2} = 2.5$, $\varepsilon_{Ar} = 0.75$, and $\varepsilon_{He} = 0.75$. When a rate constant is declared specifically for Ar or He collision partner, the efficiency of Ar or He is set to zero when determining M for the same reaction.

b Efficiency factors are $\varepsilon_{H2O} = 12.0$, $\varepsilon_{H2} = 2.5$, $\varepsilon_{Ar} = 0.38$, and $\varepsilon_{He} = 0.38$.

c When the main bath gas is N_2 (M = N_2). Troe parameter is $F_c = 0.8$. Efficiency factors are $\varepsilon_{H2O} = 11.0$, $\varepsilon_{H2} = 2.0$, and $\varepsilon_{O2} = 0.78$.

d When the main bath gas is Ar or He (M = Ar or He). Troe parameter is $F_c = 0.5$. Efficiency factors are $\varepsilon_{H2O} = 16.0$, $\varepsilon_{H2} = 3.0$, $\varepsilon_{O2} = 1.1$, and $\varepsilon_{He} = 1.2$.

e Reactions (14) and (19) are expressed as the sum of the two rate expressions.

f Troe parameter is $F_c = 0.5$. Efficiency factors are $\varepsilon_{H2O} = 12.0$, $\varepsilon_{H2} = 2.5$, $\varepsilon_{Ar} = 0.64$, and $\varepsilon_{He} = 0.64$.

The forward rate constant for the *n*th reaction has an Arrhenius dependence on temperature given by

$$k_{f_n} = A_n T^{\beta_n} \exp\left(\frac{-E_n}{R^o T}\right) \quad \textbf{2.69}$$

where, A_n, β_n, and E_n are the pre-exponential factor, the temperature exponent, and the activation energy, respectively (Kee, et al. 1996), and correspond to the values in Table 2.1 for each reaction involved. The reverse rate constant for the *n*th reaction is related to the forward rate constant through

$$k_{r_n} = \frac{k_{f_n}}{k_{c_n}} \quad \textbf{2.70}$$

where k_{c_n} is given by

$$k_{c_n} = \exp\left(\sum_{i=1}^{I} v_{ni} \frac{S_i^o}{R^o} - \sum_{i=1}^{I} v_{ni} \frac{H_i^o}{R^o}\right)\left(\frac{101.3\text{kPa}}{R^o T}\right)^{\Sigma_{i=1}^{I} v_{ni}} \quad \textbf{2.71}$$

where S_i^o and H_i^o are the entropy and enthalpy of formation of species i, respectively and are computed using the thermo-chemical data shown in Table 2.2.

Table 2.2: H_i^o (298.15), S_i^o (298.15), and C_p (T) for Species Considered in the H2/O2 Reaction Mechanism from Li, et al. (2004).

Species	H_i^o(298.15)	S_i^o(298.15)	C_p(300)	C_p (500)	C_p (800)	C_p (1000)	C_p (1500)	C_p (2000)
H	52.10	27.39	4.97	4.97	4.97	4.97	4.97	4.97
O	59.56	38.47	5.23	5.08	5.02	5.00	4.98	4.98
OH	8.91	43.91	7.16	7.05	7.15	7.34	7.87	8.28
H2	0.00	31.21	6.90	7.00	7.07	7.21	7.73	8.18
O2	0.00	49.01	7.01	7.44	8.07	8.35	8.72	9.03
H2O	-57.80	45.10	8.00	8.45	9.22	9.87	11.26	12.22
HO2	3.00	54.76	8.35	9.47	10.77	11.38	12.48	13.32
H2O2	-32.53	55.66	10.42	12.35	14.29	15.21	16.85	17.88
N2	0.00	45.77	6.95	7.08	7.50	7.83	8.32	8.60
Ar	0.00	36.98	4.97	4.97	4.97	4.97	4.97	4.97
He	0.00	30.12	4.97	4.97	4.97	4.97	4.97	4.97

Units are cal/mol/K for S_i^o and C_p, and kcal/mol for H_i^o.

2.5 Approximate Homogeneous Mixing Ignition Model (HMI Model)

To further simplify the problem, the ignition phenomenon is also modeled using the *homogenous mixing ignition* (HMI) method described in (Echekki and Chen 2003; Knikker, et al. 2003). Transport effects are implicitly taken into account by considering the ignition time history of a single constant mass particle with a representative fixed mixture fraction of fuel and air. In this model, the most reactive fuel to air mixture fraction is considered, since this is where the first ignition site would be likely to occur. This approximation is made by considering the activation energy asymptotics of ignition-diffusion problems where heat and mass diffuse at the same rate (Knikker, et al. 2003). Also, the approximation assumes that heat release plays a minor role prior to the ignition event. This approach has been shown to be a good approximation for predicting non-premixed hydrogen air ignition problems without expansion (Knikker, et al. 2003). Since transport effects are accounted for

implicitly, the diffusion terms are neglected. The resulting governing equations that are solved numerically for the approximate model are reduced to:

Conservation of Mass of the ith Species:

$$\rho \frac{\partial Y_i}{\partial z} = \omega_i \tag{2.72}$$

Conservation of Energy:

$$\rho c_p \frac{\partial T}{\partial z} = \frac{\partial p}{\partial z} - \sum_{i=1}^{N} h_i \omega_i \tag{2.73}$$

For the initial conditions, the most reactive mixture fraction, z, is found by reacting various mixtures of the two gases, computed from the shock tube problem as explained in Section 2.3.4, until the mixture with the smallest ignition delay is found. Ignition delay times for various mixtures of hot air and cold hydrogen are shown below in Figure 2.13 for a case where the storage pressure ratio is $\frac{p_{Ao}}{p_{Bo}} = 200$. The subscripts Ao and Bo refer to the initial states of the hydrogen and air respectively. In this particular case, for example, the most reactive mixture of the two gasses is found when $z = 0.0065$.

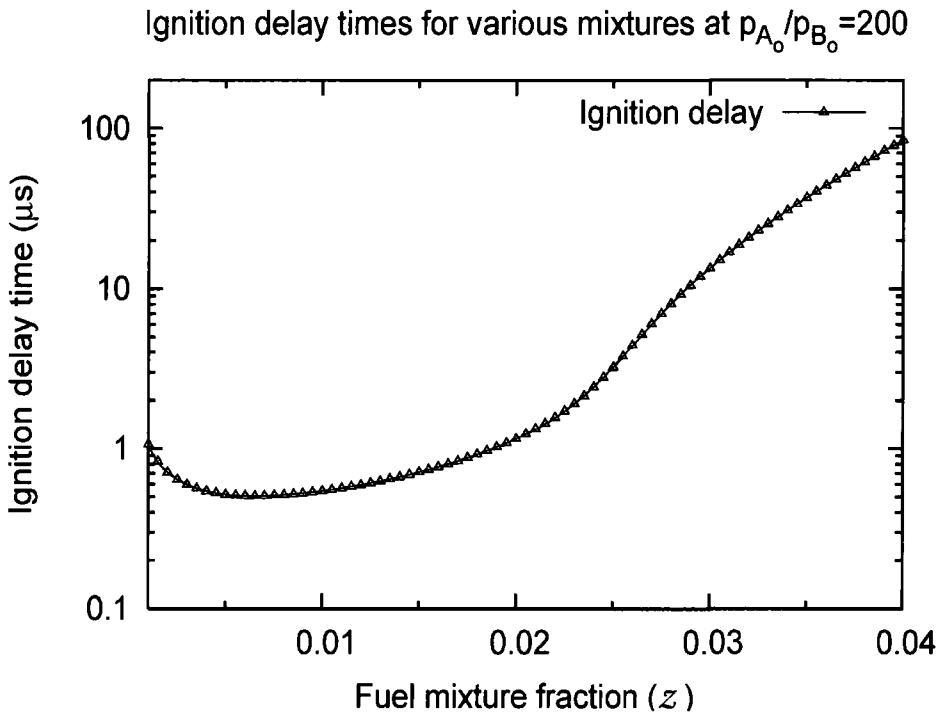

Figure 2.13: Ignition delay times for various mixture fractions of fuel to air for a case where $\frac{p_{Ao}}{p_{Bo}} = 200$. The subscripts *Ao* and *Bo* refer to the initial states of the hydrogen and air respectively.

Chapter 3

Numerical Methods

In this chapter, the numerical methods are described for both the 1-D *Lagrangian Diffusion-Reaction* (LDR) model and the approximate *homogeneous mixing ignition* (HMI) model. The solvers for both models are custom software, written in C++. Both models incorporate external libraries for evaluating thermodynamic and transport properties as well as an external solver for integrating the stiff chemistry. The thermodynamic and transport properties are evaluated at each time step and grid point using the Cantera libraries (Goodwin 2009) for C++. The kinetic mechanism used for calculating the reaction rates and thermodynamic data for each chemically reacting specie was developed by Li, et al. (2004) and is specifically designed for hydrogen chemistry. Details of the reaction mechanism are given in Section 2.3.6. Finally, the Sundials (Hindmarsh, et al. 2005) CVODE (Cohen and Hindmarsh 1996) integrator is used to handle integration of the stiff chemistry in the reaction terms of the governing equations.

3.1 Lagrangian Diffusion-Reaction Model (LDR Model)

3.1.1 Discretization

The governing equations are integrated numerically using an *operator splitting* technique (Leveque 2002) which solves the diffusion, reaction, and source terms separately over one time step. Each operation is solved *explicitly* based on information known from the previous operation as illustrated below in Figure 3.1. Once each of the three steps, explained below, are executed throughout a single time step, the process is repeated over the next time step. The size of each time step is governed by the diffusion step, as explained below. The operator-splitting process is similar to the process outlined in a paper written by Karasalo and Kurylo (1981). For this model, only equations 2.47 and 2.48 need to be solved. As mentioned in Chapter 2, the momentum equation, 2.34, is neglected and the conservation of mass, 2.32, is already accounted for in the conservation of species equation 2.47.

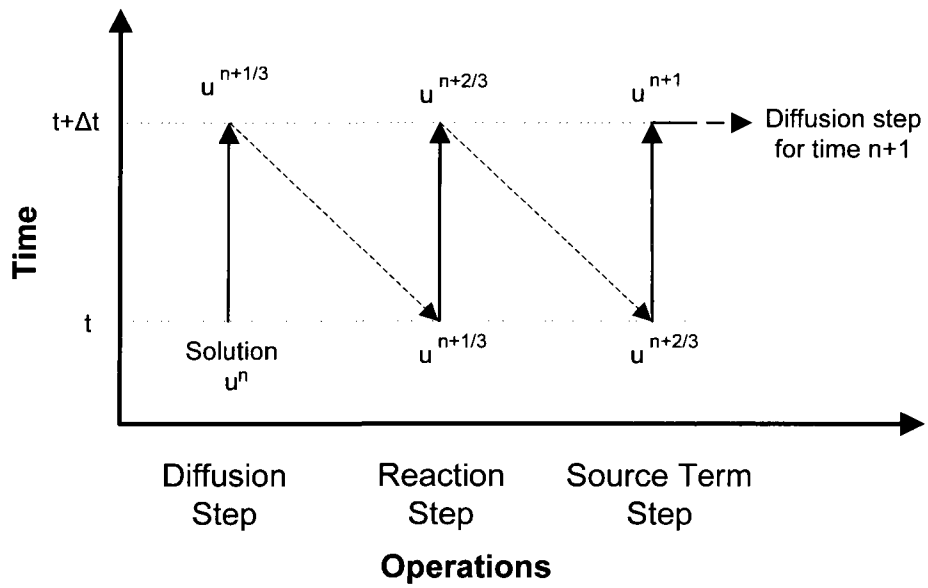

Figure 3.1: Operator splitting for the LDR model. Here, *u* is the solution at time step *n*.

Step 1: Diffusion Step

First the diffusive terms are solved over one whole time step. The equations that are solved in this step are:

$$\rho\frac{\partial Y_i}{\partial z} = -\rho\frac{\partial\left(\rho Y_i u_{d,i}\right)}{\partial m} \tag{3.1}$$

$$\rho c_p\frac{\partial T}{\partial z} = \rho\frac{\partial}{\partial m}\left(k\rho\frac{\partial T}{\partial m}\right) - \sum_{i=1}^{N}\rho^2 Y_i c_{p,i} u_{d,i}\frac{\partial T}{\partial m} \tag{3.2}$$

Equations 3.1 and 3.2 are discritized using *central difference* approximations (Anderson 1995) on the diffusive terms and *explicit time stepping* (Anderson 1995) for the unsteady terms. The diffusion velocities, $u_{d,i}$, are evaluated using the mixture-averaged formulas found in the previous chapter. Therefore, the spatial derivatives, including the spatial derivate found in the calculation of $\vec{d}_i$ in equation 2.50, are approximated by

$$\left(\frac{\partial T}{\partial m}\right)_j^n \approx \frac{T_{j+1}^n - T_{j-1}^n}{2\Delta m} \tag{3.3}$$

Similarly, the time derivatives are approximated by

$$\left(\frac{\partial T}{\partial z}\right)_j^n \approx \frac{T_j^{n+1} - T_j^n}{\Delta z} \tag{3.4}$$

In these two equations, j represents the current spatial node and n represents the current time step. Applying these discretizations to equations 3.1 and 3.2 allows us to calculate the species concentration and temperature for each node at the next time step explicitly based on the values known from the current time step. The resulting discretized equations for the species concentration and temperature at each node for the next time step are shown below.

$$Y_{i,j}^{n+1} = Y_{i,j}^n - (A - B)\frac{\Delta z}{\Delta m^2} \tag{3.5}$$

$$T_j^{n+1} = T_j^n + (C - D)\frac{\Delta z}{\Delta m^2} \tag{3.6}$$

where

$$A = \left(\rho^2 Y_i \left[-\frac{D_{im}}{X_i}\left(X_{i,j+1} - X_{i,j}\right) + \sum_{k=1}^{N} \frac{Y_k}{X_k} D_{km}\left(X_{k,j+1} - X_{k,j}\right)\right]\right)^n_{j+\frac{1}{2}} \quad \textbf{3.7}$$

$$B = \left(\rho^2 Y_i \left[-\frac{D_{im}}{X_i}\left(X_{i,j} - X_{i,j-1}\right) + \sum_{k=1}^{N} \frac{Y_k}{X_k} D_{km}\left(X_{i,j} - X_{i,j-1}\right)\right]\right)^n_{j-\frac{1}{2}} \quad \textbf{3.8}$$

$$C = \frac{1}{c_{p_j}}\left[(k\rho)^n{}_{j+\frac{1}{2}}\left(T^n{}_{j+1} - T^n{}_j\right) - (k\rho)^n{}_{j-\frac{1}{2}}\left(T^n{}_j - T^n{}_{j-1}\right)\right] \quad \textbf{3.9}$$

$$D = \frac{\rho_j^{n2}}{c_{p_j}}\left(\sum_{i=1}^{N}\left(Y_i c_{p,i}\left[\begin{array}{c}\sum_{k=1}^{N}\frac{Y_k}{X_k}D_{km}\frac{\left(X_{i,j+1}-X_{i,j-1}\right)}{2} \\ -\frac{D_{im}}{X_i}\frac{\left(X_{i,j+1}-X_{i,j-1}\right)}{2}\end{array}\right]\right)_j^n\right)\left(\frac{T^n{}_{j+1}-T^n{}_{j-1}}{2}\right) \quad \textbf{3.10}$$

The stability condition, or CFL number (Anderson 1995), at each node for equations 3.5 and 3.6, are calculated using equations 3.11 and 3.12, respectively.

$$CFL_{i,j} = \left(\frac{\rho^2 Y_i}{X_i} D_{im}\right)_j^n \frac{\Delta z}{\Delta m^2} \quad \textbf{3.11}$$

$$CFL_j = \left(\frac{k\rho}{C_p}\right)_j^n \frac{\Delta z}{\Delta m^2} \quad \textbf{3.12}$$

The size of the time step Δz is determined by the specified resolution Δm and ensuring that the maximum CFL number at any node (Anderson 1995) does not exceed

$$CFL_{\max} < 0.01 \quad \textbf{3.13}$$

It should be noted that this limit was found by trial and error in order to ensure that round off errors associated with the discretization do not grow with each calculation and cause the solution to become unstable (Anderson 1995). It should also be noted that for equations in the form of the diffusion equation,

$$\frac{\partial T}{\partial z} = \alpha \frac{\partial^2 T}{\partial m^2} \quad \textbf{3.14}$$

that are discretized using equations 3.3 and 3.4 have the stability requirement (Anderson 1995)

$$CFL_{\max} = \frac{\alpha \Delta z}{(\Delta m)^2} < 0.5 \qquad \textbf{3.15}$$

Therefore, the extra term in equation 3.2 is more difficult to compute and thus requires a much smaller time step than typical diffusion equations.

Step 2: Reaction Step

In step 2, the reaction terms are solved over the same time step using the solution obtained from step 1. The equations solved for this step are:

$$\rho \frac{\partial Y_i}{\partial z} = \omega_i \qquad \textbf{3.16}$$

$$\rho c_p \frac{\partial T}{\partial z} = -\sum_{i=1}^{N} h_i \omega_i \qquad \textbf{3.17}$$

In these equations, the production rate of specie i, ω_i, is dependent on the rate-of-progress of each reaction involving each chemical species (Kee, et al. 1996), which in turn has an Arrhenius dependence on temperature. The result is a very stiff set of equations that are highly coupled. To solve the system of equations, 3.16 and 3.17, the Sundials (Hindmarsh, et al. 2005) CVODE (Cohen and Hindmarsh 1996) integrator is used. This particular solver is specifically designed for solving stiff, nonlinear systems of equations *implicitly* for each time step using *Newton iteration* (Cohen and Hindmarsh 1996).

Step 3: Source Term Step

The expansion term, $\frac{\partial p}{\partial z}$, in the energy equation 2.48, is treated as a source term and is therefore evaluated independently of the other terms. In this step, the pressure is updated by using the solution obtained from the previous step and solving the following equation over the same time step:

$$\rho c_p \frac{\partial T}{\partial z} = \frac{\partial p}{\partial z} \qquad \textbf{3.18}$$

The expansion rate, $\frac{\partial p}{\partial z}$, is given in equation 2.64.

3.1.2 Validation (Flame Speed Calculation)

To validate the code, flame speed calculations were performed for an unsteady laminar premixed hydrogen flame at constant pressure. The homogeneous mixture used for the calculation was a stoichiometric mixture of hydrogen and air at 1 atm and 300K. The result is compared against the flame speed obtained using Cantera's built in steady flow solver (Goodwin 2009) for the same mixture. Mixture-averaged transport properties are used both for the LDR model and the Cantera simulation. The Cantera simulation is able to compute a steady solution with its finest grid resolved at $\Delta x = 8.0 \times 10^{-6}\text{m}$. Applying the transformation given in equation 2.38 at the minimum density gives us the corresponding resolution in Lagrangian coordinates: $\Delta m = 2.64 \times 10^{-6}\text{kg/m}^2$. The comparison between the two models is shown below in Figure 3.2. The *Lagrangian reaction-diffusion* (LDR) model was found to have a higher flame speed value than that calculated by Cantera. The reason for this is because the Cantera flame solver does not include the energy addition term,

$\rho^2 \frac{\partial T}{\partial m} \sum_{i=1}^{N} Y_i c_{p,i} u_{d,i}$, found in equations 2.48 and 3.2. When this term was neglected in the Lagrangian model, the flame speed was found to converge to the same flame speed calculated with Cantera, which was 2.4 m/s. Furthermore, a numerical study by Al-Khateeb, et al. (2007) found that the flamespeed in the same mixture was also 2.4m/s. The numerical model used by Al-Khateeb, et al. (2007) also neglected the energy addition term, $\rho^2 \frac{\partial T}{\partial m} \sum_{i=1}^{N} Y_i c_{p,i} u_{d,i}$. Therefore, the proposed LDR model is considered to be in good agreement with the benchmarks (Al-Khateeb, et al. 2007; Goodwin 2009) and is therefore considered to provide good results for the numerical experiments conducted in this study.

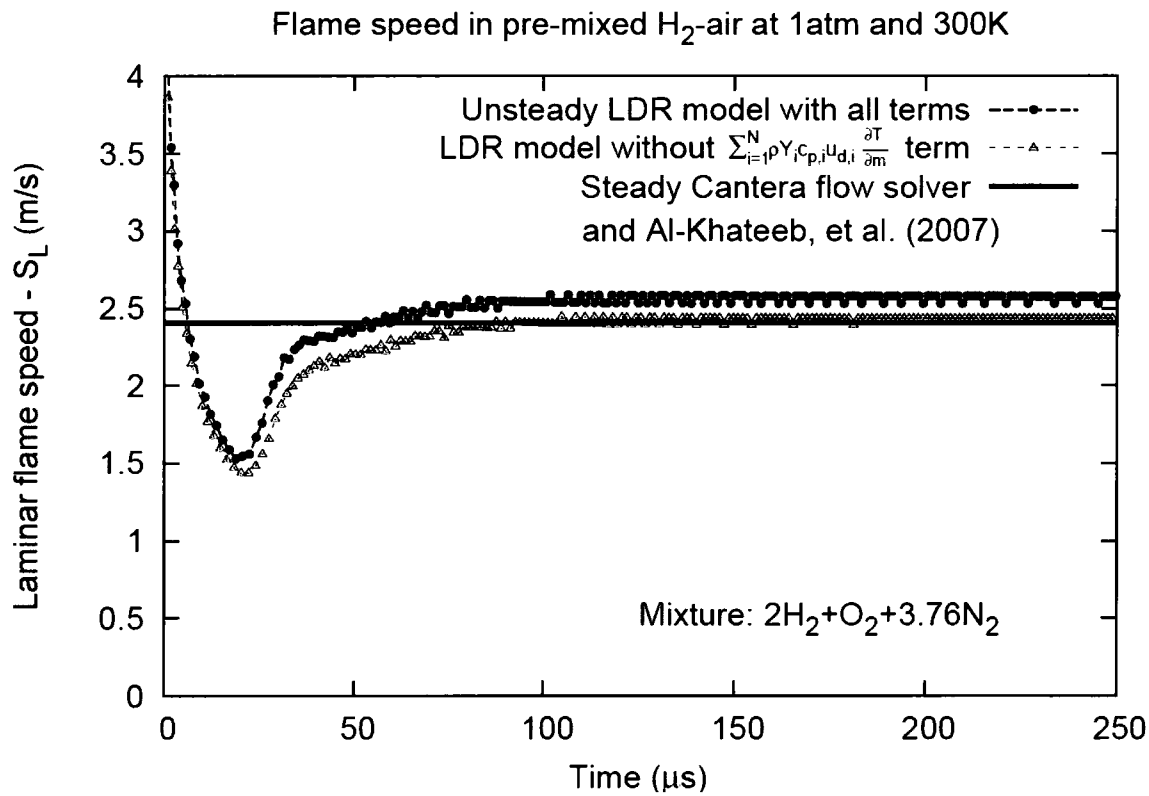

Figure 3.2: Flame speed calculation for a premixed stoichiometric mixture of hydrogen and air at 1 atm and 300K.

3.1.3 Resolution Study

Since the code has been validated against other numerical codes, it is useful to determine the resolution required, Δm, for converged solutions. Numerical experiments are conducted, simulating a release directly into air through a 2.5mm radius hole. The purpose of the experiment is to determine the storage pressure required in order for auto-ignition to occur at various spatial resolutions. In this experiment, expansion is taken into account. The results of the experiments are presented below in Table 3.1. A grid-independent solution was obtained when the resolution was set to $\Delta m = 2.5 \times 10^{-7}\text{kg/m}^2$. This resolution is in good agreement with the resolution used in the flame calculations. Also, this resolution corresponds to the required resolution of $\Delta x = 7.56 \times 10^{-6}\text{m}$ for hydrogen flame calculations predicted by Al-Khateeb, et al. (2007).

Table 3.1: Resolution study for hydrogen release into air through 2.5mm radius hole.

Resolution (Δm) in kg/m^2	Number of Nodes	Ignition Limit (atm)
4e6	501	127
2e-6	1001	124
2e-6	501	124
1e-6	1001	122
1e-6	501	122
5e-7	1001	121
2.5e-7	**2001**	**120**
1.25e-7	4001	120

3.2 Homogeneous Mixing Ignition Model (HMI Model)

3.2.1 Discretization

Equations 2.72 and 2.73 from the *homogenous mixing ignition* (HMI) model are solved numerically using the operator splitting technique described in section 3.1. For this model, however, step 1 (diffusion) is ignored since the equations do not contain diffusion terms. Therefore only steps 2 and 3, reaction step and source term step, are executed. Refer to Figure 3.3 for an illustration of the process. Furthermore, the time step required to produce converged, resolution independent results was found to be $\Delta z = 1 \times 10^{-10}$s.

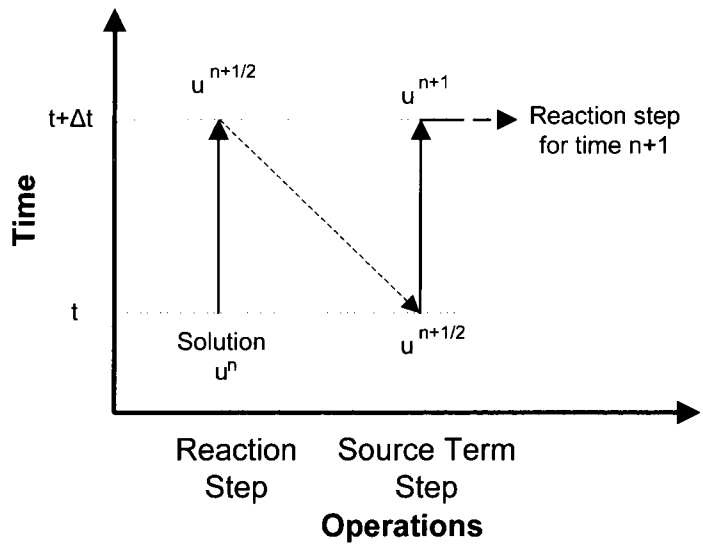

Figure 3.3: Operator splitting for the HMI model. Here, *u* is the solution at time step *n*.

3.2.2 Validation

To validate the HMI model, the ignition delay times are recorded for hydrogen releases from tanks at various storage pressures and compared against ignition delays times calculated with the LDR model. For both models, expansion is neglected. The results are

presented below in Figure 3.4. For the purpose of this study, a successful ignition event occurs when the OH mass fraction at any given point exceeds 0.001. This particular threshold was found to correlate well with rapid increase in temperature in the numerical experiments. As the figure suggests, the HMI model is able to predict the ignition delay times within the same order of magnitude as the LDR model. The study conducted by Knikker, et al. (2003) also had the same conclusion. In fact, at high storage pressures, the results are almost identical. At lower pressures there is a slight deviation, suggesting that diffusive mixing plays a more important at lower storage pressure limits. However, for the purpose of this study, the results are considered to be in good agreement and therefore the use of the HMI model as an approximation for this study is justified.

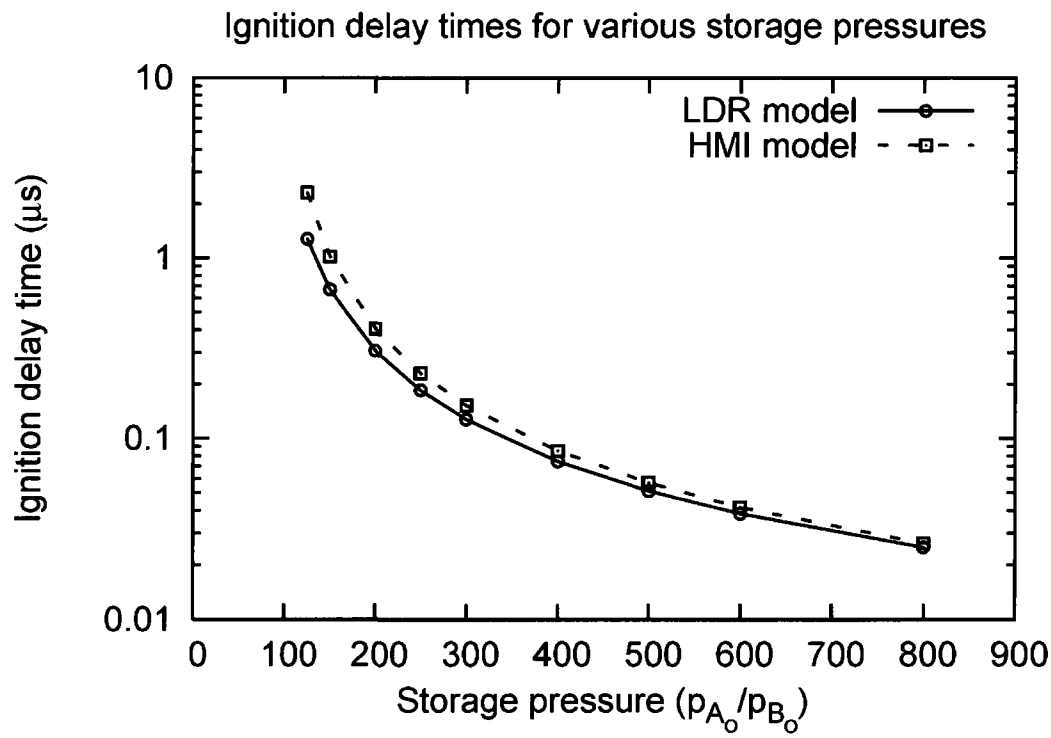

Figure 3.4: Ignition delay times for various storage pressures for both models.

3.3 Computer Program and Algorithm (Both Models)

The algorithm for the main solver of both models is relatively simple. Both models are designed such that they share the same source code with the exception of a few functions. A flow chart is presented in Appendix B to show the basic operation of the program and how it incorporates the external libraries (Goodwin 2009; Hindmarsh, et al. 2005). The program is written in C++ and implements object oriented programming principles (Prata 2005). At the start of the program the user is asked to enter the storage pressure ratio, $\frac{p_{Ao}}{p_{Bo}}$, and the radius of the hole through which hydrogen escapes, r. At each loop the operator splitting steps, described earlier in the chapter, are executed and the results are output at each time step to a file. At the end of the simulation, the program outputs whether or not ignition has occurred. Finally, an external configuration file is required which contains information regarding the resolution, number of grid points, number of loops to execute for the simulation, and the time step size or CFL number.

Chapter 4

Numerical Experiments

A number of numerical experiments are conducted for high pressure hydrogen releases directly into atmosphere for various storage pressures, $\frac{p_{Ao}}{p_{Bo}}$, in order to determine the critical hole size, at which ignition is quenched. These simulations are done using both models (LDR and HMI models), detailed in Chapter 2, for a wide range of storage pressures that are typical for hydrogen storage (Vieira, et al. 2007). First, we look at the critical point of ignition for one particular storage pressure in order to examine how the hole size controls the ignition process. This analysis is first done using the LDR model which allows us to see how the diffusive effects contribute to the ignition phenomena. Next, we will study the critical point of ignition using the simplified HMI model in order to examine the competition between chemical reactions and cooling due to expansion in detail. Finally, the two models are compared against experimental data, which is available for hydrogen releases into atmosphere through tubes of varying length (Golub, et al. 2008; Mogi, et al. 2008). A resolution study for the numerical experiments can be found in Chapter 3.

4.1 Release Simulations for the LDR Model

4.1.1 Release process without expansion

Figure 4.1 shows the temperature profile as well as mass fraction profiles for N_2, H_2, O_2, H_2O, H, O, OH, HO_2, and H_2O_2, respectively, for the release process without expansion. The particular experiment was conducted for an initial storage pressure of $\frac{p_{Ao}}{p_{Bo}} = 300$. When no expansion is prescribed, representative of large hole sizes, ignition is observed. In Figure 4.1a, the initial temperature profile resembles the initial condition sketched in Figure 2.11. The gas on the left of the discontinuity is the hot air and the gas on the right is the cold hydrogen. At early times, the temperature profile is stretched such that the gas to the right of the initial discontinuity sees an increase in temperature and the gas to the left is cooled slightly. This is due to the diffusion of heat from the hot air to the cold hydrogen. Eventually a 'hump' is observed on the hot air side in the figure, which indicates that ignition has occurred. In this particular case ignition occurs after $0.13\mu s$, $6.5\mu m$ from the initial interface between the two gases. Also, the size of the mixing layer at the time of ignition is approximately $10\mu m$. The diffusive mixing process, prior to ignition, can clearly be seen in the profiles of N_2, H_2, and for early times of O_2, in Figure 4.1b, c, and d, respectively. As the two gases mix, H_2 and O_2 species are consumed by chemical reactions. The consumption of O_2 is clearly seen for later times in Figure 4.1d. From Figure 4.1e it is clear that H_2O is eventually produced as the result of the reaction process.

According to the reaction mechanism, described in Section 2.4.6, H_2 and O_2 do not react directly to produce H_2O. Instead, the reaction process is a multiple step process involving chain initiation reactions, chain propagating/carrying reactions, chain branching

reactions, and chain termination reactions (Browne 2004; Law 2006). To initiate the reaction process, the H_2 and O_2 molecules dissociate into H and O radicals through collisions with other molecules. Accordingly, the production of H and O is observed at the ignition site in Figure 4.1f and g, respectively. These radicals then react with other molecules in a series of chain branching and chain propagating reactions to form OH at the ignition site, shown in Figure 4.1h, and to a lesser extent, HO_2 and H_2O_2, shown in Figure 4.1i and j, respectively. In chain branching reactions, more radicals are produced than they are consumed whilst an equal number of radicals are produced and consumed in chain carrying reactions (Law 2006). Finally, H_2O is formed through chain termination reactions where the radicals combine to form stable molecules once the reactants are all exhausted at the ignition site. It should be noted that although these reactions are not noticeable prior to ignition, it does not mean they are not occurring. Since the chemical reactions have a dependency on temperature, the increased temperature at the ignition site leads to an increase in production rates, and thus quicker and more pronounced chemical reactions. Prior to ignition, the production rates are much slower although still present. This becomes more evident in Section 4.2 when the rate of change of energy due to chemical reactions for a fluid particle is tracked as a function of time using the HMI model.

Finally, it is interesting to see from the HO_2 and H_2O_2 profiles, in Figure 4.1i and j, respectively, that there are two thin *reaction sheets* formed, each travelling in opposite directions. These reactions sheets are flames propagating away from the ignition site. Furthermore, from Figure 4.1d, a pocket of unburned fuel and oxidizer remains near the original interface. This region can be seen identified by the 'hump', or increased amounts of O_2 near the interface. The presence of OH in this region also suggests that the mixture is

burning at this location. This burning region, in combination with the two reaction sheets travelling away from the ignition site, is characteristic of the triple flame structure (Domingo and Vervisch 1996; Kioni, et al. 1993; Knikker, et al. 2003).

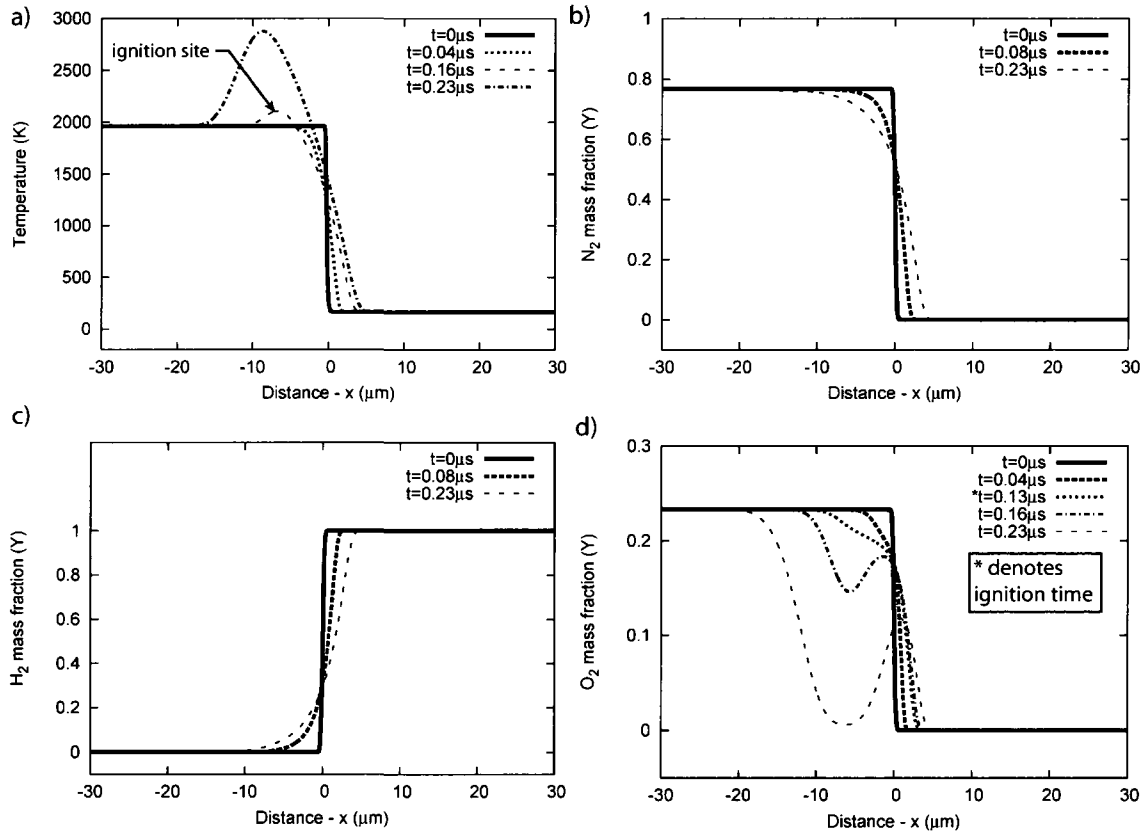

Figure 4.1: Temperature and species mass fraction profiles for the release process without expansion for a storage pressure of $\frac{p_{Ao}}{p_{Bo}} = 300$. In the figure, profiles are provided for a) temperature, b) N2 mass fractions, c) H2 mass fractions, and d) O2 mass fractions. For H2O, H, O, OH, HO2, and H2O2 mass fractions Figure 4.1 is continued on the next page.

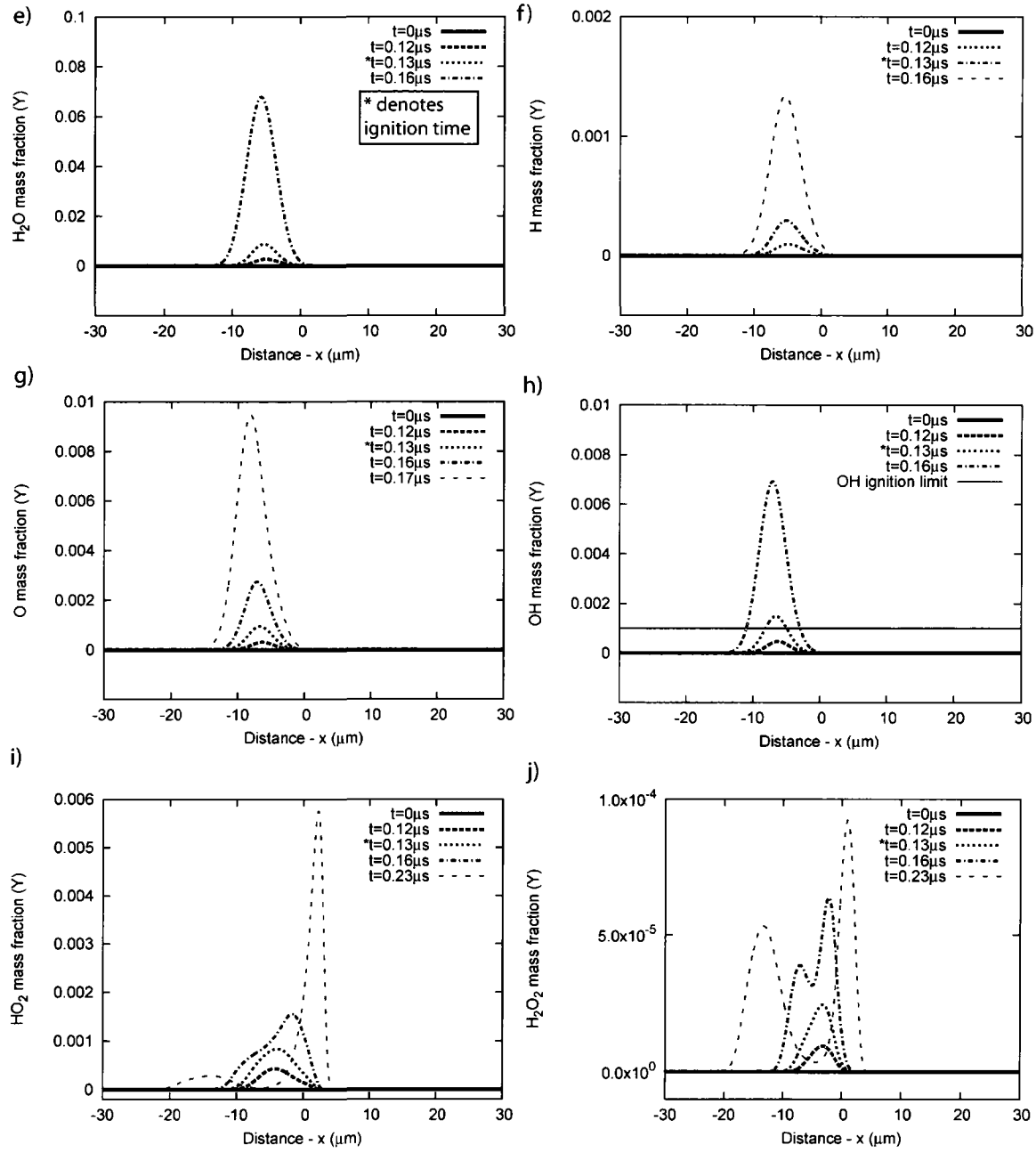

Figure 4.1 (continued...): Mass fraction profiles for the release process without expansion for a storage pressure of $\frac{p_{Ao}}{p_{Bo}} = 300$. In the figure, profiles are provided for e) H2O mass fractions, f) H mass fractions, g) O mass fractions, h) OH mass fractions, i) HO2 mass fractions, and j) H2O2 mass fractions. For temperature, N2, H2, and O2 profiles see Figure 4.1 on the previous page.

4.1.2 Super-Critical Case

The super-critical ignition regime corresponds to successful ignition of the mixing layer despite the cooling effect due to expansion. In this case, the expansion is sufficiently weak, such that ignition is possible. Figure 4.2 shows the temperature profile as well as mass fraction profiles for H_2, O_2, N_2, H_2O, OH, H, O, HO_2, and H_2O_2, respectively, for a typical example of a super-critical case where the storage pressure and hole radius are $\frac{p_{Ao}}{p_{Bo}} = 300$ and r=0.29mm, respectively. In the figure, it is clear that the gas occupies more space as it expands. The temperature drops initially as the gas expands. At some point, however, ignition occurs represented by the appearance of a 'hump' in the temperature profile in Figure 4.2a on the hot air side near the initial interface between the two gases. The heat that is released, as a result of ignition, in this case is sufficiently strong enough to raise temperature of the gas locally. The diffusion and reaction process itself is similar to the case where no expansion is prescribed. In this case, however, the ignition delay is longer, suggesting that the chemical reactions are retarded by the fact that energy is removed during the expansion process. The location of ignition is also further away from the initial interface, owing to the fact that hydrogen has a longer time to diffuse into the air and also owing to the fact that the gas is expanding and occupying more space ahead of the ignition site. Furthermore, the size of the mixing layer at the time of ignition is larger than the previous case. In this case ignition occurs after $0.44\mu s$, $27.5\mu m$ from the initial interface between the two gases. The size of the mixing layer at ignition is approximately $50\mu m$, 5 times greater than the case with no expansion.

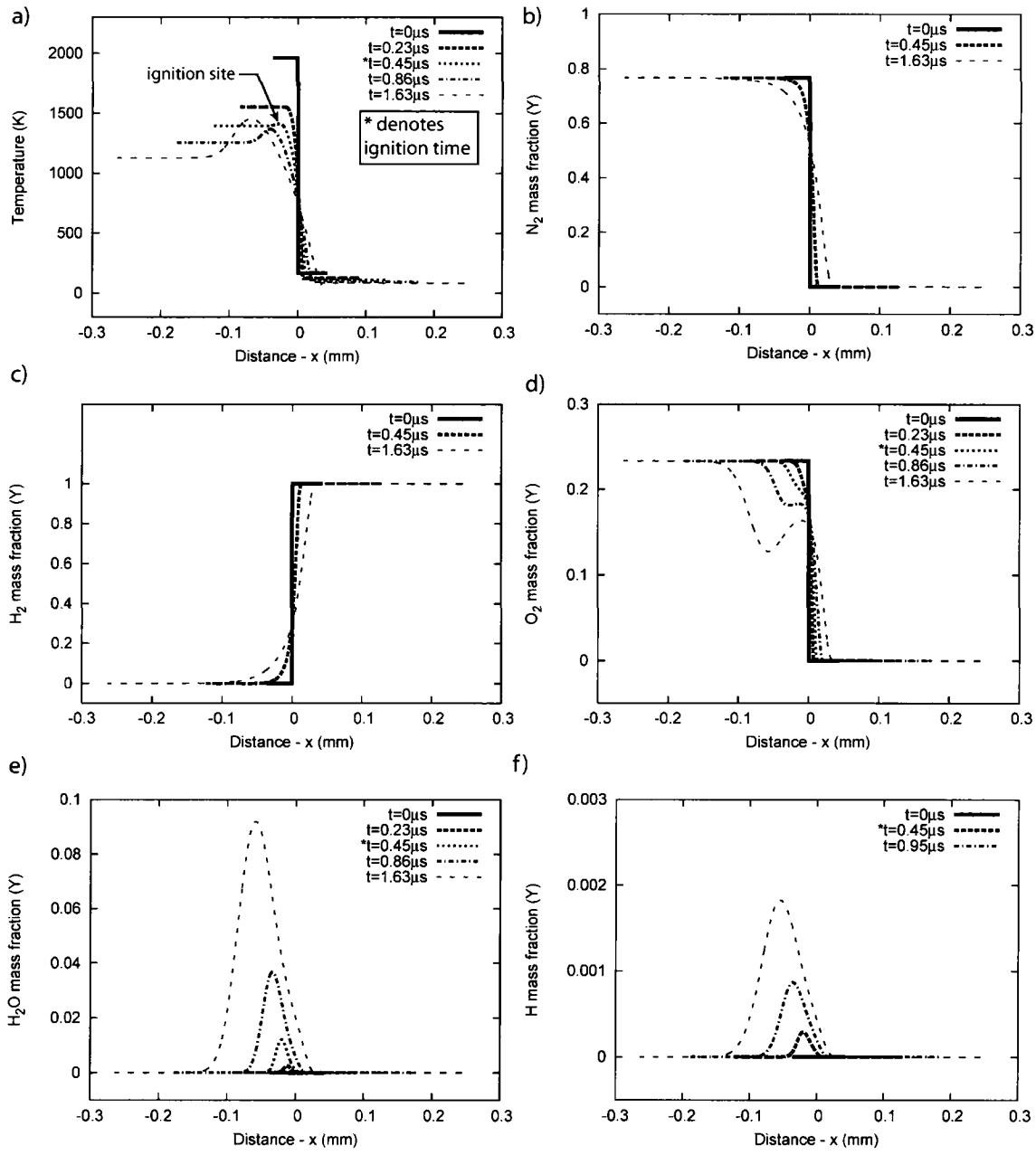

Figure 4.2: Temperature and species mass fraction profiles for the super-critical release process for a storage pressure of $\frac{p_{Ao}}{p_{Bo}} = 300$ and hole radius of r=0.29mm. In the figure, profiles are provided for a) temperature, b) N2 mass fractions, c) H2 mass fractions, d) O2 mass fractions e) H2O mass fractions, and f) H mass fractions. For O, OH, HO2, and H2O2 mass fractions Figure 4.1 is continued on the next page.

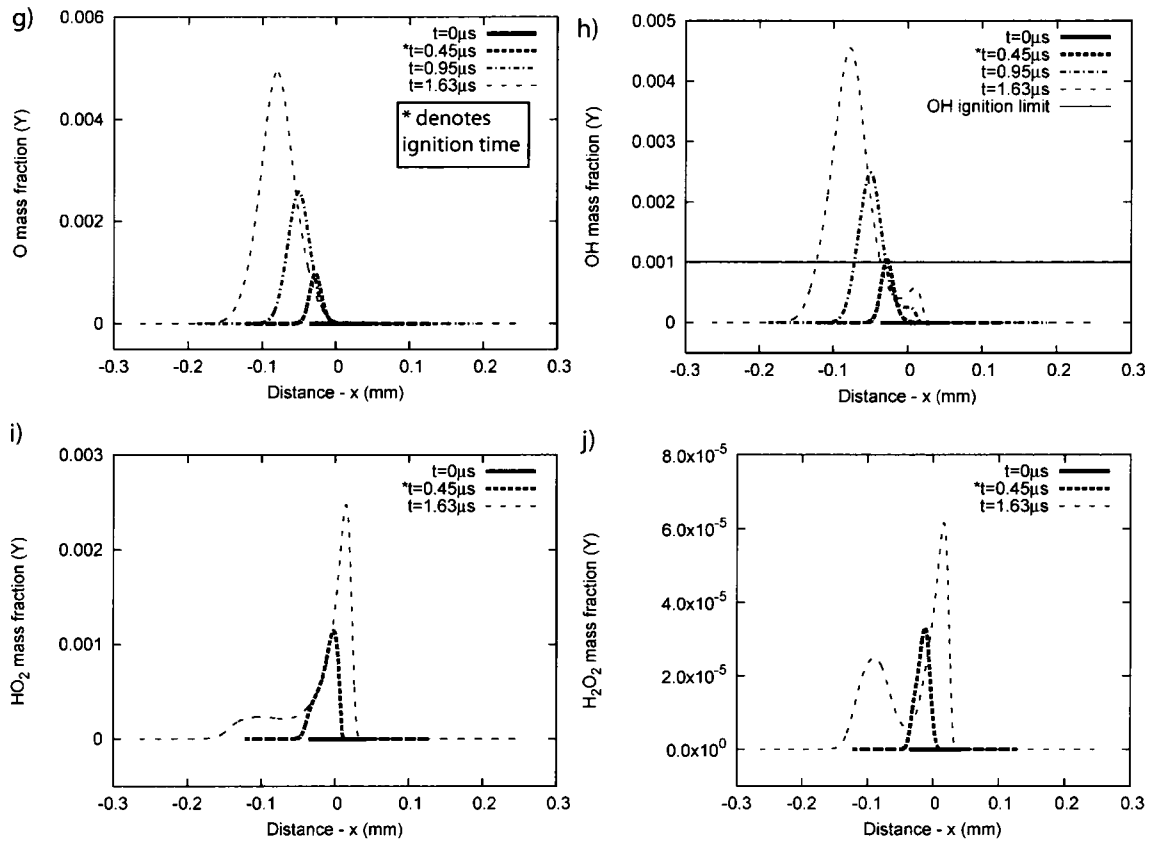

Figure 4.2 (continued...): Mass fraction profiles for the super-critical release process for a storage pressure of $\frac{p_{Ao}}{p_{Bo}} = 300$ and hole radius of r=0.29mm. In the figure, profiles are provided for g) O mass fractions, h) OH mass fractions, i) HO2 mass fractions, and j) H2O2 mass fractions. For temperature, H2, O2, N2, H2O, and H profiles see Figure 4.2 on the previous page.

4.1.3 Critical Case

In this particular case, the hole size is reduced to the point where ignition is on the verge of becoming quenched. The simulation is conducted with an initial storage pressure of $\frac{p_{Ao}}{p_{Bo}} = 300$ and a hole radius of r=0.27mm. Figure 4.3 shows the temperature profile as well as mass fraction profiles for H_2, O_2, N_2, H_2O, OH, H, O, HO_2, and H_2O_2, respectively, for the critical case. In Figure 4.3a, the temperature profile is similar to that of the super-critical case, with the characteristic 'hump' associated with ignition. In this case, however, the local

temperature at the ignition site is continually decreasing, despite the heat released as result of the ignition. This suggests that there is a strong competition between the energy addition due to chemical reactions and the energy removal due to expansion at this critical point.

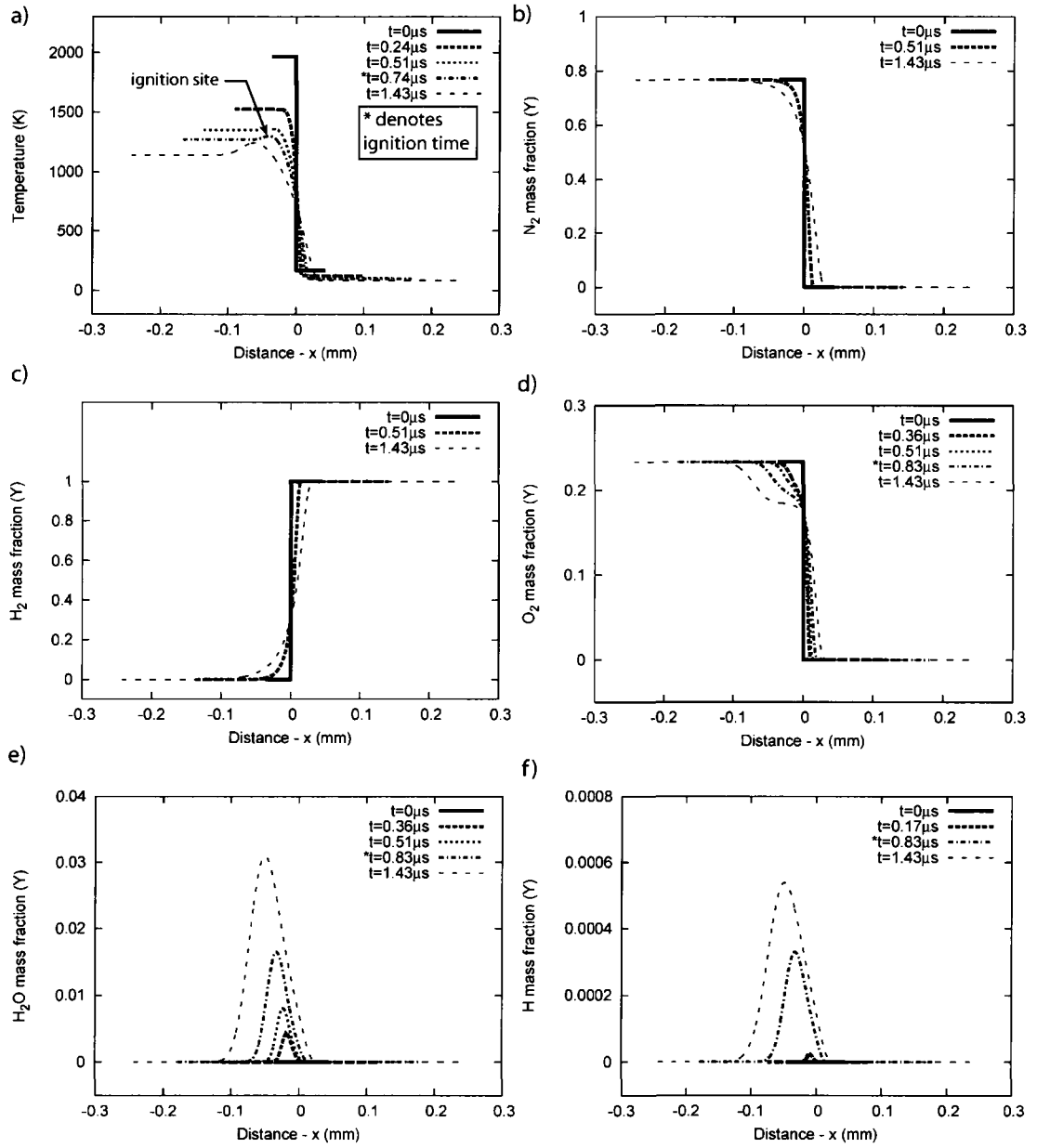

Figure 4.3: Temperature and species mass fraction profiles for the critical release process for a storage pressure of $\frac{p_{Ao}}{p_{Bo}} = 300$ and hole radius of r=0.27mm. In the figure, profiles are provided for a) temperature, b) N2 mass fractions, c) H2 mass fractions, d) O2 mass fractions, e) H2O mass fractions, and f) H mass fractions. For O, OH, HO2, and H2O2 mass fractions Figure 4.3 is continued on the next page.

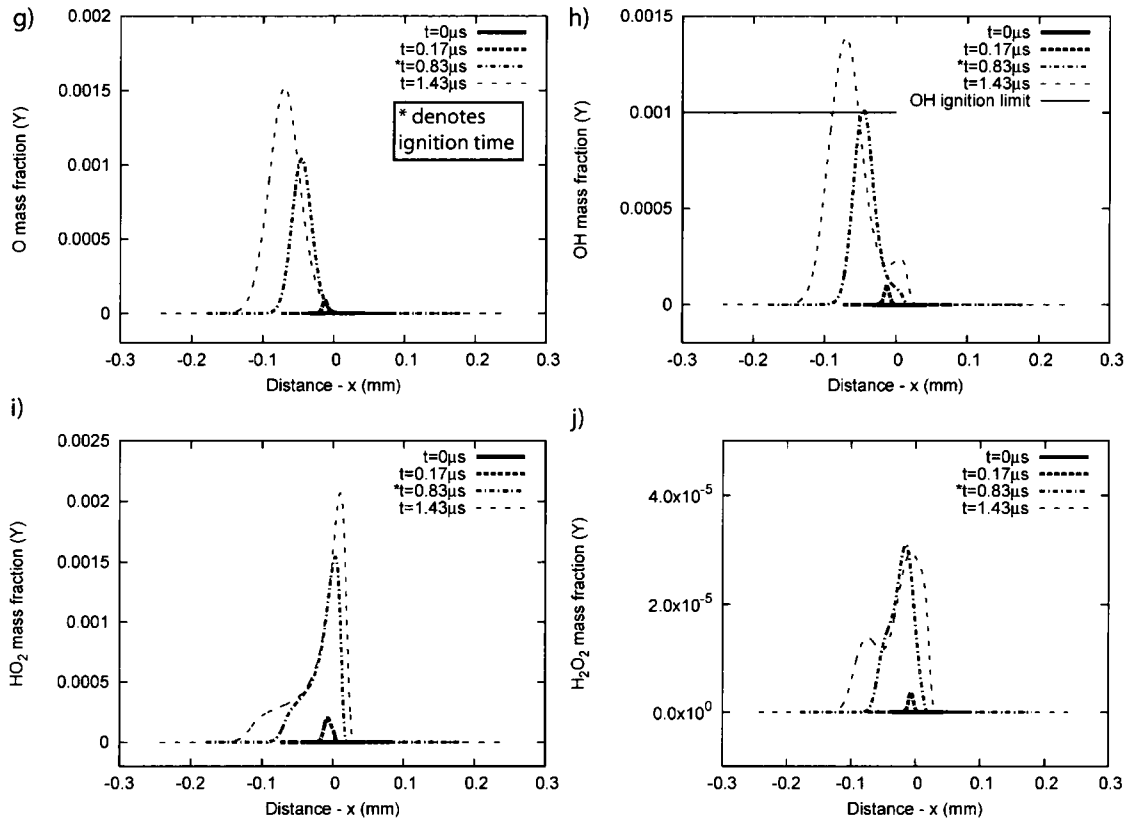

Figure 4.3 (continued...): Mass fraction profiles for the critical release process for a storage pressure of $\frac{p_{Ao}}{p_{Bo}} = 300$ and hole radius of r=0.27mm. In the figure, profiles are provided for g) O mass fractions, h) OH mass fractions, i) HO2 mass fractions, and j) H2O2 mass fractions. For temperature, H2, O2, N2, H2O, and OH profiles see Figure 4.3 on the previous page.

Again, the diffusive mixing and reaction process is similar to the previous two cases, however much slower. The ignition delay in this case is $0.82\mu s$, $46.1\mu m$ from the initial interface between the two gases. The size of the mixing layer at the time of ignition in this case is approximately $100\mu m$. The ignition delay, location of ignition, and size of the mixing layer at ignition are all increased approximately by a factor of 2 compared to the

super-critical case, or a factor of 10 compared to the case without expansion. Furthermore, ignition at the critical point is very sensitive to the smallest changes in hole radius. For smaller hole sizes, the ignition process is quenched altogether.

4.1.4 Sub-Critical Case

With further reduction of the hole size to r=0.20mm, at an initial storage pressure of $\frac{p_{Ao}}{p_{Bo}} = 300$, the reaction is effectively quenched. In this case, the temperature profile and various species mass fraction profiles are shown in Figure 4.4. From Figure 4.4a, it is clear that the reaction is quenched since no increase in temperature is observed. In Figure 4.4b, c, and d, the diffusive mixing of N_2, H_2, and O_2 is observed although in Figure 4.4e only trace amounts of H_2O are produced. In Figure 4.4h, the OH mass fractions peak at approximately $1\mu s$. It should be noted that the OH mass fraction at this point is well below the ignition criteria. Furthermore, at this point, the chemical reactions become inhibited by the expansion and the maximum amount of OH is then reduced with time. Finally, only trace amounts of the radicals H, O, HO_2 and H_2O_2 are observed.

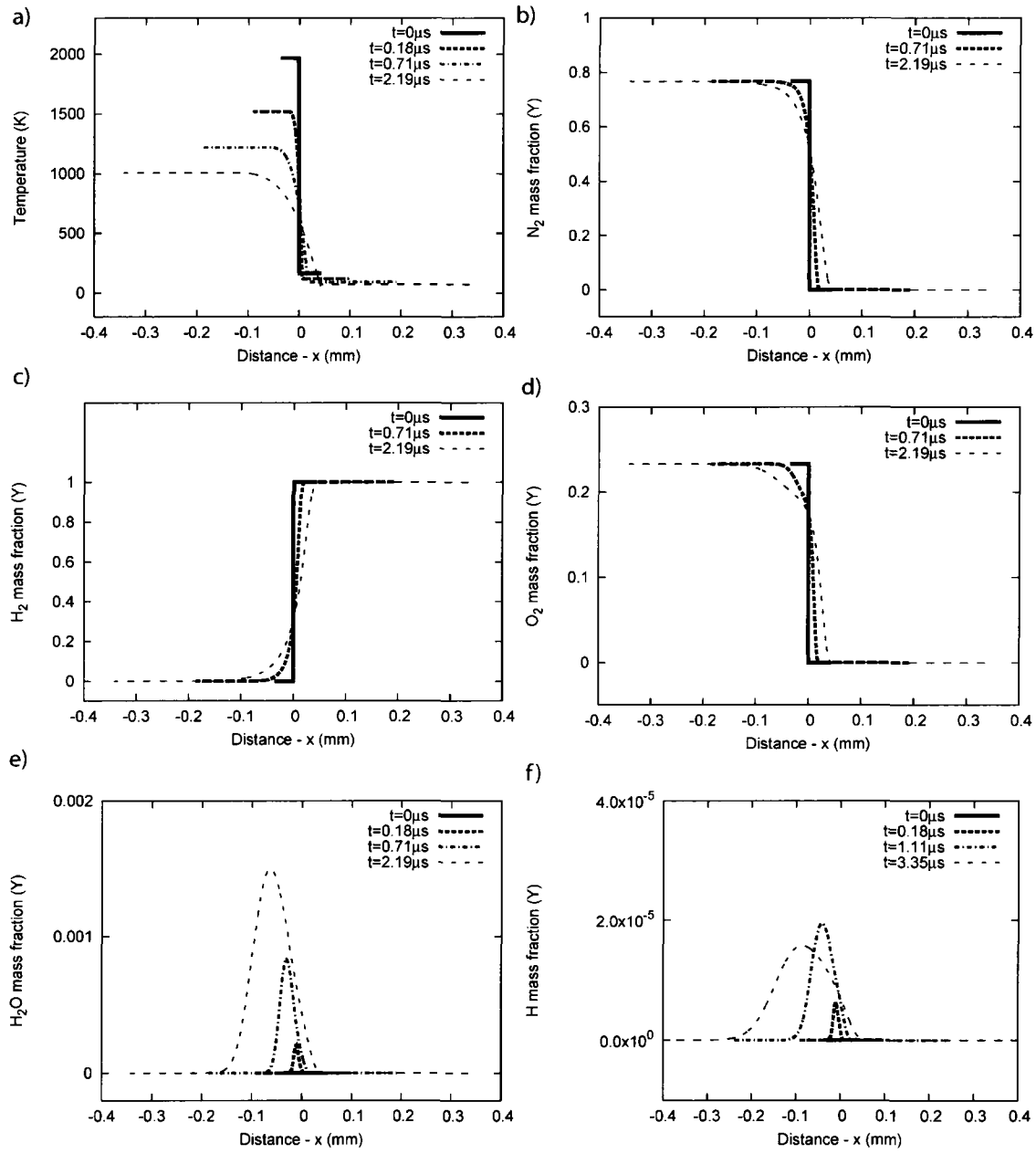

Figure 4.4: Temperature and species mass fraction profiles for the sub-critical release process for a storage pressure of $\frac{p_{Ao}}{p_{Bo}} = 300$ and hole radius of r=0.20mm. In the figure, profiles are provided for a) temperature, b) N2 mass fractions, c) H2 mass fractions, d) O2 mass fractions, e) H2O mass fractions, and f) H mass fractions. For O, OH, HO2, and H2O2 mass fractions Figure 4.1 is continued on the next page.

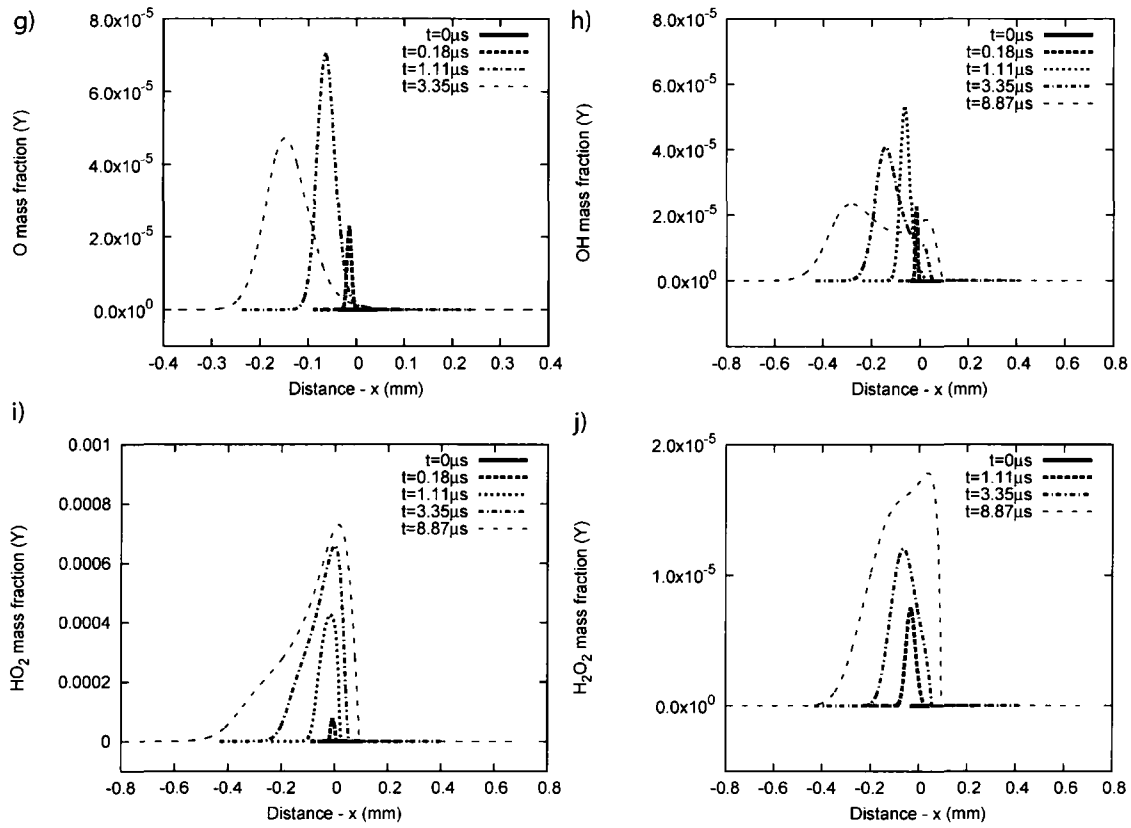

Figure 4.4 (continued...): Mass fraction profiles for the sub-critical release process for a storage pressure of $\frac{p_{Ao}}{p_{Bo}} = 300$ and hole radius of r=0.20mm. In the figure, profiles are provided for g) O mass fractions, h) OH mass fractions, i) HO2 mass fractions, and j) H2O2 mass fractions. For temperature, H2, O2, N2, H2O, and OH profiles see Figure 4.4 on the previous page.

4.1.5 Ignition Limits for Various Storage Pressures

In the above simulations, the critical ignition limit was found for one particular initial storage pressure, $\frac{p_{Ao}}{p_{Bo}} = 300$. For this particular storage pressure, the critical hole radius was found to be 0.265 ±0.005mm. For larger hole sizes ignition was observed and for smaller hole sizes ignition was quenched. The experiment was repeated over a wide range of initial storage pressures, 100 to 1000 atmospheres, in order to study how the ignition limit, or critical hole size, changes as a function of storage pressure. The resulting curve is shown below in Figure 4.5. It is clear from the figure that higher storage pressures of hydrogen

require smaller holes for the gas to escape through in order for ignition to be quenched. If the storage pressure and hole size corresponds to a location that is to the lower left of the curve, ignition is quenched. If the storage pressure and hole size lies to the upper right of the curve, ignition is observed.

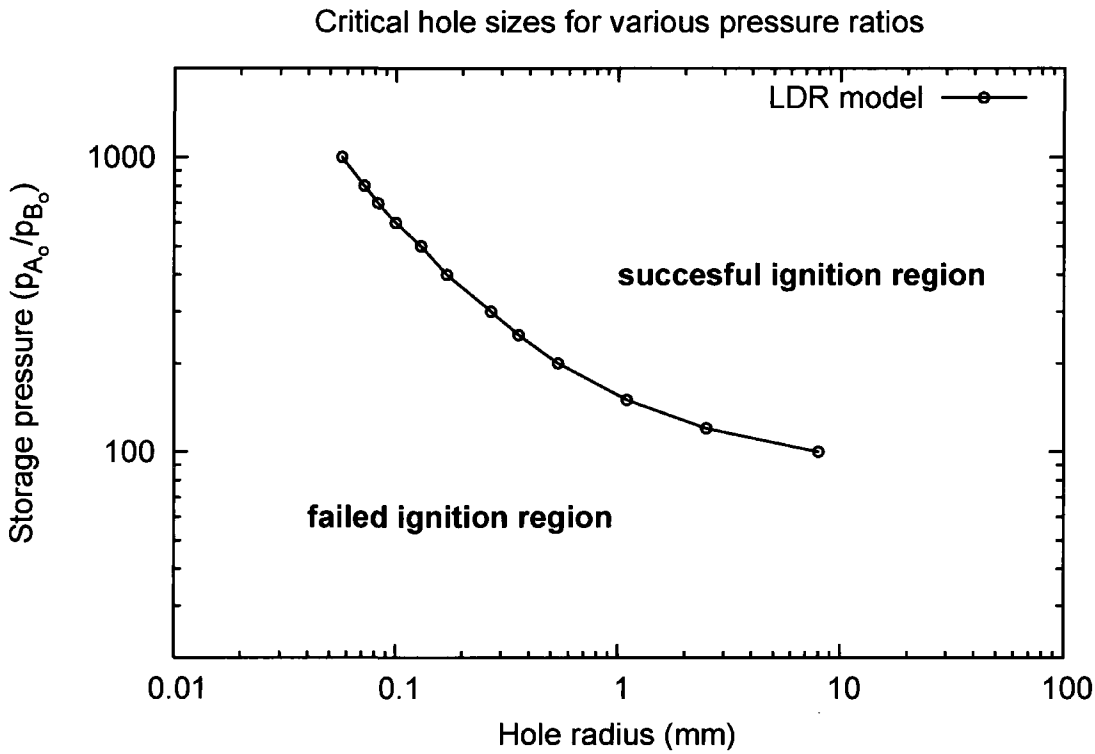

Figure 4.5: Critical hole sizes to quench ignition at various storage pressure ratios, $\frac{p_{Ao}}{p_{Bo}}$ (LDR model).

4.1.6 Problems and Difficulties with the LDR Model

Once the pressure of the mixing layer reaches the ambient atmospheric pressure, p_{B_o}, it is assumed the expansion process ceases since the jet would become over expanded if expansion is allowed to continue beyond this point. Unfortunately, due to the computer power available at the time of writing, it is very costly to simulate the ignition process beyond the expansion phase using the LDR model. As a result, the LDR simulations are

conducted within the expansion phase only and ignition in the far field is not considered. It should be noted, however, that far field ignition is studied using the HMI method in Section 4.3. Further difficulties arise, for the LDR model, when the local temperature of the mixture drops below 73K during the expansion process. Below 73K, an infinite error is encountered during the calculation of the net production rate of species i, ω_i. Specifically, the problem arises in equation 2.70 as $k_{c_n} \to 0$. According to equation 2.71, $k_{c_n} \neq 0$ for all temperatures. However, computers have a finite domain for which a number can be stored. If the number is smaller than the minimum allowed value, digitally, it will be recognized as a zero by the computer. For example, on typical personal computers, double data types have a maximum and minimum exponent range of +308 and -307 (Prata 2005). If a double precision floating point number has an exponent larger or smaller than this allowed range it will consequently be stored as infinite or zero, respectively. Therefore, as $k_{c_n} \to 0$, $k_{r_n} \to \infty$ and ω_i cannot be computed. For the kinetic mechanism developed by Li, et al. (2004), this error occurs when the temperature of the gas drops below 73K. In order to correct the problem, *long double* variables (Prata 2005) should be used in the calculations of the production rates of each chemically reacting specie in order to allow numbers smaller than those allowed by *double* type variables. Long doubles are typically capable of handling exponents in the range of +4932 and –4931 (Prata 2005). This would allow division by very small numbers, thus allowing a realistic production rate to be calculated at temperatures below 73K.

To overcome this problem in this study, ω_i is assumed to be zero when the error is encountered. This assumes that at sufficiently low temperatures, the chemical reactions do not play an important role, locally, while diffusion and expansion are allowed to continue.

4.2 Release Simulations for the HMI Model

The ignition process was also addressed using the *Homogeneous Mixing Ignition* (HMI) Model detailed in Section 2.5. For comparison with the results presented in the previous section, the storage pressure, $\frac{p_{Ao}}{p_{Bo}}$, was fixed at 300 atmospheres and the hole size, r, was varied to find the critical ignition limit. For consistency with the previous numerical experiment, simulations are conducted for the duration of the expansion process only. Temperature and chemical specie mass fraction profiles are presented for four cases in Figure 4.6 and Figure 4.7, respectively. The four cases are 1) the super-critical case (r=1.00mm), 2) the near-critical case (r=0.40mm), 3) the critical case (r=0.32mm), and 4) the sub-critical case (r=0.25mm).

According to the temperature profiles presented in Figure 4.6, for sufficiently large hole sizes, the super-critical case for example, ignition occurs as it would if there were no expansion. Ignition is represented in the figure by a sharp increase in temperature. As the hole size is reduced, the onset of pressure decay occurs sooner causing a cooling effect in the gas. Despite this cooling effect, however, it is still possible for chemical reactions to occur which can lead to ignition. This is observed for the near-critical case. With a further reduction in hole size, a critical point is reached, below which ignition is not observed. The critical radius obtained using the HMI method for this particular storage pressure was found to be 0.315 ±0.005mm. This radius is only slightly larger than the critical hole size obtained with the LDR model, 0.27mm. The ignition process itself is the same as that observed for the LDR model where H_2 and O_2 molecules are consumed, as can be seen in Figure 4.7a and b, forming H and O radicals, whose profiles are shown in Figure 4.7c and d. Through a series of chain branching reactions we see the appearance of OH radicals, shown in Figure 4.7e and

also HO_2 and H_2O_2 in trace amounts, presented in Figure 4.7f and g, respectively. Finally, H_2O, shown in Figure 4.7h, is produced as the product gas. Clearly for the cases that do not achieve ignition, only trace amounts of H_2O are produced. Also, there is no noticeable consumption of O_2 and H_2. Although there are still some chemical reactions that occur for the sub-critical case, as seen by the production of a small amount of radicals in Figure 4.7e, they are not strong enough to contribute to any significant, or noticeable, changes in the temperature or composition of the gas during the expansion process. Furthermore, the critical point at which the ignition occurs is very sensitive to small changes in the hole size. The smallest change in hole size can lead to full blown ignition, or no ignition at all. This reflects the strong competition between chemical reactions and expansion at this point. Finally, it should also be noted that the reaction mechanism developed by Li, et al. (2004) treats N_2 as inert such that the mass fraction of N_2 remains constant throughout the reaction process. For details on the reaction mechanism see Section 2.4.6.

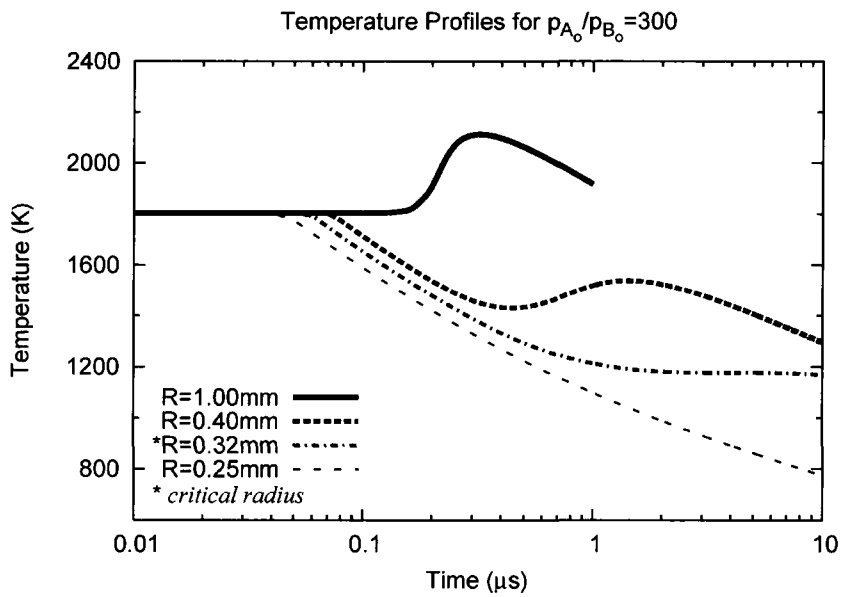

Figure 4.6: Temperature profiles for 4 cases; the super-critical case (r=1.0mm), the near-critical case (r=0.40mm), the critical case (r=0.32mm), and the sub-critical case (r=0.25mm). All simulations are conducted for the HMI model with an initial storage pressure of 300 atm.

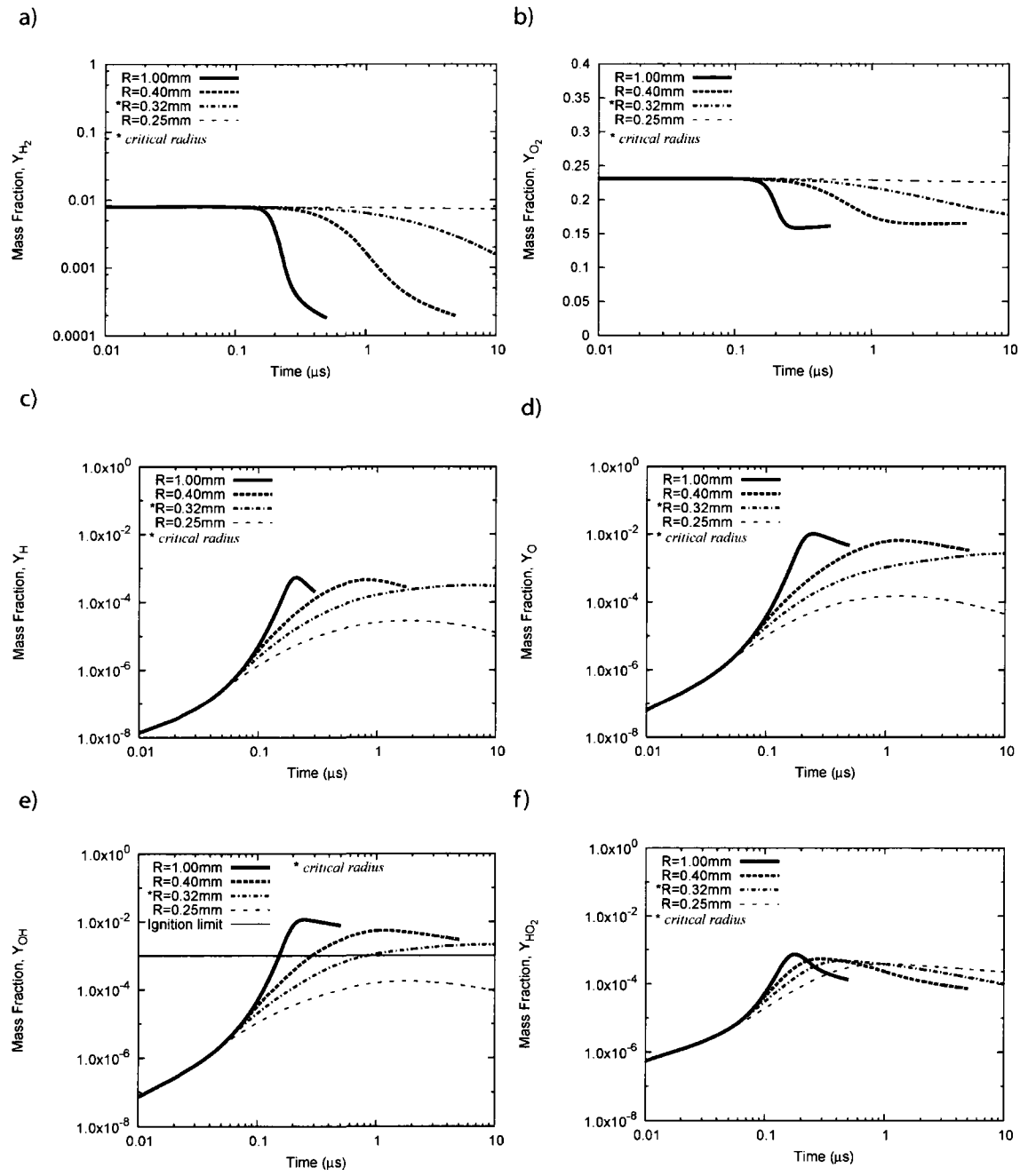

Figure 4.7: Species mass fraction profiles for 4 cases; 1) the super-critical case (r=1.0mm), 2) the near-critical case (r=0.40mm), 3) the critical case (r=0.32mm), and 4) the sub-critical case (r=0.25mm). All simulations are conducted for the HMI model with an initial storage pressure of 300 atm.. In the figure, profiles are provided for a) H2 mass fractions, b) O2 mass fractions, c) H mass fractions, d) O mass fractions, e) OH mass fractions, and f) HO2 mass fractions. For H2O2 and H2O mass fractions, Figure 4.7 is continued on the next page.

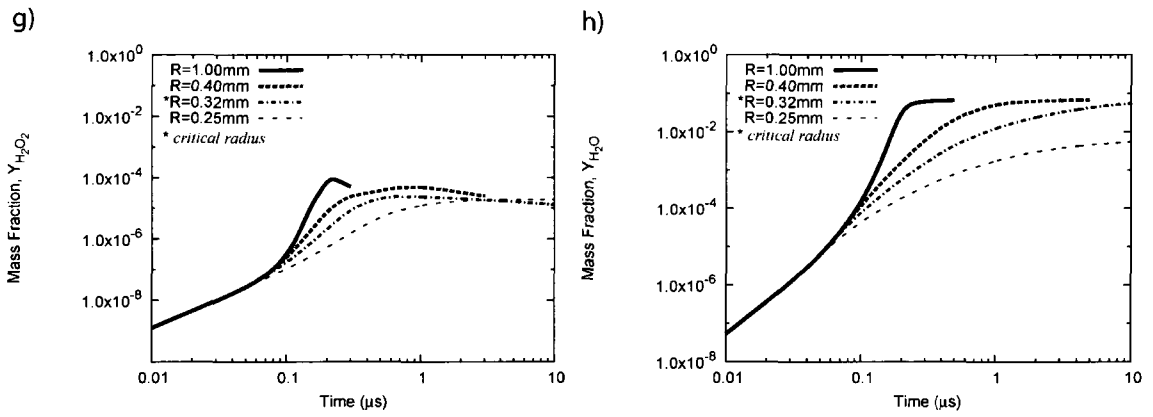

Figure 4.7 (continued...): Mass fraction profiles for the critical release process for a storage pressure of $\frac{p_{Ao}}{p_{Bo}} = 300$ and hole radius of r=0.20mm. In the figure, profiles are provided for g) H2O2 mass fractions and h) H2O mass fractions. For H2, O2, H, O, OH, and HO2 profiles see Figure 4.7 on the previous page.

In order to examine the competition between chemical reactions and expansion in more detail, the rate at which energy changes in the constant mass particle is recorded as a function of time for the four cases; the super-critical case, the near-critical case, the critical, and the sub-critical case. Specifically, the energy record in Figure 4.8 shows the rate at which energy is added to the particle due to the chemical reactions and also the rate at which energy is removed due to expansion. Furthermore, the energy balance between energy addition due to chemical reactions and energy removal due to expansion for the representative fluid particle is shown below in equation 2.73. Also shown in the Figure are the temperature profiles for each case, which correspond to the profiles presented in Figure 4.6. Clearly, for the super-critical case, the rate at which energy is added through chemical reactions is initially greater than the rate at which energy is removed due to expansion. This leads to an early ignition event, represented by a sharp increase in temperature. For the near-critical case, the expansion is initially strong enough to overcome ignition. The result is an initial drop in temperature. However, at some point, the rate at which energy is added to the

particle from the chemical reactions becomes greater than the rate at which energy is removed due to expansion. This leads to a subsequent increase in temperature and ignition is finally observed. For the critical case, the amount of energy added to the particle through chemical reactions becomes equal to the amount of energy that is removed due to expansion. Although there is no significant increase in temperature, the *OH* concentration exceeds the ignition threshold of 0.001, as discussed in Section 3.2.2. Chemical reactions take place and the rate at which temperature decreases is greatly reduced. Finally, for the sub-critical case, the rate of energy removal due to expansion dominates. In this case, the chemical reactions are quenched altogether and thus ignition does not occur.

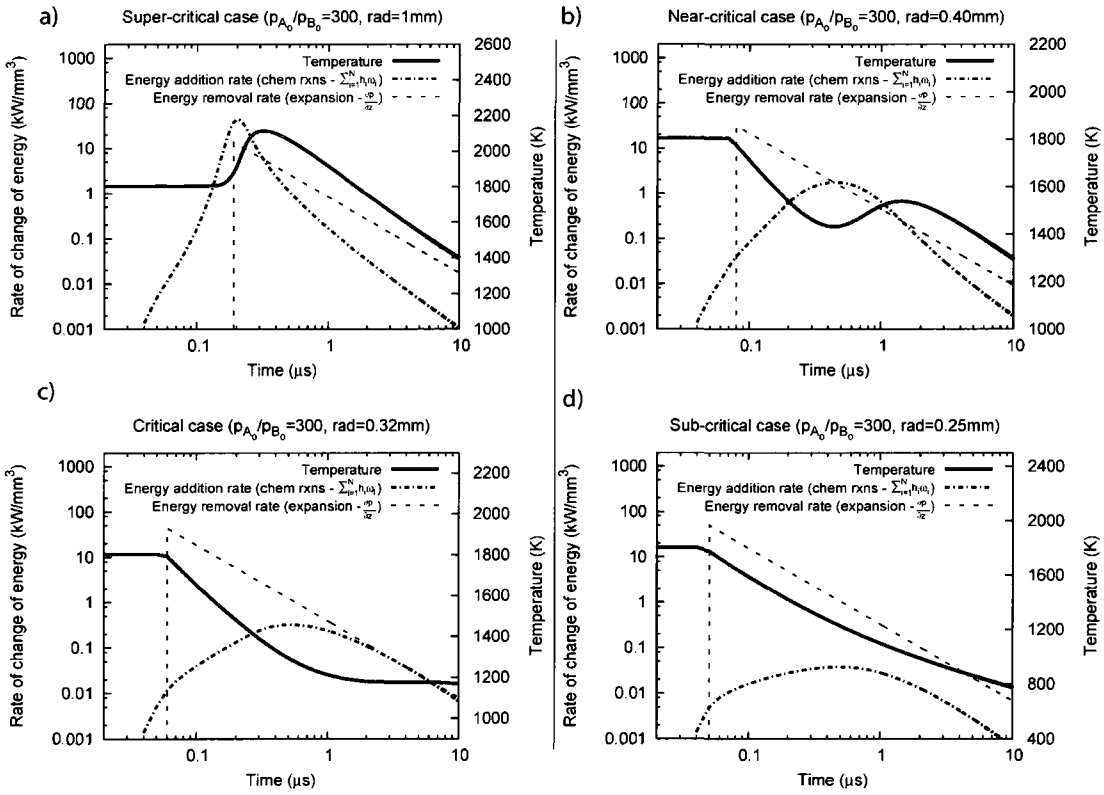

Figure 4.8: Energy Record for 4 cases; a) the super-critical case, b) the near-critical case, c) the critical case, and d) the sub-critical case. All simulations are conducted for the HMI model with an initial storage pressure of 300 atm.

$$\rho c_p \frac{\partial T}{\partial z} = \frac{\partial p}{\partial z} - \sum_{i=1}^{N} h_i \omega_i \qquad 2.73$$

The competition between heating and cooling, present in equation 2.73, is analogous to the competition observed for unsteady detonations. For discussion purpose, a detonation wave is a shock wave that travels in a combustible medium that is coupled to a trailing exothermic reaction zone with a short induction period (Law 2006; Thompson 1988). Lundstrom and Oppenheim (1969) were able to show, experimentally, that when a detonation front is unsteady, the expansion behind the decaying front leads to the decoupling of the shock wave and reaction zone. Furthermore, a numerical study by Eckett, Quirk, and Shepherd (2000) demonstrates that there is a direct competition, or dominant balance, between energy removal due to unsteadiness (i.e. change in velocity and pressure with time) and energy addition due to chemical reactions. Their calculations confirm that if the unsteadiness in a detonation is strong enough, the detonation wave becomes quenched. This is synonymous with the energy balance in this particular study, where the unsteady term is simply the change in pressure with time observed at the mixing layer.

4.3 Ignition in the Far Field (Post Expansion Phase)

Due to computer limitations, simulations for the LDR model are only conducted until the pressure decays to atmospheric pressure. Consequently, the same is done with the HMI model in order to produce a proper comparison between the two models. In reality, however, it is possible for ignition to occur in the far field once the gas has already reached atmospheric pressure and expansion no longer occurs. Since energy is no longer removed at this point, if the chemical reactions are strong enough it is possible for ignition to occur. To

demonstrate this, simulations were conducted beyond the expansion phase for the storage pressure of $\frac{p_{Ao}}{p_{Bo}} = 300$ using the HMI model. When the pressure of the particle reached atmospheric pressure, the expansion term in equation 2.73 is neglected, preventing the pressure from dropping below atmospheric. The simulation was allowed to run for a time that was several orders of magnitude longer than the time at which atmospheric pressure was reached. The temperature and OH mass fraction profiles for the simulations are presented in Figure 4.9.

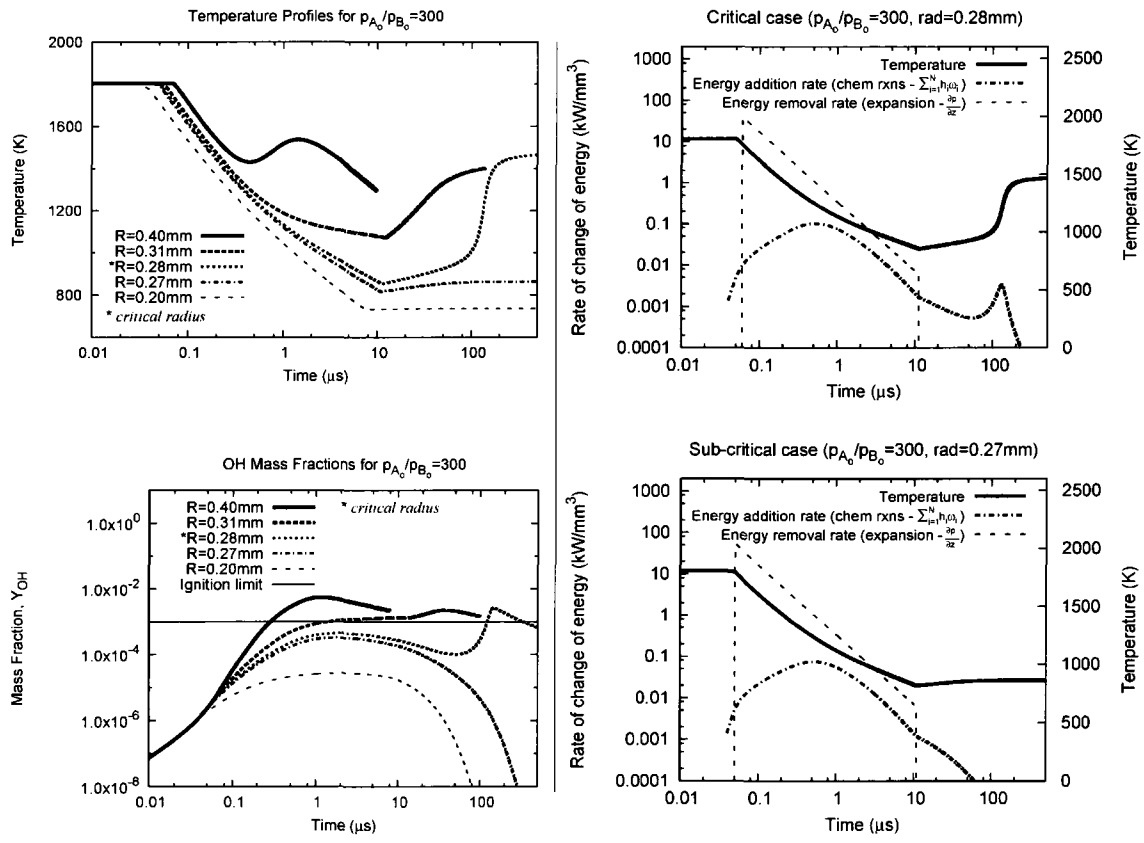

Figure 4.9: Temperature, OH, and Energy Record profiles beyond the expansion phase.

Clearly, when considering ignition in the far field, once the pressure has reached atmospheric, the critical radius for quenching ignition is reduced. For this particular storage pressure, the critical radius for observing ignition in the far field is 0.275 ±0.005mm. This is a slight difference from the 0.315 ±0.005mm critical limit observed during the expansion phase. Again, energy records, also shown in Figure 4.9, are provided for the critical case (0.28mm hole radius) and for the sub-critical case (0.27mm hole radius). In both cases, the rate at which energy is removed due to expansion dominates. However, once the expansion phase is complete, the energy addition due to chemical reactions in the critical case is enough to cause ignition to occur after some time passes. When the hole size is reduced, the chemical reactions are still quenched in the post expansion phase and ignition is not observed. It should be noted, however, that while constant pressure is assumed once the gas has reached atmospheric pressure, in reality it is likely that the jet would be subject to acoustic instabilities as the pressure nears the ambient pressure (Radulescu and Law 2007). Furthermore, turbulent mixing in the far field may also affect the ignition process, and is not considered in this model.

4.4 Ignition Limits in the Expansion Phase

Various jets with pressure ratios ranging from $\frac{p_{Ao}}{p_{Bo}} = 75$ to 1000 were simulated with varying hole sizes in order to determine the critical point, or hole size, at which ignition is quenched. The critical hole size for which the onset of ignition occurs for various storage pressures is shown below in Figure 4.10. The critical hole size is shown for both the *Lagrangian reaction-diffusion model* (LDR model) and the *homogeneous mixing ignition*

model (HMI model). For consistency, both simulations are run for the duration of the expansion process only. The critical hole sizes were determined based on the ignition criteria of *OH* mass fractions described previously. As mentioned previously, higher storage pressures of hydrogen require smaller holes for the gas to escape through in order for ignition to be quenched.

For comparison with experiment, Golub, et al. (2008) had conducted lab experiments for hole diameters of 5mm and for storage pressures below 123atm. Their findings show that ignition does not occur at this particular storage pressure or below. This particular point is shown in Figure 4.10 and proves to be in good agreement with the numerical models, although further experiments are required to find the actual ignition limit.

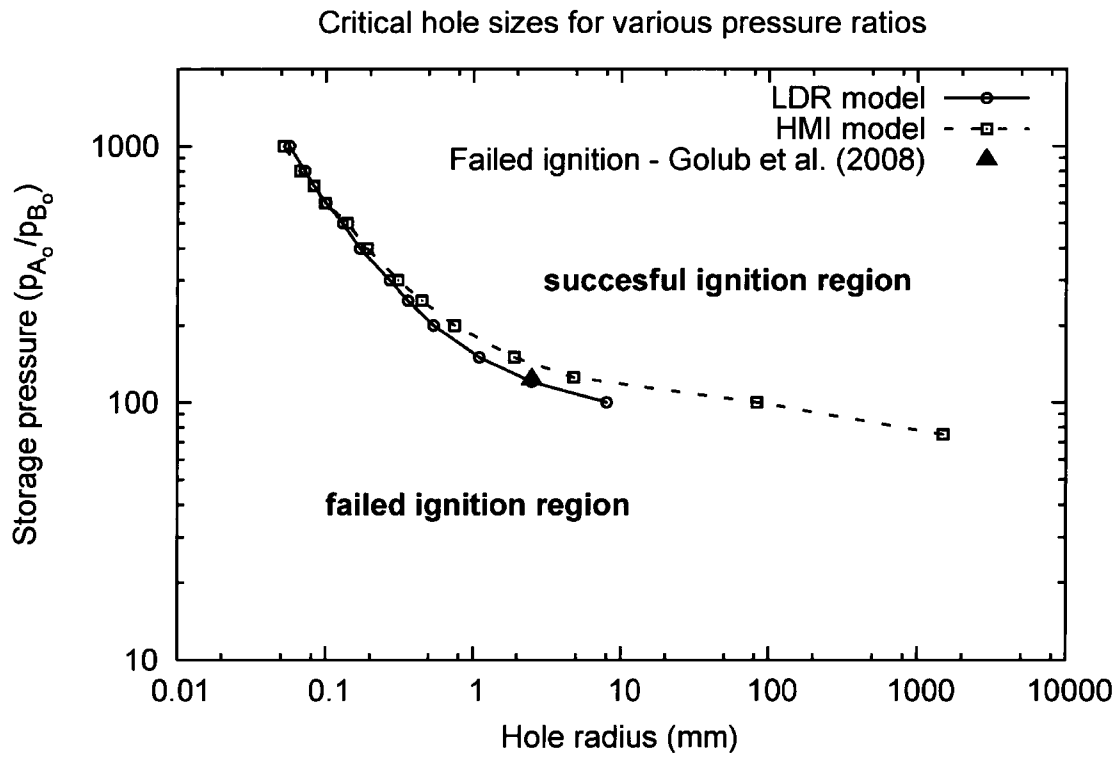

Figure 4.10: Critical hole sizes to quench ignition at various storage pressure ratios, $\frac{p_{Ao}}{p_{Bo}}$ (both models). These limits do not take into account ignition in the far field.

One final observation that is made from Figure 4.10 is that there is a significant change in the slopes of both curves around a storage pressure of $\frac{p_{Ao}}{p_{Bo}} = 150$. Below this storage pressure, the ignition is severely inhibited due to the well-known cross-over effect in hydrogen ignition (Law 2006). For a storage pressure of 150 atm, the temperature and pressure at the jet head are 1500 K and 28 atm. At temperatures below this limit and pressures above this limit, the chain branching reactions are inhibited by rapid chain termination reactions. For all practical purposes, ignition becomes very difficult below this critical limit.

4.5 Comparison with Experiments

Critical pressures for ignition of unconfined releases are not available in the literature. Experiments (Golub, et al. 2008: Mogi, et al. 2008) have, however, determined the critical ignition pressure for releases through pipes of various lengths. Both models are adapted to this geometry by lengthening the residence time of the gas at the initial state to account for the increase in residence time before the onset of the quenching expansion wave reaches the jet head. Since the models are inviscid, the mixing layer is assumed to travel at constant velocity and pressure within the tube. The results, shown in Figure 4.11, indicate that for longer pipe lengths, the storage pressure required for ignition to occur decreases.

In general, both models agree quite well with experimental data for shorter tubes (60-100mm length, 5mm radius). However for longer tubes, ignition is observed, experimentally, at lower pressures than predicted by the two numerical models. This

discrepancy may be accounted for by including increased temperatures of the fluid as it slows down in the boundary layer near the pipe wall. To account for boundary layer effects in longer tubes, the HMI model is adapted to simulate a hot spot, or a particle whose velocity is reduced to zero as a result of entering the boundary layer near the pipe wall. Its kinetic energy is transferred to the particle in the form of heat at the beginning of the simulation, through equation 4.1. Also the walls of the pipe are assumed to be adiabatic such that there is negligible heat loss. The temperature recovery is given by

$$\Delta T = \frac{{u_i}^2 - {u_f}^2}{2c_p} \qquad \textbf{4.1}$$

where u_i is the initial velocity of the particle calculated through the shock tube solution and $u_f = 0$. Results indicate that the inclusion of these effects allows spontaneous ignition to occur at lower storage pressures. For longer tube lengths (140-180mm), the modified HMI model with kinetic heat addition agrees quite well with the experimentally observed lower ignition limit.

Although both models were found to capture the ignition phenomena within experimental error, the large scatter between the experiments suggests that more controlled experiments are required. Also, due to high cost of using the LDR model at low storage pressures, the simulations have been conducted at a lower resolution, $\Delta m = 2\text{x}10^{-6}\text{kg/m}^2$ with a domain consisting of 4001 nodes. To have a better prediction for the ignition limit, the numerical models should be modified to take into account realistic boundary layer effects within the tubes and the resolution of the LDR model should be increased in order to fully resolve the diffusion ignition phenomena in the mixing layer.

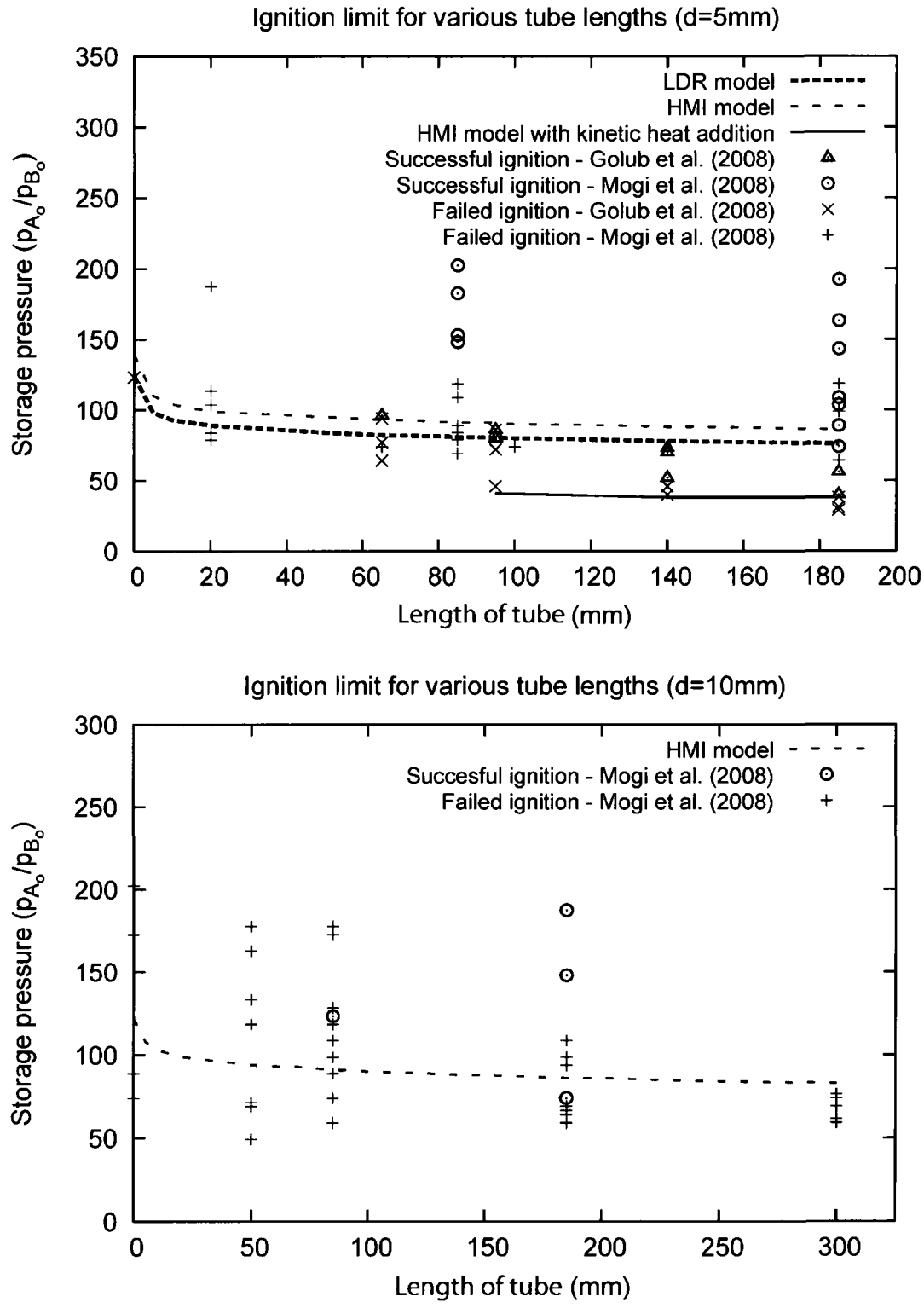

Figure 4.11: Ignition limit for hydrogen released into air through 5mm and 10mm diameter tubes of various lengths.

Chapter 5

Conclusions and Recommendations

The results of the numerical simulations indicate that for every storage pressure, there exists a critical hole size below which ignition is prevented during the hydrogen release process. Close inspection of the results indicate that this limit is due to the competition between the heating provided by the shock wave and the cooling due to expansion. In particular, the hydrogen storage pressure controls the strength of the shock that is observed upon release which in turn controls the temperature and pressure of the gases behind the shock. Also, the size of the opening determines the rate at which the mixing layer at the head of the jet expands, or cools. This cooling effect was found to be more efficient for smaller holes. Smaller holes experienced more rapid depressurization of the jet head, and thus require a higher storage pressure in order for ignition to occur.

The results also indicate that the details of the mixing process do not play a significant role to leading order. The limiting ignition criteria were found to be well approximated by the *Homogeneous Mixing Ignition Model* (HMI model) of Knikker, et al. (2003), which was supplemented by an energy loss term due to expansion. Therefore, turbulent mixing

occurring in reality is not likely to significantly affect the ignition limits derived in the present study.

If more accurate results are desired, simulations should be conducted with the LDR model to determine the ignition limits in the far field, beyond the expansion phase where the pressure of the mixing layer reaches atmospheric. It has been demonstrated with the HMI model that it is possible for ignition to occur in the far field for hole sizes that were quenching the reactions during the expansion phase. If the chemical reactions are strong enough at the end of the expansion phase, it is possible for ignition to occur in the absence of energy removal due to expansion. Some other suggested improvements to the model include implementation of *multi-component* transport properties (Kee, et al. 2000) rather than *mixture-averaged* as well as inclusion of DuFour and Soret effects in the governing equations. These improvements, however, require significantly more computer power than the current LDR model and are currently considered to be too expensive to implement on personal computers. Furthermore, it should be noted that while including multi-component transport properties may affect the ignition limits, it is unlikely that the DuFour Soret effects will have a significant impact. Also, a model should be developed for the inclusion of viscous boundary layer effects during releases into atmosphere through tubes of varying lengths. Finally, the division by zero error in the calculations of the production rates of each chemically reacting specie should be addressed by using *long double* variables instead of *doubles*, as discussed in Section 4.1.5.

In general, comparison of the numerical models with existing experiments also showed very good agreement within experimental error. It should be noted, however, that more controlled experiments should be conducted in order to achieve more accurate and consistent

results. To date, most experiments have been conducted for hydrogen releases into the atmosphere through tubes of varying length. Of the experiments (Golub, et al. 2008; Mogi, et al. 2008), results vary significantly from study to study. Also, very little experimental data is available for releases directly into air in the absence of a tube.

Finally, it should be noted that although ignition is required in order to have a jet flame, such a flame may not necessarily be established. The models used in this study are intended to capture the point of ignition only. If one desires to model the establishment of a jet flame, turbulent mixing becomes much more important. Thus, the models in this study provide a conservative estimate for the explosive limits of accidental hydrogen releases. For practical hole sizes, without extension pipes, spontaneous ignition is not expected below storage pressures of approximately 100 to 150 atm. This has significance in terms of generating the appropriate codes and standards regarding the storage and handling of hydrogen, especially since planned storage pressures for hydrogen as a fuel are above this limit (Vieira, et al. 2007).

Bibliography

Al-Khateeb, A. N., J. M. Powers, and S. Paolucci. "Verified Computations of Laminar Premixed Flames." *45th AIAA Aerospace Science Meeting and Exhibit.* Reno, Nevada, 2007.

Anderson, J. D. *Computational Fluid Dynamics: The Basics with Applications.* McGraw-Hill, 1995.

Astbury, G. R., and S. J. Hawksworth. "Spontaneous ignition of hydrogen leaks: A review of postulated mechanisms." *International Joural of Hydrogen Energy* 32 (2007): 2178-2185.

Browne, S. *Competition Effects in Combustion Chemistry and Their Role in Detonation Initiation.* Pasadena: California Institute of Technology, 2004.

Browne, S., J. Ziegler, and J. E. Shepherd. "Numerical solution methods for shock and detonation jump conditions." GALCIT Report FM2006.006, California Institute of Technology: Aeronautics and Mechanical Engineering, 2008.

Bureau de normalisation du Québec. "Canadian Hydrogen Installation Code." Bureau de normalisation du Québec, 2007.

Çengel, Y. A., and M. A. Boles. *Thermodynamics: An Engineering Approach.* 4th Edition. McGraw-Hill, 2002.

Coffee, T. P., and J. M. Heimerl. "Transport Algorithms for Premixed Laminar Steady-State Flames." *Combustion and Flame* 43 (1981): 273-289.

Cohen, S. D., and A. C. Hindmarsh. "CVODE: A Stiff/Nonstiff ODE Solver in C." *Computers in Physics* 10, no. 2 (1996): 138-143.

Dixon-Lewis, G. "Flame Structure and Flame Reaction Kinetics I: Solution of Conservation Equations and Application to Rich Hydrogen-Oxygen Flames." *Proceedings of the Royal Society of London Series A* 298, no. 1455 (1967): 495-513.

Dixon-Lewis, G. "Flame Structure and Flame Reaction Kinetics II: Transport Phenomena in Multicomponent Systems." *Proceedings of the Royal Society of London Series A* 307, no. 1488 (1968): 111-135.

Domingo, P., and L. Vervisch. "Triple flame and partially premixed combustion in auto-ignition of non-premixed turbulent mixtures." *Proc. Combust. Inst.* 26 (1996): 233-240.

Dryer, F. L., M. Chaos, Z. Zhao, J. N. Stein, J. Y. Alpert, and C. J. Homer. "Spontaneous ignition of pressurized releases of hydrogen and natural gas into air." *Combust. Sci. Tech.* 179 (2007): 663-694.

Echekki, T., and J. H. Chen. "Direct numerical simulation of autoignition in non-homogenous hydrogen-air mixtures." *Combustion and Flame* 134 (2003): 169-191.

Eckett, C. A., J. J. Quirk, and J. E. Shepherd. "The role of unsteadiness in direct initiation of gaseous detonations." *J. Fluid Mech.* 421 (2000): 147-183.

Golub, V. V., D. I. Baklanov, S. V. Golovastov, M. F. Ivanov, I. N. Laskin, A. S. Saveliev, N. V. Semin, and V. V. Volodin. "Mechanisms of high-pressure hydrogen gas self-ignition in tubes." *Journal of Loss Prevention in the Process Industries* 21 (2008): 185-198.

Goodwin, D. G. 2009. http://code.google.com/p/cantera/ (accessed December 14, 2009).

Hindmarsh, A. C., P. N. Brown, K. E. Grant, S. L. Lee, D. E. Serban, D. E. Shumaker, and C. S. Woodward. "SUNDIALS: Suite of Nonlinear and Differential/Algebraic Equations Solvers." *ACM Transactions on Mathematical Software* 31, no. 3 (2005): 363-396.

Hirschfelder, J. O., C. F. Curtiss, and R. B. Bird. *Molecular Theory of Gases and Liquids.* New York: John Wiley and Sons, 1954.

Ishii, R., H. Fujimoto, N. Hatta, and Y. Umeda. "Experimental and numerical analysis of circular pulse jets." *J. Fluid. Mech.* 392 (1999): 129-153.

Karasalo, I., and J. Kurylo. "On Solving the Stiff ODE's of the Kinetics of Chemically Reacting Gas Flow." *Journal of Computational Physics* 40 (1981): 167-182.

Kee, R. J., F. M. Rupley, J. A. Miller, M. E. Coltrin, J. F. Grcar, E. Meeks, H. K. Moffat, A. E. Lutz, G. Dixon-Lewis, M. D. Smooke, J. Warrantz, G. H. Evans, R. S. Larson, R. E. Mitchell, L. R. Petzold, W. C. Reynolds, M. Caracotsios, W. E. Stewart, P. Glarborg, C. Wang, and O. Adigun. *Chemikin collection release 3.6.* San Diego: Reaction Design Inc., 2000.

Kee, R. J., F. M. Rupley, E. Meeks, and J. A. Miller. "Chemkin-III: A Fortran Chemical Kinetics Package for the Analysis of Gas-Phase Chemical and Plasma Kinetics." Sandia National Laboratories, Livermore, CA, 1996.

Kioni, P., B. Rogg, K. Bray, and A. Linan. "Flame spread in laminar mixing layers: the triple flame." *Combust. Flame* 95, no. 3 (1993): 276-290.

Knikker, R., A. Dauptain, B. Cuenot, and T. Poinsot. "Comparison of computational methodologies for ignition of diffusion layers." *Combustion Science and Technology* 175, no. 10 (2003): 1783-1806.

Lacerda, N. L. "On the start up of supersonic underexpanded jets." PhD Thesis, California Institute of Technology, Pasadena, CA, 1987.

Law, C. K. *Combustion Physics.* New York: Cambridge University Press, 2006.

Leveque, R. J. *Finite Volume Methods for Hyperbolic Problems.* New York: Cambridge University Press, 2002.

Li, Juan, Zhenwei Zhao, Andrei Kazakov, and Frederick L. Dryer. "An Updated Comprehensive Kinetic Model of Hydrogen Combustion." *International Journal of Chemical Kinetics* 36, no. 10 (2004): 566-574.

Liepmann, H. W., and A. Rhoshko. *Elements of Gas Dynamics.* Dover, 2001.

Liu, Y. F., N. Tsuboi, H. Sato, F. Higashino, and A. K. Hayashi. "Direct numerical simulation on hydrogen fuel jetting from high pressure tank." *20th Intl Colloquium on the Dynamics of Explosions and Reactive Systems.* Montreal, Canada, 2005.

Liu, Y. L., J. Y. Zheng, P. Xu, Y. Z. Zhao, H. Y. Bie, H. G. Chen, and H. Dryver. "Numerical simulation on the diffusion of hydrogen due to high pressure storage tanks failure." *Journal Loss Prevention in the Process Industries* 22 (2009): 265-270.

Lopez, R. J. *Advanced Engineering Mathematics.* Addison-Wesley, 2001.

Lundstrom, E. A., and A. K. Oppenheim. "On the Influence of Non-Steadiness on the Thickness of the Detonation Wave." *Proc. R. Soc. Lond. A* 310 (1969): 463-478.

Mogi, T., D. Kim, H. Shiina, and S. Horiguchi. "Self-ignition and explosion during discharge of high-pressure hydrogen." *Journal of Loss Prevention in the Process Industries* 21 (2008): 199-204.

Paolucci, S. "On the filtering of sound from the Navier–Stokes equations." Report, Sandia. National Laboratories, Livermore, CA, 1982.

Prata, S. *C++ Primer Plus.* 5th Edition. Sams Publishing, 2005.

Quirk, J. J. "Amr_sol : Design Principles and Practice." Edited by H. Deconinck. *29th Computational Fluid Dynamics, von Karman Institute Lecture Series.* 1998a.

Quirk, J. J. "Amrtia: A Computational Facility (for CFDModelling)." Edited by H. Deconinck. *29th Computational Fluid Dynamics, von Karman Institute Lecture Series.* 1998b.

Radulescu, M. I., and C. K. Law. "The transient start of supersonic jets." *J. Fluid Mech* 578 (2007): 331-369.

Rogg, B., and W. Wang. "Run-1DL User Manual." Lehrstuhl fur Stromungsmechanik, Institut fur Thermo-und Fluiddynamik, Ruhr-Universitat Bochum, D-44780 Bochum Germany, 1995.

Thompson, P. A. *Compressible-Fluid Dynamics.* Edited by I. H. Shames. Library of Congress, 1988.

Toong, T. Y. *Combustion Dynamics: The Dynamics of Chemically Reacting Fluids.* McGraw-Hill, 1983.

Versteeg, H. K., and W. Malalasekera. *An Introduction to Computational Fluid Dynamics: The Finite Volume Method.* 2nd Edition. Pearson Education Limited, 2007.

Vieira, A., H. Faria, R. Oliveira, N. Correia, and A. T. Marques. "H2 High Pressure On-Board Storage Considering Safety Issues." *2nd International Conference on Hydrogen Safety.* San Sebastian, Spain, 2007.

Warnatz, J., U. Maas, and R. W. Dibble. *Combustion: Physical and Chemical Fundamentals, Modelling and Simulation, Experiments, Pollutant Formation.* 4th Edition. Springer, 2006.

Williams, F. A. *Combustion Theory.* 2nd Edition. Menlo Park, CA: Benjamin/Cummings Publishing Company Inc., 1985.

Wolanski, P., and S. Wojcicki. "Investigation into the mechanism of diffusion ignition of a combustible gas flowing into an oxidizing atmosphere." *14th Symp. (Int.) on Combustion.* Pittsburgh, PA: The Combustion Inst., 1973. 1217-23.

Xu, B. P., L. E. Hima, J. X. Wen, S. Dembele, V. H. Y. Tam, and T. Donchev. "Numerical study on the spontaneous ignition of pressurized hydrogen release through a tube into air." *Journal of Loss Prevention in the Process Industries* 21 (2008): 205-213.

Xu, B. P., L. E. L. Hima, J. X. Wen, S. Dembele, and V. H. Y. Tam. "Numerical study of spontanous ignition of pressurized hydrogen release into air." *International Journal of Hydrogen Energy*, 2009.

Appendix A

Shock Tube Problem with Frozen Chemistry

The *shock tube problem* (Liepmann and Rhoshko 2001) is solved in order to determine the initial boundary conditions of the mixing layer at the head of the jet in hydrogen release problem. Here a derivation of the shock tube problem is given by taking realistic thermal properties into account. An algorithm is then proposed to solve the problem numerically. First, an introduction is given regarding the shock tube problem itself.

A shock tube is a device used in a lab that is used to generate shock waves in a long tube. Consider the shock tube shown below in Figure A.1, where a high pressure driver gas is separated by a test gas in a shock tube with a diaphragm.

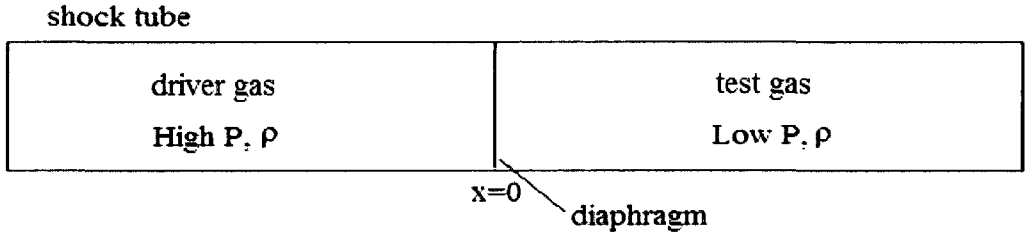

Figure A.1 Shock tube setup.

Once the diaphragm is broken, a shock wave travels through the test gas. Behind the shock, the contact surface of the driver gas also travels to the right. This contact surface acts as a piston, driving the shock ahead. The piston, or contact surface, as well as the shock wave will travel at a constant speed prior to interaction with the shock tube end walls. At the same time, a centered expansion wave travels into the driver gas, causing the gas to start moving to the right to match the velocity of the piston, or contact surface. An *x-t* diagram is shown below in Figure A.2 showing the profiles of the shock wave, contact surface, and expansion wave for the problem outlined above. The particle paths are also shown for particles starting in both the driver gas and test gas sections.

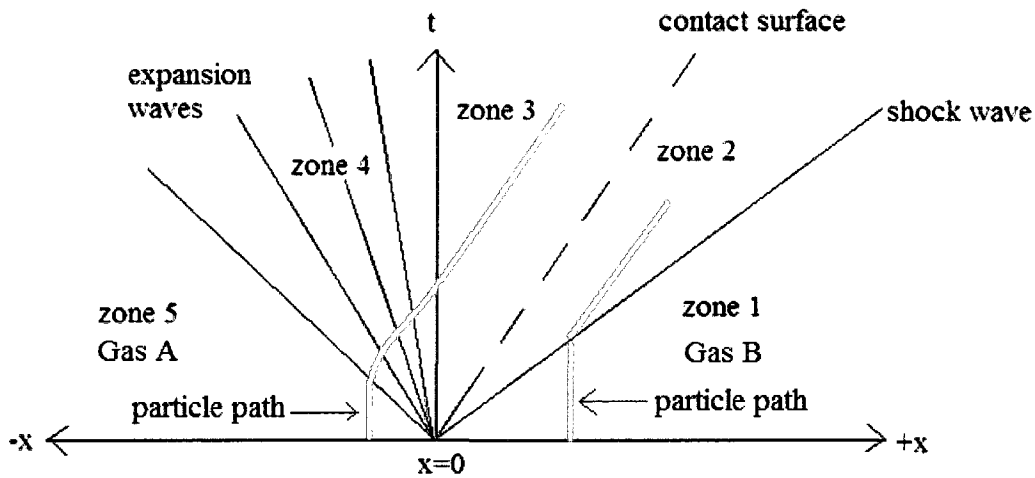

Figure A.2: x-t diagram for shock tube problem.

The zones 1-5 in Figure A.2 correspond to the following regions:

Zone 1: Undisturbed test gas.

Zone 2: Shocked test gas.

Zone 3: Expanded driver gas.

Zone 4: Expansion zone.

Zone 5: Undisturbed driver gas.

The solution to this problem is obtained by matching the pressure and velocities of the two gasses at the contact surface (Liepmann and Rhoshko 2001; Thompson 1988). Let us examine the solution in each of the 5 zones.

Across the Shock (zone 1 to 2):

Consider a control volume surrounding the shock wave shown below in Figure A.3. In the frame of reference of the shock itself, a fluid particle will travel towards the shock wave from the right at velocity w_1. Once shocked, the particle will continue to travel to the left, away from the shock, at velocity w_2. The velocities, w_1 and w_2, are related to the absolute velocities of the fluid to the right of the shock, u_1, the fluid to the left of the shock, u_2, and the velocity of the shock wave itself, u_s, through equations A.1 and A.2, respectively.

$$w_1 = u_s - u_1 \qquad \text{A.1}$$

$$w_2 = u_s - u_2 \qquad \text{A.2}$$

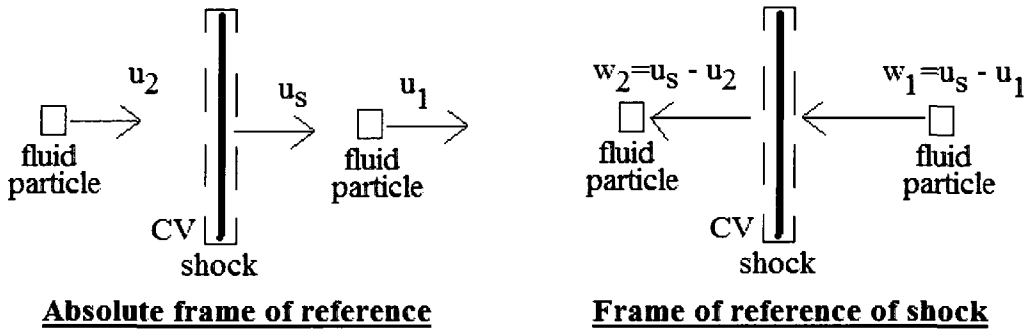

Figure A.3: Control volume analysis of shock wave in absolute frame of reference (left) and also in the frame of reference of the shock wave itself (right).

From the conservation of mass, momentum, and energy, across the shock in the frame of reference of the shock itself we have three equations.

$$\rho_1 w_1 = \rho_2 w_2 \tag{A.3}$$

$$p_1 + \rho_1 w_1^2 = p_2 + \rho_2 w_2^2 \tag{A.4}$$

$$h_1 + \frac{w_1^2}{2} = h_2 + \frac{w_2^2}{2} \tag{A.5}$$

Substituting equation A.3 into equations A.4 and A.5 yields two equations for determining the pressure and enthalpy in shocked zone:

$$p_2 = p_1 + \rho_1 w_1^2 \left(1 - \frac{\rho_1}{\rho_2}\right) \tag{A.6}$$

$$h_2 = h_1 + \frac{w_1^2}{2}\left(1 - \left(\frac{\rho_1}{\rho_2}\right)^2\right) \tag{A.7}$$

The enthalpy at any particular state involving K chemical species can be calculated from equation A.8.

$$h = \sum_{i=1}^{K} Y_i h_i(T) \tag{A.8}$$

where the enthalpy of the ith species is given by equation A.9.

$$h_i = h_i^o + \int_{T_o}^{T} c_{p,i}(T)dT \tag{A.9}$$

Where h_i^o is the enthalpy of formation of the *i*th species at temperature T_o. Specifically, the enthalpy at state 1 can be calculated directly using Cantera (Goodwin 2009), which solves equations A.8 and A.9. To solve the enthalpy at state 2 using equation A.8 instead of A.7 we must first assume that the chemistry is frozen across the shock. In other words:

$$Y_{2,i} = Y_{1,i} \tag{A.10}$$

Therefore, the enthalpy at state 2 can be solved in terms of temperature and the undisturbed mass fraction of state 1:

$$h_2 = \sum_{i=1}^{K} Y_{1,i} h_{1,i}(T_2) \tag{A.11}$$

Furthermore, the temperature, density, and pressure are related through the equation of state:

$$\frac{p}{\rho} = \frac{R^o T}{\bar{W}} \tag{A.12}$$

Where R^o is the universal gas constant and $\bar{W}$ mean molecular weight of the fluid mixture. By applying the equation of state:

$$\frac{p_1}{\rho_1 T_1} = \frac{p_2}{\rho_2 T_2} \tag{A.13}$$

In 2008, Browne, Ziegler, and Shepherd developed an algorithm (Browne, et al. 2008) to solve for state 2 providing the speed of the shock, u_s, is known. However, since u_s is not known, the problem is more complex and we have to look at the other zones to fully solve the problem.

Across the contact surface (zone 2 to 3):

Across the contact surface, the velocities and pressures are equal. However the densities and temperatures are not. Therefore:

$$P_2 = P_3, \quad u_2 = u_3, \quad \rho_2 \neq \rho_3, \quad T_2 \neq T_3$$

Across the expansion waves (zones 3 to 5):

If the expansion in zone 4 is isentropic, then

$$s_3 = s_5 \tag{A.14}$$

Furthermore, for isentropic flow, the speed of sound can be evaluated through equation A.15.

$$a^2 = \left(\frac{\partial p}{\partial \rho}\right)_s \tag{A.15}$$

Moreover, if the chemistry is across the expansion zone is frozen, as we have assumed for the flow across the shock, zone 1 to 2, then

$$Y_{3,i} = Y_{4,i} = Y_{5,i} = \text{constant} \tag{A.16}$$

Thus the speed of sound across the expansion zone is evaluated through equation A.17.

$$a^2 = \left(\frac{\partial p}{\partial \rho}\right)_{s,Y} \tag{A.17}$$

Therefore, the *Riemann invariants* (Thompson 1988) along the $a \pm$ characteristics, shown in Figure A.4, can be found to be

$$J\pm = u \pm F = \text{constant along } a \pm \tag{A.18}$$

where

$$F = \int_{p_o}^{p} \frac{dp}{\rho a} \tag{A.19}$$

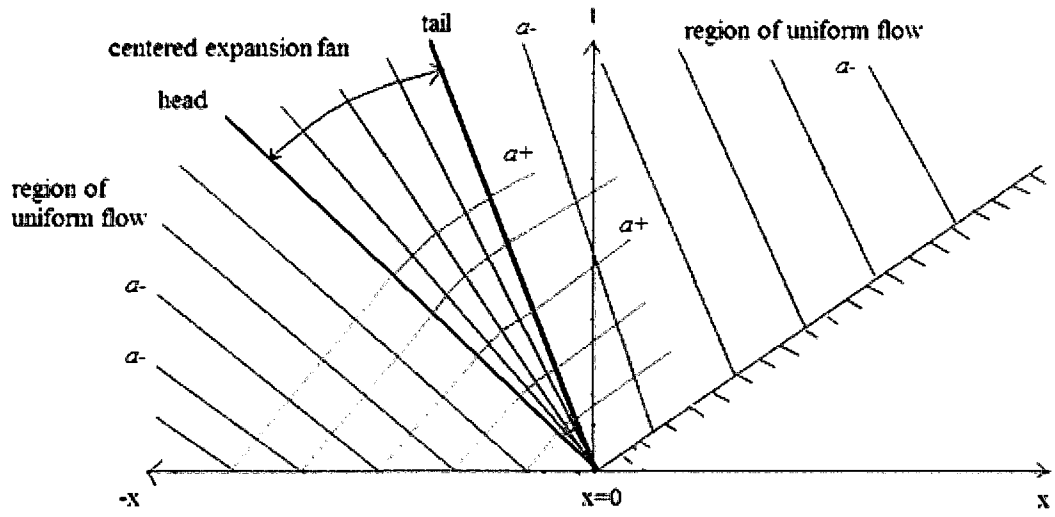

Figure A.4: Characteristic lines across a centered expansion fan (Thompson 1988).

By solving equation A.18 along the $a+$ characteristics we can solve for the velocity at any point in the expansion fan:

$$u_4 = u_5 + \int_{p_3}^{p_4} \frac{dp}{\rho a} \qquad \textbf{A.20}$$

where the reference pressure p_o is taken at state 5, p_5. Since the flow is isentropic and the chemistry is frozen, all other parameters can be found, using Cantera (Goodwin 2009), since state 5 is known.

$$\rho_4 = \rho\left(p_4, s_4 = s_5, Y_{4,i} = Y_{5,i}\right) \qquad \textbf{A.21}$$

$$a_4 = a\left(p_4, s_4 = s_5, Y_{4,i} = Y_{5,i}\right) \qquad \textbf{A.22}$$

$$T_4 = T\left(p_4, s_4 = s_5, Y_{4,i} = Y_{5,i}\right) \qquad \textbf{A.23}$$

Noting that $u_2 = u_3$ and that $u_5 = 0$, the velocity at state 3 is simply

$$u_2 = u_3 = \int_{p_3}^{p_3} \frac{dp}{(\rho a)_{s=s_5}} \qquad \textbf{A.24}$$

Here equation A.24 can be integrated numerically using the *Trapezoid Rule* (Lopez 2001).

Algorithm for solving shock tube problem

To solve the shock tube problem described above, the following algorithm is proposed, and is based on the algorithm proposed by Browne, et al. (2008) for finding a solution across the shock. The approach solves for states 2 and 3, iteratively, until the conditions $P_2 = P_3$ and $u_2 = u_3$ are met across the contact surface between the two gases.

1. Guess u_s
2. Guess ρ_2
3. Solve for w_1 from equation A.1 (note that $u_1 = 0$)
4. Solve for p_2 from equation A.6
5. Solve for h_2 from equation A.7
6. Solve for T_2 from equation A.13
7. Solve for h_2 from equation A.11
8. Compare solution for h_2 from steps 5 and 7
9. If not equal, return to step 2 and make a new guess for ρ_2.
10. If equal, solve for u_2 from equation A.24, noting that $p_3 = p_2$
11. Solve for u_2 from equations A.2 and A.3 and compare with solution from step 10
12. If not equal, return to step 1 and make a new guess for u_s.
13. If equal, then all states are known!

Appendix B

H_2 Release Solver Flow Chart (Both Models)

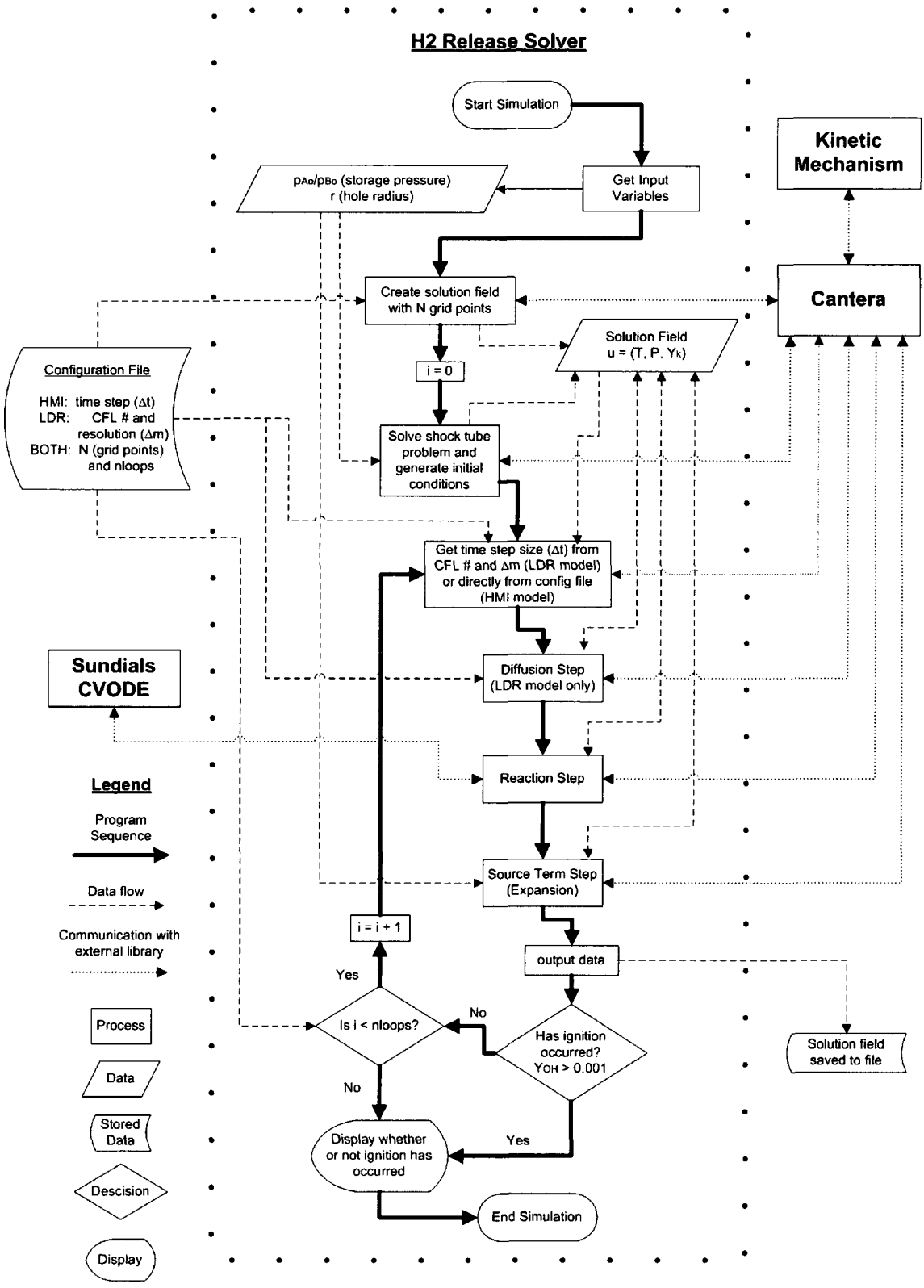
H2 Release Solver
Start Simulation
Get Input Variables
pAo/pBo (storage pressure)
r (hole radius)
Kinetic Mechanism
Cantera
Create solution field with N grid points
Solution Field
u = (T, P, Yk)
Configuration File
HMI: time step (Δt)
LDR: CFL # and resolution (Δm)
BOTH: N (grid points) and nloops
i = 0
Solve shock tube problem and generate initial conditions
Get time step size (Δt) from CFL # and Δm (LDR model) or directly from config file (HMI model)
Sundials CVODE
Diffusion Step (LDR model only)
Reaction Step
Source Term Step (Expansion)
i = i + 1
output data
Yes
Is i < nloops?
No
Has ignition occurred? YOH > 0.001
Solution field saved to file
No
Yes
Display whether or not ignition has occurred
End Simulation
Legend
Program Sequence
Data flow
Communication with external library
Process
Data
Stored Data
Descision
Display